Doctoral Thesis

Experimental Study on the Role of Secondary Vortex at Trailing Edge in Motion-induced Vortex Vibration

By

Nade Cao

Supervisor: Professor Kazutoshi Matsuda

Department of Civil Engineering and Architecture

Kyushu Institute of Technology

2021

CONTENTS

Chapter 1: Introduction

1.1 Research Background

In constructed environments, architectural and engineering structures are usually designed as bluff shape, in order to meet the requirements of structural performances. The aerodynamic characteristics of bluff bodies therefore become a critical subject in wind-resistant design. The aerodynamic characteristics of bluff bodies have been a subject of a considerable study since the collapse of the Tacoma Narrow Bridge in U.S.A. in 1940. A principal feature of bluff bodies is that they create separated flow regions which become the source of vortex shedding, hence the aerodynamic characteristics of bluff bodies are extremely complex. Vortices shedding from a bluff body are related to a variety of aerodynamic instability phenomena, which can reduce the useful life of the structures or even destroy the structures fatally. Regarding these aerodynamic instability phenomena, vortex-induced vortex vibration is one of the most important design issues in wind engineering. Vortex-induced vibration is a kind of limited-amplitude vibration and rarely leads to destructive damage for the structures. However, vortex-induced vibration can result in large amplitude under relatively low wind velocity, then reduce the fatigue life of the structures inevitably. **Figure 1.1.1** shows the occurrence of vortex-induced vortex vibration in the Volgograd Bridge in Russia in 2010[1)]. One of the essential requirements of modern wind-resistance design is to limit the amplitude of vortex-induced vibration or eliminate it to minimum extent. In order to achieve that, a number of wind tunnel tests aiming to elucidate the aerodynamic characteristic of vortex-induced vibration have been conducted.

According to the results of the previous wind tunnel tests, vortices separated from two-dimensional bluff bodies can be broadly divided into the Kármán vortex and the motion-induced vortex (separated vortex from leading edge and secondary vortex at trailing edge)[2,3)]. **Figure 1.1.2** and **Figure 1.1.3** show the schematic illustration of the Kármán vortex and the motion-induced vortex, respectively. The Kármán vortex is accompanied by interference of the two separated shear layers separated alternately from both the top and bottom surfaces of the bodies. The vortex-induced vibration caused by the Kármán vortex is closely related with the Strouhal number *St* determined

Figure 1.1.1 Vortex-induced vibration in the Volgograd Bridge[1)]

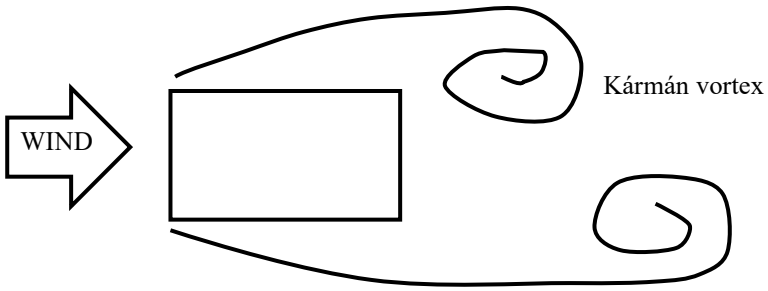

Figure 1.1.2 Schematic illustration of the Kármán vortex

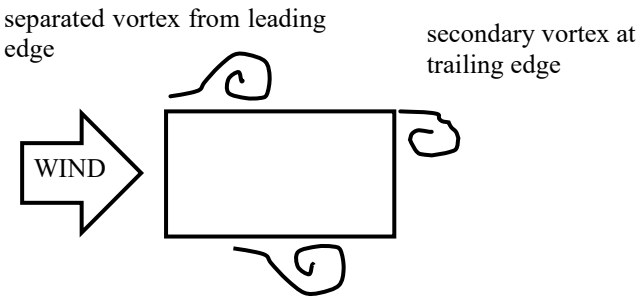

Figure 1.1.3 Schematic illustration of the motion-induced vortex

by the shape and side ratio of the bodies. This vortex-induced vibration is explained as a lock-in phenomenon between the frequency of the Kármán vortex and the natural frequency of the body[2)].

On the other hand, the separated vortex from leading edge is shed separately from the leading edges of the upper and bottom surfaces. The shedding of the separated vortex from leading edge is one of the basic flow phenomena related to shallow cavities and bluff bodies[4)]. The vibration caused by the separated vortex from leading

edge was found in the past wind tunnel tests[5]. The separated vortex from leading edge synchronizing with the body produces dynamic lift within a certain range of wind velocities. In the resonance wind velocity region, a lock-in phenomenon is also confirmed between the natural frequency of the structure and the frequency of the separated vortex from leading edge, which is independent of the Strouhal number *St*[4, 5]. The frequency of the separated vortex from leading edge is related to the shape of the structure and the wind velocity[6]. The vortex-induced vibration caused by the separated vortex from leading edge is known as either motion-induced vortex vibration[2,3] or impinging-shear-layer instability[6, 7], which is a seed of one-shear-layer-type instability. The motion-induced vortex vibration is characterized by two types of unsteady vortices. One is the separated vortex from leading edge, while the other is generated in the wake near the trailing edge in-phase with the separated vortex from leading edge due to the vibration of the body. The latter vortex is referred to as the secondary vortex at trailing edge[2]. In general, the motion-induced vortex vibration is considered to be caused by the unification of the separated vortex from leading edge and the secondary vortex at trailing edge[2]. According to the summary of the results of previous wind tunnel tests[2], the motion-induced vortex has been confirmed on rectangular cross sections with side ratios of B/D=2–8(B: along-wind length, D: cross-wind length).

In 2009, Ikitsuki Bridge, a truss bridge in Japan with a center span length of 400m, was discovered to have a crack in the diagonal member of the bridge[8]. The side ratio of the section was B/D=1.18(B=590mm, D=500mm). As a result of a field oscillation measurement, the primary cause of the crack was identified as the Kármán vortex-induced vibration. However, another aerodynamic vibration was also observed in the wind velocity range lower than the resonance wind velocity of the Kármán vortex vibration[8]. In addition, it was confirmed that the onset reduced wind velocity of the aerodynamic vibration occurring in lower wind velocity region is close to the empirical value of the onset reduced wind velocity of the motion-induced vortex vibration. Nevertheless, there is little past research on the motion-induced vortex vibration on the rectangular cross section with side ratios smaller than B/D=2. For that reason, a series of wind tunnel tests for the bracing member of Ikitsuki Bridge and rectangular cross sections with side ratio B/D=1.18 were carried out for the sake of clarifying aerodynamic vibration occurring in the lower wind velocity range. As a

result, a new finding was that the aerodynamic vibration in the bracing member of Ikitsuki Bridge generated in the wind velocity range lower than Kármán vortex-induced vibration was suggested to possibly be the motion-induced vortex vibration by the experimental results of the spring-supported tests and the unsteady aerodynamic lift measurements. Nevertheless, the results of flow visualization tests suggested that the secondary vortex at trailing edge was not observed while the motion-induced vortex vibration has been generated[9]. This result shows a possibility that motion-induced vortex vibration might occur without the formation of secondary vortex at trailing edge. Obviously, this result is in contradiction with the conventional conception on the motion-induced vortex vibration[2], and indicates that the role of the secondary vortex at trailing edge in the motion-induced vortex vibration is not totally clear, further investigation is needed.

The motion-induced vortex vibration occurs in many engineering situations. Especially, the service lives of bridge decks are prone to be influenced by the motion-induced vortex vibration. With the ever-growth of span length, bridge decks are becoming more flexible and thereby more susceptible to the motion-induced vortex vibration. Therefore, the vibration control countermeasure against the motion-induced vortex vibration is necessary in the wind engineering design area. Usually, the vibration control countermeasure can be divided into the mechanical vibration control countermeasure and the aerodynamic vibration control countermeasure. In the case of mechanical vibration countermeasure, the vibration is suppressed by increasing the damping. In the aerodynamic vibration control countermeasure, the cause of vibration is eliminated by changing the flow field around the bridge deck. Normally, the cross section of the bridge deck is modified or attached with additional members such as flap or spoiler. Thus, in order to modify the cross sections of the bridge decks appropriately and maximize the improvement of the additional members on the wind-resistant performance against the motion-induced vortex vibration, it is necessary to clarify the roles of the separated vortex from leading edge and the secondary vortex at trailing edge in the motion-induced vortex vibration. However, the conventional conception on the secondary vortex at trailing edge is not explicit. Therefore, it can be difficult to improve the wind-resistant performance of bridge decks and additional members efficiently against the motion-induced vortex vibration for wind-resistant designers with respect to the aerodynamic vibration control countermeasure against

the motion-induced vortex vibration. This study thereby focuses on the role of the secondary vortex at trailing edge in the motion-induced vortex vibration for the sake of providing more valuable insights to wind-resistant designers in terms of optimizing cross sections of bridge decks and maximizing the improvement of the additional members on the wind-resistant performance against the motion-induced vortex vibration.

1.2 Research Objective and Thesis Contents

The current study aims to give a more comprehensive explanation on the effect of the secondary vortex at trailing edge on the motion-induced vortex vibration. Rectangular cross sections with side ratios of B/D=0.50-6.0 including side ratios smaller than B/D=2.0 were used as the target cross sections. In addition, specific cross sections where the secondary vortex at trailing edge is considered less likely to occur were also used in order to get a better grasp on the effect of the secondary vortex at trailing edge on the motion-induced vortex vibration. Spring-supported and flow visualization tests were conducted. By comparing the flow patterns of the secondary vortex at trailing edge with the response characteristics of the target cross sections, the purpose of this study is to clarify the role of the secondary vortex at trailing edge in the motion-induced vortex vibration.

This thesis included total 7 chapters.

Chapter 1 introduced the entire research background and objective of this study.

Chapter 2 described the literature reviews mainly about the mechanism of the motion-induced vortex vibration, the flow pattern of the separated vortex from leading edge and the aerodynamic characteristics of the bracing member in the Ikitsuki Bridge.

In chapter 3, the spring-supported and flow visualization tests for rectangular cross sections with side ratios of B/D=0.50-1.18 in the heaving mode were introduced. By comparing the flow patterns of the secondary vortex at trailing edge with the response characteristics of motion-induced vortex vibration, the necessity of the secondary vortex at trailing edge for the generation of the motion-induced vortex vibration for rectangular cross sections with small side ratios in the heaving mode was evaluated.

Chapter 4 introduced the spring-supported and flow visualization tests for

rectangular cross sections with side ratios of *B/D*=2, 4, 6 in the heaving mode. The necessity of the secondary vortex at trailing edge for the onset of the motion-induced vortex vibration for the acknowledge rectangular cross sections on which the motion-induced vortex vibration has been confirmed to occur in the heaving mode was clarified. Further, the influence of the secondary vortex at trailing edge on the extent of the exciting force of the motion-induced vortex vibration in the heaving mode was also discussed.

In chapter 5, the spring-supported and flow visualization tests for rectangular cross sections with side ratios of *B/D*=2, 4, 6 in the torsional mode were described. Based on the results of the wind tunnel tests, the necessity of the secondary vortex at trailing edge for the onset of the motion-induced vortex vibration for rectangular cross sections with side ratios of *B/D*=2, 4, 6 in the torsional mode was evaluated. The influence of the secondary vortex at trailing edge on the extent of the exciting force of the motion-induced vortex vibration in the torsional mode was also evaluated. Moreover, the difference between the results of wind tunnel tests for rectangular cross sections with side ratios of *B/D*=2, 4, 6 in the heaving and torsional mode was discussed.

In chapter 6, the spring-supported and flow visualization tests for two kinds of specific cross sections where the secondary vortex at trailing edge is considered less likely to occur were described. The necessity of the secondary vortex at trailing edge for the onset of the motion-induced vortex vibration was evaluated. Furthermore, at the wind velocity where larger response amplitude of the motion-induced vortex vibration occurs, the influence of the secondary vortex at trailing edge on the response characteristic of motion-induced vortex vibration was clarified.

In chapter 7, conclusions drawn based on this study were summarized. Based on the results obtained from this study, the future issues were stated.

References

1) https://www.dailymail.co.uk/news/article-1280919/Russian-bridge-bounces-feet-Volga River.html
2) Shiraishi, N. and Matsumoto, M., 1983. On classification of vortex-induced oscillation and its application for bridge structures, Journal of Wind Engineering and Industrial Aerodynamics, 14 (1-3), 419-430.
3) Komatsu, S. and Kobayashi, H., 1980. Vortex-induced oscillation of bluff cylinders, Journal of Wind Engineering and Industrial Aerodynamics, 6, 335-362.
4) Nakamura, Y. and Nakashima, M., 1986. Vortex excitation of prisms with elongated rectangular, H and ⊢ cross-section, Journal of Fluid Mechanics, 163, 149-169.
5) Novak, M., 1971. Galloping and vortex induced oscillations of structures, Proceedings of the 3rd International Conference on Wind Effects on Buildings and Structures, Tokyo, Japan, 799-809.
6) Ohya, Y., Nakamura, Y., Ozono, S., Tsuruta, H. and Nakayama, R., 1992. A numerical study of vortex shedding from flat plates with square leading and trailing edges, Journal of Fluid Mechanics, 236, 445-460.
7) Naudascher, E. and Wang, Y., 1993. Flow-induced vibrations of prismatic bodies and grids of prisms, Journal of Fluids and Structures, 7, 341-373.
8) Nakamura, S., Shintomi, K., Tanaka, S., Nishikawa T. and Okumatsu, T., 2012. A survey on wind conditions at the Ikitsuki Bridge, Proceedings of the 67th annual meeting of JSCE, No.67, I-323, 645-646. (in Japanese)
9) Tamai, Y., Matsuda, K., Kato, K., Misawa, K. and Ikeda, I., 2014. Experimental study on aerodynamic vibration of a bracing member with a rectangul ar cross section of the long-spanned truss bridge, Proceedings of the 23rd National Symposium on Wind Engineering, 211-216. (in Japanese)

Chapter 2: Literature Review

2.1 Mechanism of Motion-induced Vortex

The target of this study is to give a more comprehensive explanation on the effect of the secondary vortex at trailing edge on the motion-induced vortex vibration. Thus, it is necessary to grasp the mechanism and the basic properties of the motion-induced vortex. In this section, the flow properties of the separated vortex from leading edge and the fundamental considerations on the secondary vortex at trailing edge obtained from previous studies were introduced.

2.1.1 Flow Properties of Separated Vortex from Leading Edge

Figure 2.1.1 summarizes the dominant frequency of the vortex formation in the form of the Strouhal number $S_h=fd/V$ based on cross-wind length of the model d for stationary prisms with an angle of attack α=0°, where f is the dominant frequency of the vortex, d is defined in the figure and V is the approaching wind velocity[1]. With regard to rectangular cross sections, the flow regimes were distinguished into 4 regimes, which are regime 1, regime 2a, regime 2b and regime 3, respectively[2].

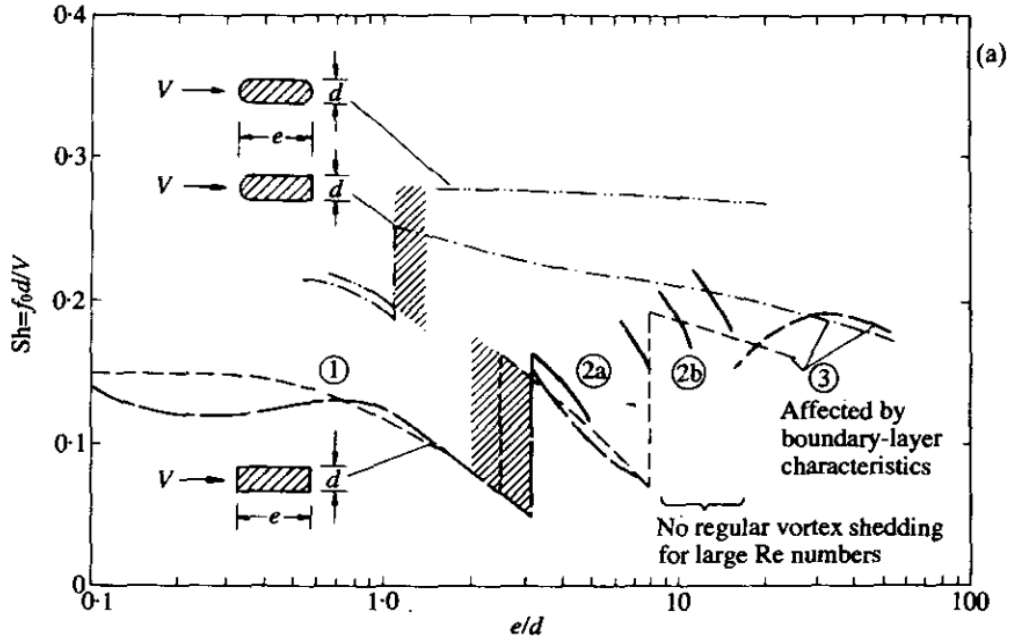

Figure 2.1.1 Strouhal number for stationary prisms in cross flow based on the cross-wind length of the model d[1]

Regime 1 is associated with non-reattaching separation streamlines in the range of roughly e/d=0-3 for smooth flow, and e/d=0-2 for turbulent flow. In regime 2a, which extends roughly over the range of e/d=2-8, the separated shear layers reattach intermittently. In the adjacent regime 2b, e/d=8-16, there is hardly any regular vortex shed for a stationary prism. In regime 3, beyond e/d=16, boundary layers develop past reattachment and combine to form a stable vortex street at a short distance downstream of the trailing edge.

The vortex formation in regime 2a is controlled by a flow instability equivalent to the impinging shear layer[3] or the separated vortex from leading edge[4]. Vortices formed in the unstable free shear layers on the two sides of the prism are transported with convection velocity V_c toward the trailing edges where they generate pressure pulsations which are fed back upstream and trigger the development of new vortices. The Strouhal number S_h of these vortices can be described as follows:

$$S_h = \frac{fd}{V} = (n + \varepsilon)\frac{V_c}{V}\frac{d}{e}, \quad n = 1, 2, \ldots \tag{2.1.1}$$

where length e is equivalent to the length between shear layer origin and impingement edge, and the variables ε and V_c/V depend on the particular flow conditions and the order n of the vortex formation mode.

Figure 2.1.2 shows the variation of the reduced frequency of the separated vortex from leading edge $St=fe/V$ based on the along-wind length of the model e for

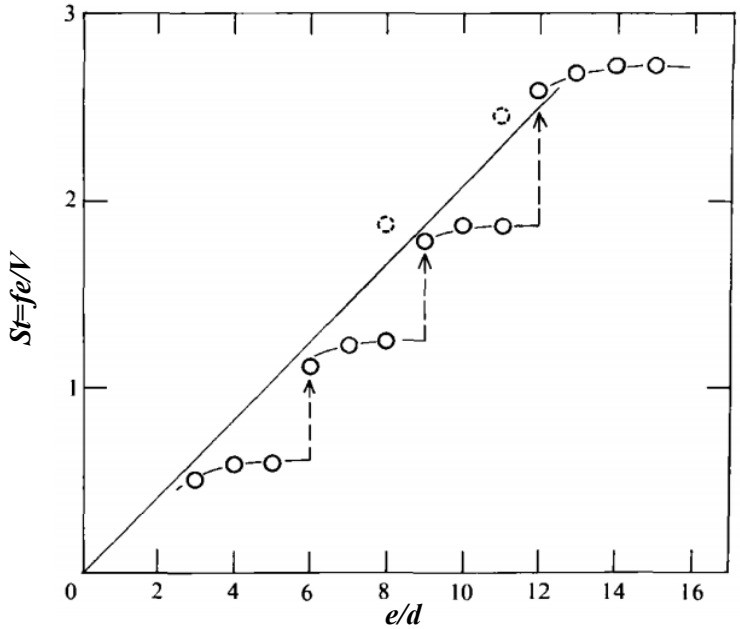

Figure 2.1.2 Strouhal number for rectangular cylinders based on the along-wind length of the model e[5]

rectangular cylinders[5]. *St* is nearly constant and equal to 0.6 for *e/d*=3-5. With further increase in *e/d*, *St* increases stepwise to values which are approximately equal to integral multiples of 0.6. Accordingly, each branch of nearly constant *St* is given an integral *n*. *St* often has two values at the jump. Full circles correspond to the higher peaks in the spectra while broken circles correspond to the lower ones.

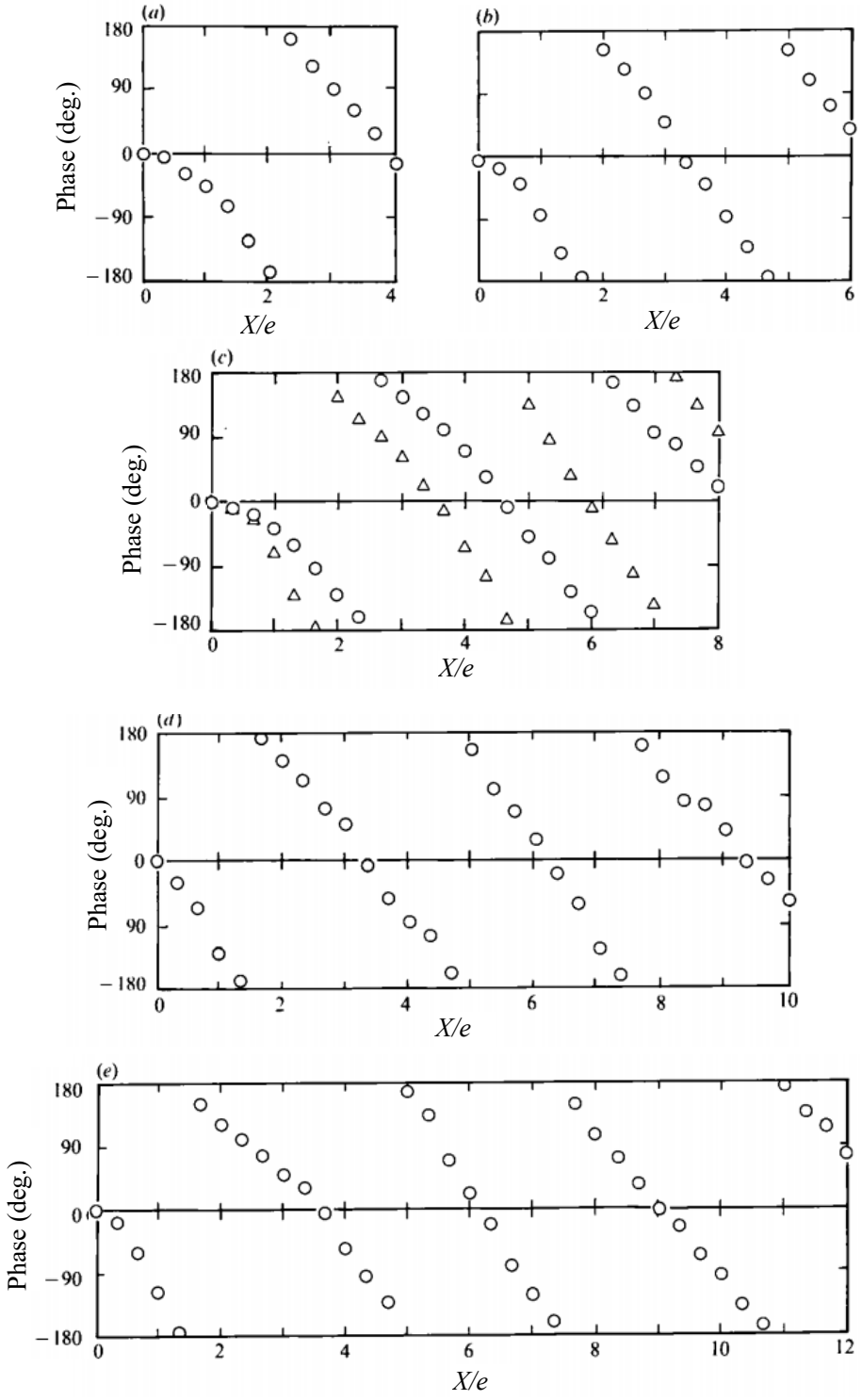

Figure 2.1.3 Phase angel of the separated vortex on the side face. (a) *e/d*=4, (b) *e/d*=6, (c) *e/d*=8, (d) *e/d*=10, (e) *e/d*=12; ○, *n*=2; △, *n*=3[6]

In **Figure 2.1.3**, the phase angle of the fluctuation at the dominant frequency, measured relative to that at leading edge, is plotted against the distance along the surface of the model X for various side ratios of e/d [6]. In accordance with the results shown in **Figure 2.1.2**, the wavelength is just equal (n=1 and 2) or approximately equal (n=3 and 4) to the along-wind lengths of the models. In other words, the integer n represents the number of the separated vortex from leading edge. The motion-induced vortex vibration initiates at about e/d=3 where the wavelength of the separated vortex from leading edge is just equal the along-wind lengths of the model. As the side ratio increases, the wavelength is locked-on to the along-wind lengths of the model through some nonlinear flow processes until a certain limit is reached. At the limit, transition of the mode of the shedding of the separated vortex from leading edge from n=1 to n=2 occurs. With a further increase in the side ratio, the same cycle of events repeats.

It should be noted that the transition of the mode of the shedding of the separated vortex from leading edge does not mean that the mechanism of the separated vortex from leading edge with smaller n vanished there. It means rather that this mechanism is too weak to materialize without additional control. Such control can be obtained either externally by means of sound field or internally by the movement of the leading edge[7].

Figure 2.1.4 shows the motion of the separated vortex from leading edge on the

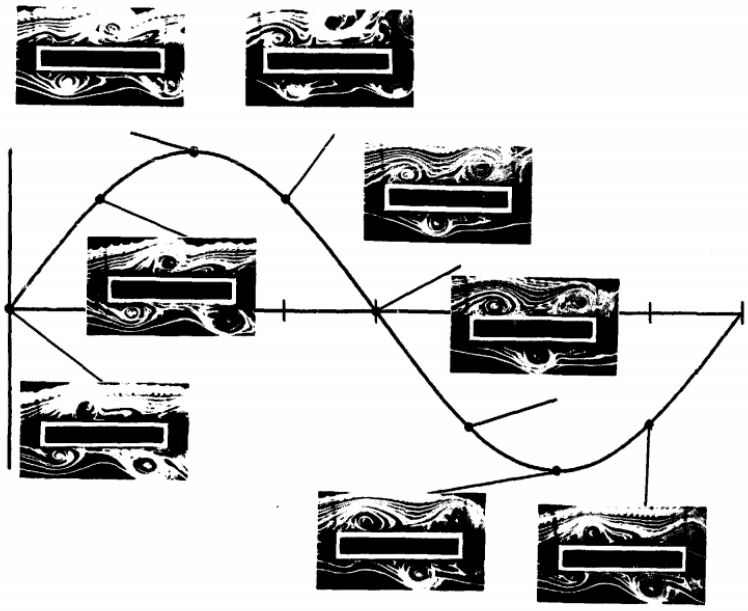

Figure 2.1.4 The motion of the separated vortex from leading edge on the surface of a rectangular cylinder in one cycle of torsional vibration[8]

surface of a rectangular cylinder in one cycle of torsional vibration[8]. In this figure,two pairs of the separated vortices from leading edge appear respectively on the upper and lower surfaces in the first 1/4 cycle, two and one in 1/4 to 3/4 cycle, one and two in the last 1/4 cycle. When the model starts to move downward from upper rest position, the separated shear layer starts to be entrained as a vortex on the upper surface and grows larger as it flows down to leeward of the model.

In the light of the previous results of wind tunnel tests, it is suggested that the vibration mode of the motion-induced vortex vibration is determined by the arrangement of the separated vortices from leading edge on the surface of the model[8]. The equal number of the separated vortices from leading edge existing on both upper and lower surfaces correspond to the appearance of the torsional vibration, while the difference by one in the number of the separated vortices from leading edge corresponds to the heaving vibration. **Figure 2.1.5** shows the arrangement of the separated vortices from leading edge in the heaving and torsional mode[8]. In the case of one different number of the separated vortex from leading edge between upper and lower surface, the forces work to move the model up and down, whereas in the case of equal number of the separated vortex from leading edge, the forces work to rotate the model.

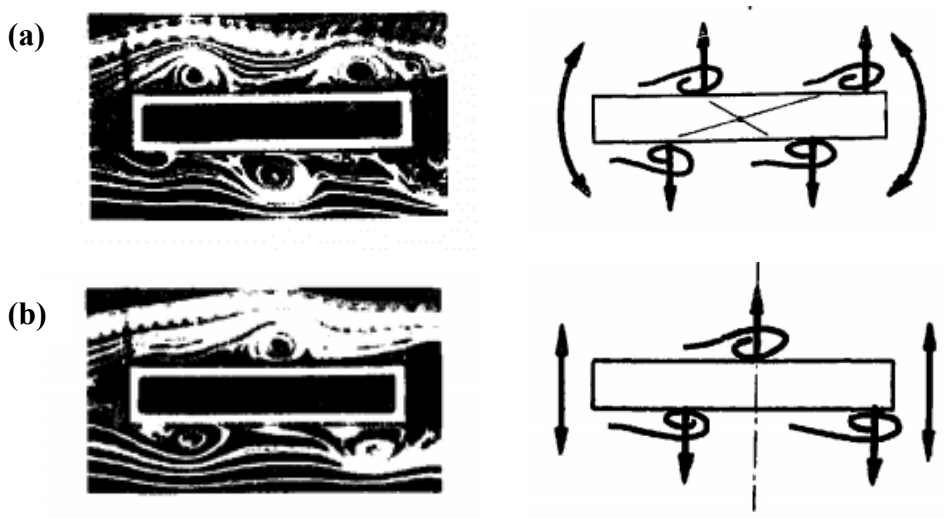

Figure 2.1.5 (a) Arrangement of the separated vortices from leading edge in the torsional and (b) heaving mode[8]

2.1.2 Conventional Conception on Secondary Vortex at Trailing Edge

Another feature of the motion-induced vortex vibration is the shedding of the secondary vortex at trailing edge. The secondary vortex at trailing edge is generated in the wake near the trailing edge in-phase with the separated vortex from leading edge due to the motion of the body. **Figure 2.1.6** shows the coherence in course of time of the separated vortex from leading edge and the secondary vortex at trailing edge for rectangular cross section with side ratio of B/D=2 (B: along-wind length, D: cross-wind length) at a reduced wind velocity of $V_r=V/fD$=4.15 (V: wind velocity, f: natural frequency), in a non-dimensional double amplitude of $2\eta/D$=0.30 (η: single-sided amplitude)[9]. The separated vortex from leading edge travels on the body surface, it reaches the trailing edge after one cycle of vibration and merges with the secondary vortex at trailing edge. Therefore, the motion-induced vortex vibration is considered to occur when the separated vortex combines with the secondary vortex at trailing edge in advance[9].

Figure 2.1.7 shows the V-A diagram of the region of the motion-induced vortex vibration for rectangular cross section with side ratio of B/D=2[9]. Three horizonal plates were installed at the downstream with a gap length X for the sake of eliminating regular vortices shedding into the wake. When the horizonal plates were installed at X/D=1, 0.167, the decrease of the maximum amplitude was confirmed. On the other hand, **Figure 2.1.8** shows fluctuating pressure coefficient distribution for rectangular

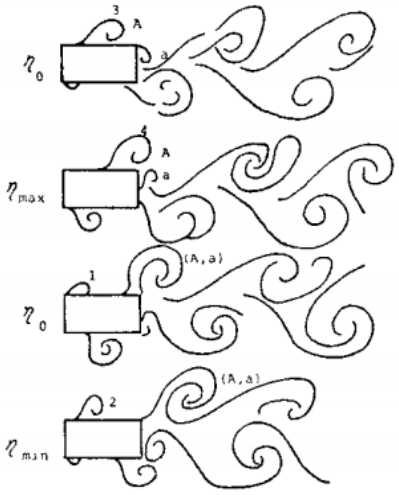

A: separated vortex from leading edge
a: secondary vortex at trailing edge

Figure 2.1.6 Flow patterns around rectangular section in forced heaving motion (B/D=2, Vr=4.15, $2\eta/D$=0.30)[9]

section of *B/D*=2 at the wind velocity where the motion-induced vortex vibration has occurred[9]. At the leeward part of the model, it is confirmed that the fluctuating pressure coefficient changed dramatically. These characteristics can be attributed to the influence of the secondary vortex at trailing edge. Thus, it can be considered that the stable shedding of the secondary vortex at trailing edge plays an important role in the motion-induced vortex vibration[9].

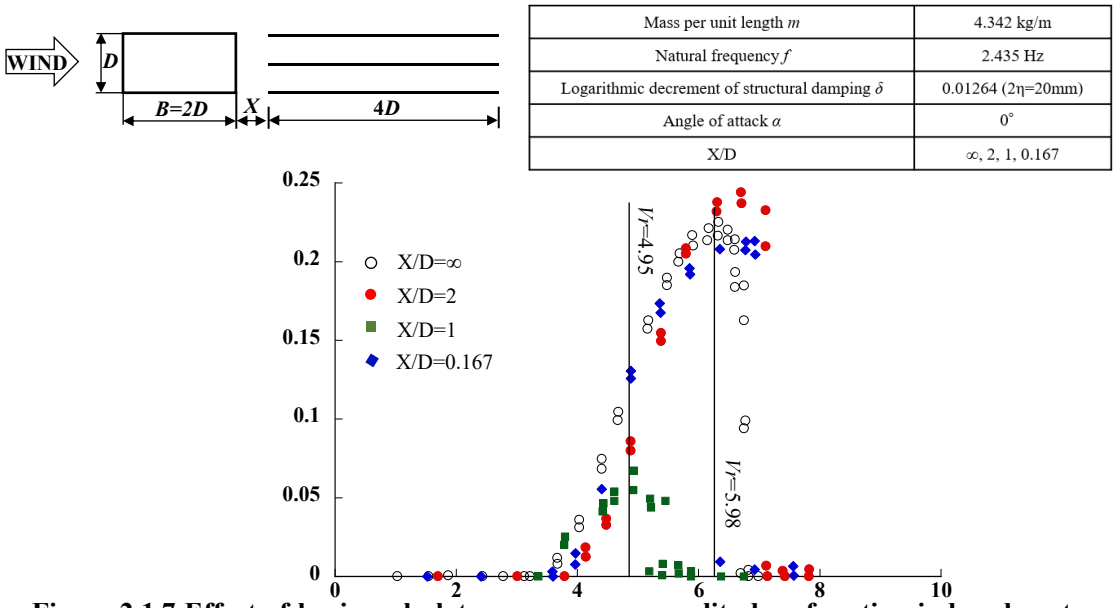

Mass per unit length *m*	4.342 kg/m
Natural frequency *f*	2.435 Hz
Logarithmic decrement of structural damping *δ*	0.01264 (2η=20mm)
Angle of attack *α*	0°
X/D	∞, 2, 1, 0.167

Figure 2.1.7 Effect of horizonal plates on response amplitudes of motion-induced vortex vibration for a rectangular section of *B/D*=2[9]

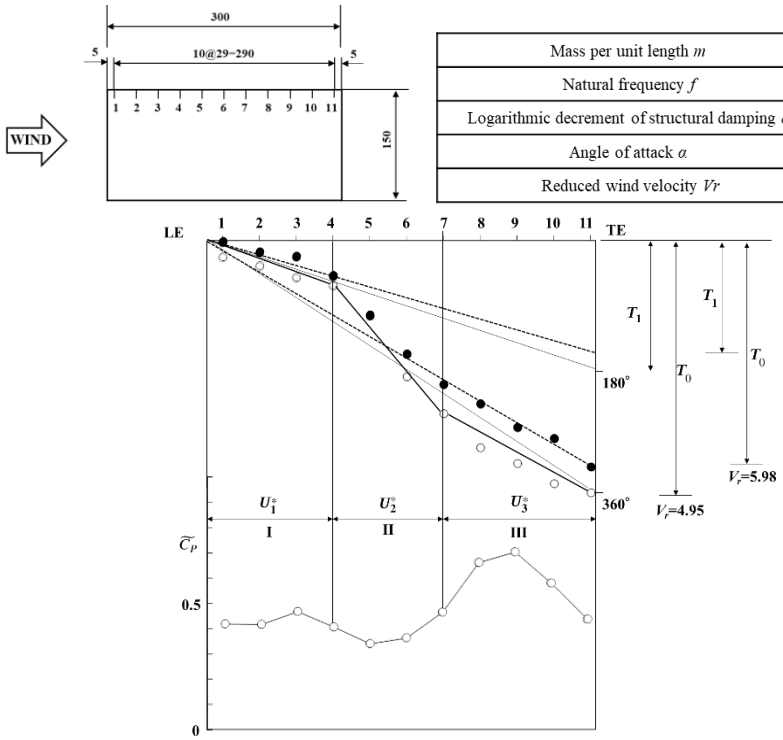

Mass per unit length *m*	4.342 kg/m
Natural frequency *f*	2.435 Hz
Logarithmic decrement of structural damping *δ*	0.01264 (2η=20mm)
Angle of attack *α*	0°
Reduced wind velocity *Vr*	4.95, 5.98

Figure 2.1.8 Fluctuating pressure coefficient distribution for a rectangular section of *B/D*=2[9]

2.2 Aerodynamic Characteristics of Motion-induced Vortex Vibration

In order to clarify the effect of the secondary vortex at trailing edge on the motion-induced vortex vibration, it is important to understand the basic aerodynamic characteristics of the motion-induced vortex. Hence, the response characteristics and fluctuation pressure distribution of the motion-induced vortex vibration obtained from previous study were introduced in this section.

2.2.1 Response Characteristics of Motion-induced Vortex Vibration

Figure 2.2.1 shows the relation between the onset reduced wind velocity of the vortex-induced vibration in the heaving mode and the side ratio for various sections such as rectangular and hexagonal sections[4]. Group 1 and 3 indicate the Kármán vortex-induced vibration, whereas Group 2 indicates the motion-induced vortex vibration. The motion-induced vortex vibration has been confirmed to occur on the cross sections with side ratios of B/D=2.0-8.0[4].

Figure 2.2.2 shows the schematic illustration of the unification of separated vortex from leading edge and secondary vortex at trailing edge[10]. The separated vortex from leading edge reaches to the trailing edge after n (n=1, 2, 3…) cycles of vibration

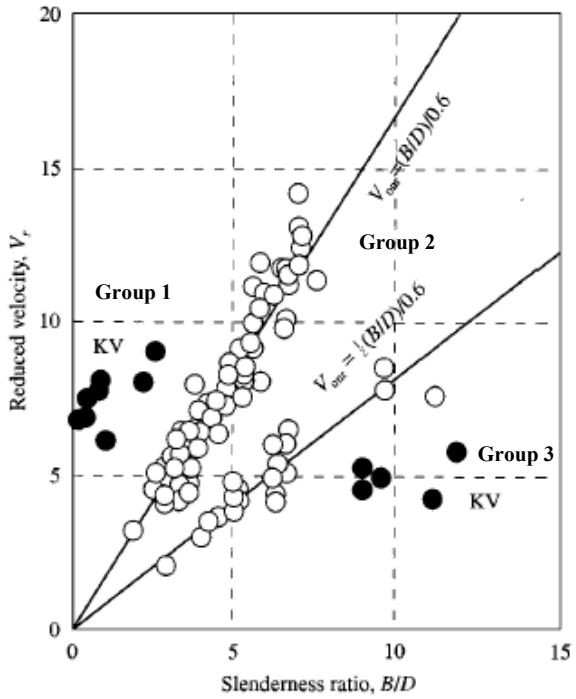

Figure 2.2.1 Onset reduced wind velocity of the motion-induced vortex vibration and side ratio[4]

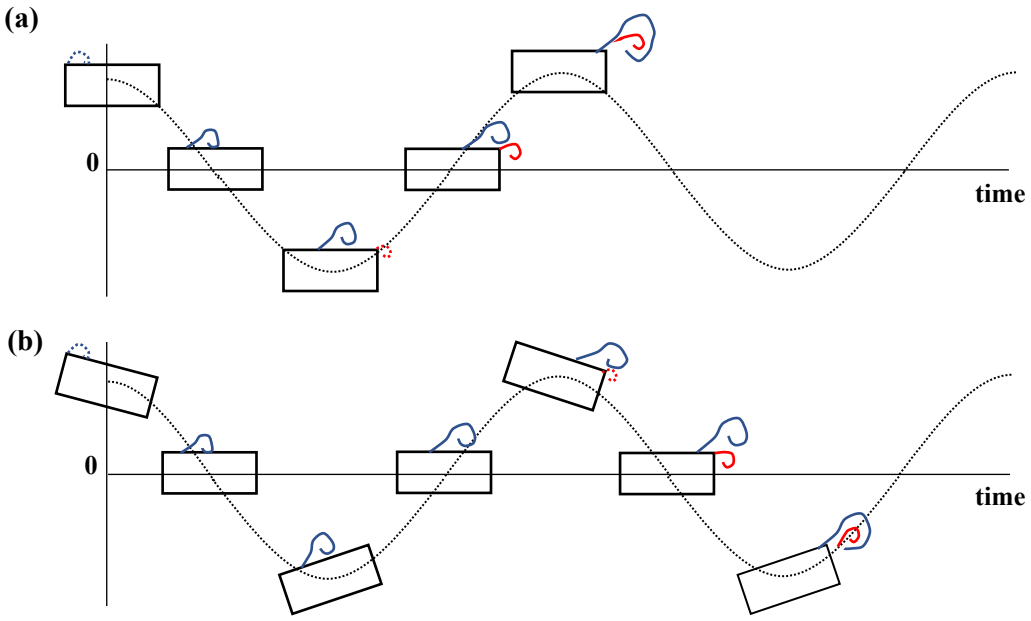

Figure 2.2.2 (a) Schematic illustration of the unification of separated vortex from leading edge and secondary vortex at trailing edge in the heaving mode and (b) torsional mode[10)]

for the heaving mode, $(2n-1)/2$ cycles for the torsional mode, respectively. In addition, the mean convection velocity of the separated vortex from leading edge on the body surface toward the trailing edge is evaluated as to be approximately 60% of the approaching flow velocity[4)]. Therefore, the onset reduced wind velocity of the motion-induced vortex vibration can be described as follows[4)]:

heaving mode:

$$V_{cr}=1/n\times 1.67B/D \tag{2.2.1}$$

torsional mode:

$$V_{cr}=2/(2n-1)\times 1.67B/D \tag{2.2.2}$$

On the other hand, it is suggested that the reduced wind velocity where the peak response amplitude of the motion-induced vortex vibration occurs also depends on the side ratio of the model[11)]. The fluctuating wind pressure distributing on the surface of the model does either positive or negative work according to the phase of the fluctuating wind pressure with respect to the displacement of the model. Typical instantaneous distribution of the work W on the surface of a rectangular cross section for various wind velocities can be illustrated as **Figure 2.2.3**[11)]. The work performing per unit area of the surface during one cycle of vibration is given in a non-dimensional

form as follows[11]:

$$W=Cp_0\,\eta_0 \sin\phi \tag{2.2.3}$$

where Cp_0 indicates the non-dimensional amplitude of the fluctuating wind pressure, η_0 and ϕ indicate the non-dimensional forced-oscillating amplitude and the phase difference between the pressure fluctuation and the displacement of the model, respectively. **Figure 2.2.3 (a)** shows the case when the wind velocity is relatively low, the convection velocity of the separated vortex from leading edge then becomes low. The first domain of the work $W>0$ appears near the center of the surface, while the second domain of $W>0$ appears at its leeward part. As the wind velocity increases, the patterns of distribution of W varies as shown in **Figure 2.2.3 (b)-(d)**. If the convection velocity of the separated vortex from leading edge becomes higher due to the increase in the wind velocity, the region of positive work is translated toward the leeward part from its position at low wind velocity. In higher wind velocity region, the convection velocity of the separated vortex from leading edge becomes so large that the region of positive work translates toward the leeward part, and finally leaves the model. The positive work attains its maximum value when the distribution of W changes from negative to positive at the center and at the quarter point of the span, as shown in **Figure 2.2.3 (c)** and **(a)**, respectively. Based on these distribution patterns of maximum

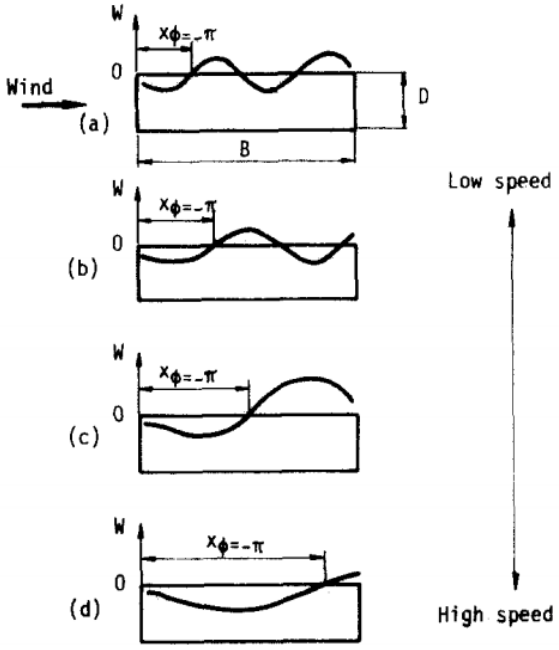

Figure 2.2.3 Distribution of work done by fluctuating pressure during one cycle and its variation with wind velocity[11]

positive work, the critical reduced wind velocity of the motion-induced vortex vibration where the peak response amplitude occurs can be estimated as follows[11]:

$$V_{cr}=2.4B/D + 0.5 \quad (2.2.4)$$

$$V_{cr}=1.2B/D + 0.5 \quad (2.2.5)$$

Figure 2.2.4 shows the *V-A* diagram of rectangular cross sections with side ratios of B/D=3, 4, 5 in the heaving mode with approximately the same Scruton number $Sc=2m\delta/\rho BD$ (m: mass per unite length, δ: logarithmic decrement of structural damping, ρ: air density)[12]. It is noted that the abscissa axis representing reduced wind velocity is based on the along-wind length B, instead of cross-wind length D. The motion-induced vortex vibrations were confirmed as occurring at the vicinity of V_{cr}=0.83, 1.6. In addition, a motion-induced vortex vibration with a tiny peak response amplitude for B/D=5 was also confirmed at approximately V_{cr}=0.5. As the side ratio becomes larger, it was confirmed that the peak response amplitudes of the motion-induced vortex vibrations whose onset wind velocity are V_{cr}=1.6 tend to become smaller. On the contrary, the peak response amplitudes of the motion-induced vortex vibrations with an onset wind velocity of V_{cr}=0.83 tend to become larger with the increase in the side ratio. Thus, it can be considered that as the side ratio becomes larger, the motion-induced vortex with a high onset wind velocity tends to become weak and shifts to lower wind velocity regions[12].

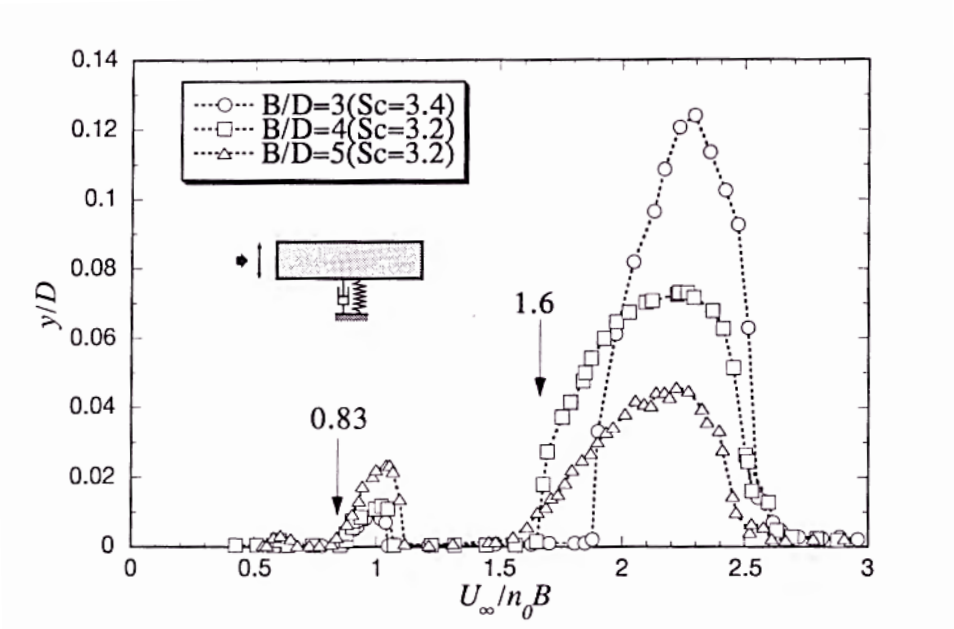

Figure 2.2.4 *V-A* diagram of rectangular cross sections with side ratios of *B/D*=3, 4, 5 in the heaving mode[12]

2.2.2 Fluctuating Wind Pressure Distribution in the Wind Velocity Region of Motion-induced Vortex Vibration

The displacement motion of the model in forced-oscillating vibration is assumed to be expressed as:

$$y(t)=A_0 \cos \omega t \tag{2.2.6}$$

where A_0, ω and t denote the forced-oscillating amplitude, circular frequency and time, respectively. The forced frequency component of the fluctuating wind pressure has a delay from the displacement and is expressed as:

$$C_p(t)=\left|C_p\right| \cos (\omega t+\beta) \tag{2.2.7}$$

where $\left|C_p\right|$ and β indicate the amplitude of the fluctuating wind pressure and the phase lag with respect to the displacement. Alternatively, equation (2.2.7) can be expressed in complex notation as:

$$C_p(t)=Re\left[(C_{pm}+iC_{pI})e^{i\omega t}\right] \tag{2.2.8}$$

where *Re* [ ] means the real part in the square bracket, C_{pm} and C_{pI} indicates the real and imaginary parts of the complex amplitude of the fluctuating wind pressure, respectively. From equation (2.2.7) and (2.2.8), the following relations can be obtained:

$$C_{pm}=\left|C_p\right| \cos \beta \tag{2.2.9}$$

$$C_{pI}=\left|C_p\right| \sin \beta \tag{2.2.10}$$

It should be noted that C_{pI} is in-phase with damping force. When $C_{pI}>0$, the fluctuating wind pressure does positive work to the vibration system.

Figure 2.2.5 shows the fluctuating wind pressure distribution C_{pI} for a rectangular cross section with a side ratio of *B/D*=2 at the reduced wind velocity where the motion-induced vortex occurred in the heaving mode[13]. As shown in **Figure 2.2.5**, C_{pI} shows negative values in the windward side and positive values in the leeward side. In other words, the damping force is composed on the windward side, whereas the exciting force is concentrated on the leeward part of the model. Such a force distribution can be related to the reattachment of a separated shear flow due to the motion[13].

Moreover, the fluctuating wind pressure distribution characteristics for a rectangular cross section with a side ratio of *B/D*=4 also show a similar tendency to *B/D*=2 in the heaving mode. **Figure 2.2.6** and **Figure 2.2.7** show the fluctuating wind

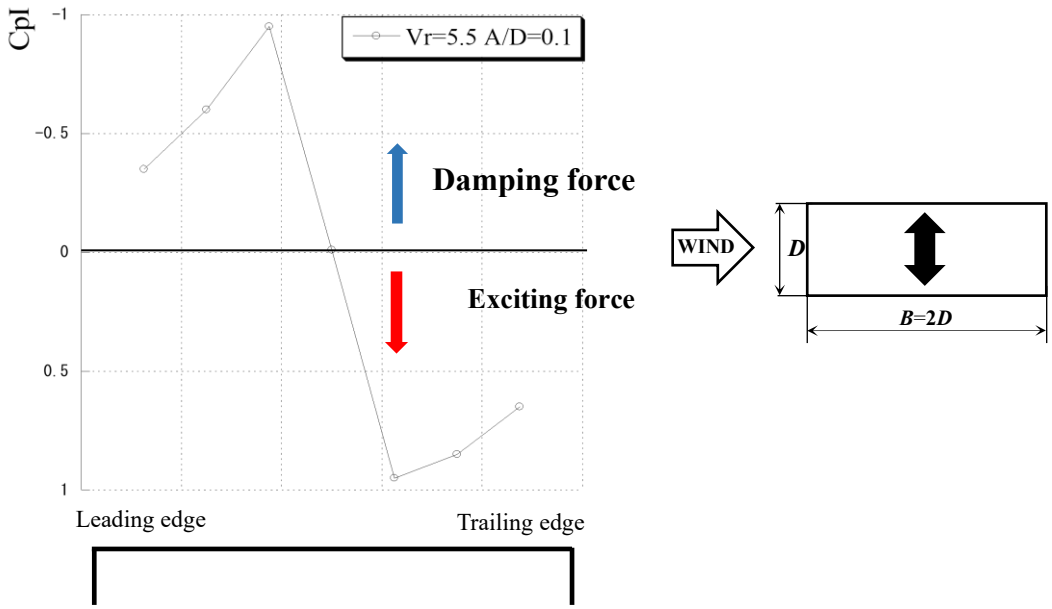

Figure 2.2.5 Fluctuating wind pressure distribution for *B/D*=2 in the wind velocity region of motion-induced vortex vibration in the heaving mode[13)]

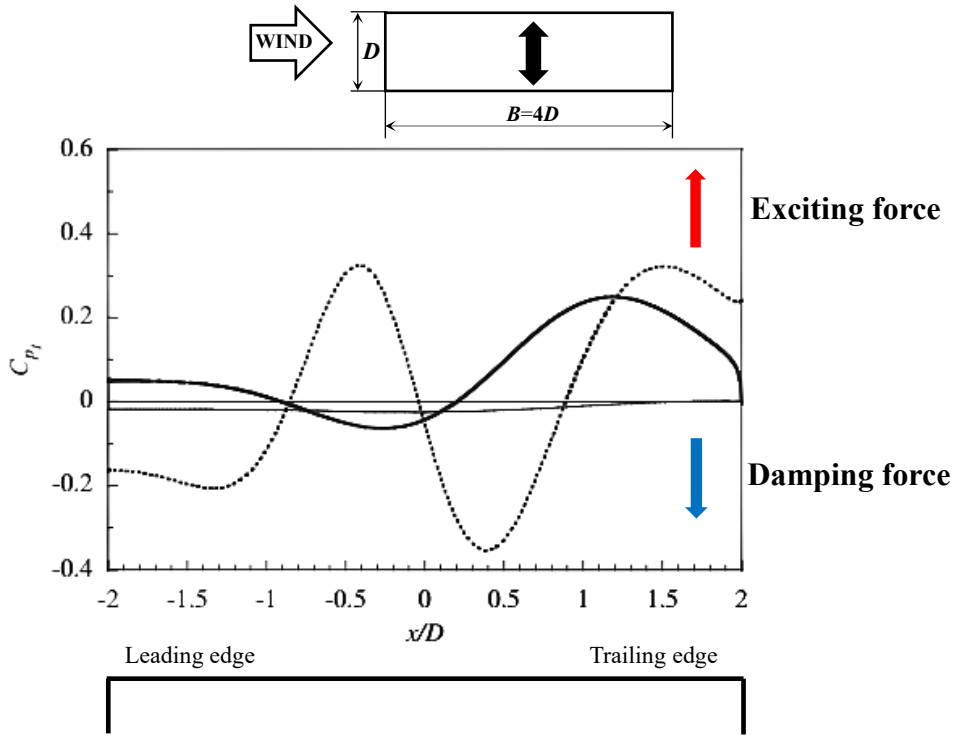

Figure 2.2.6 Fluctuating wind pressure distribution for *B/D*=4 in the wind velocity region of motion-induced vortex vibration in the heaving mode (*η/D*=0.02, dotted line: V_r=4, solid line: V_r=8)[14)]

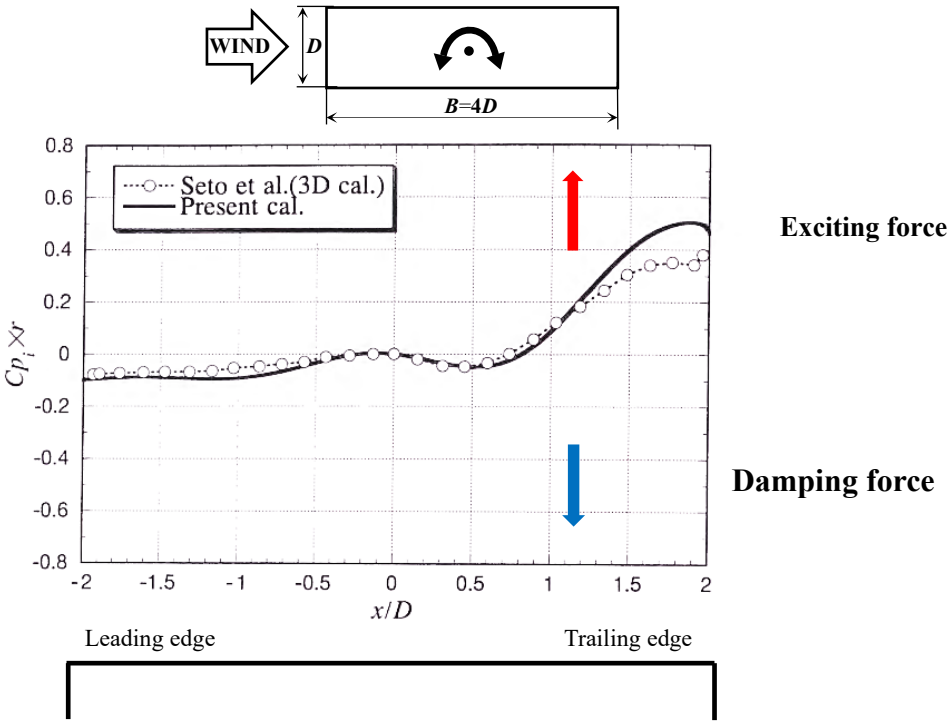

Figure 2.2.7 Fluctuating wind pressure distribution for *B/D*=4 in the wind velocity region of motion-induced vortex vibration in the torsional mode (ϕ=0.52°, V_r=5.67)[12)]

pressure distribution for a rectangular cross section with a side ratio of *B/D*=4 at the reduced wind velocity where the motion-induced vortex occurred in the heaving and torsional mode, respectively[12), 14)]. The fluctuating wind pressure C_{pI} is positive in the leeward side of the model in both the heaving and torsional mode. Thus, regarding a rectangular cross section of *B/D*=4, when the motion-induced vortex vibration occurs, the exciting force acts on the leeward side regardless of the vibration mode[12), 14)].

2.3 Aerodynamic Characteristics of the Bracing Member in Ikitsuki Bridge

According to the results of wind tunnel tests for the cross section of the bracing member in Ikitsuki Bridge, it is suggested that the motion-induced vortex vibration might occur without the formation of the secondary vortex at trailing edge[15)]. Hence, the role of the secondary vortex at trailing edge in the motion-induced vortex vibration is not totally clear. This study therefore regards it as a trigger to carry out a series of wind tunnel tests for the sake of investigating the role of the secondary vortex at trailing edge in the motion-induced vortex vibration. In order to clarify the research motivation of this study more explicitly, the aerodynamic characteristics of the bracing

member in Ikitsuki Bridge were introduced in this section.

2.3.1 Response Characteristics of the Bracing Member in Ikitsuki Bridge

The cross section of the bracing member of Ikitsuki Bridge is composed of a rectangular cross section with a side ratio of B/D=1.18 and a flange attached at each corner of the cross section. **Figure 2.3.1** shows the *V-A* diagram for the bracing member of Ikitsuki Bridge and rectangular cross sections with an angle of attack α=0°[15]. Aerodynamic vibrations were confirmed at the vicinity of V_r=2 and 8. The vibrations confirmed as occurring at V_r=2 were suggested to be the motion-induced vortex vibration, as the onset reduced wind velocities correspond to the empirical onset wind velocity of the motion-induced vortex vibration V_{cr}=1.67B/D=2.0. The maximum response amplitudes of the motion-induced vortex vibrations for both cross sections nearly have the same value. Thus, when the angle of attack is 0°, it is suggested that the effect of the flange on the maximum response amplitude of the motion-induced vortex vibration is extremely small. However, **Figure 2.3.2** shows the *V-A* diagram for the two cross sections with an angle of attack α=10°[15]. The maximum response amplitude in the case with flanges is approximately 1.5 times larger than that in the case with no flanges. In other words, it turns out that as the angle of attack becomes

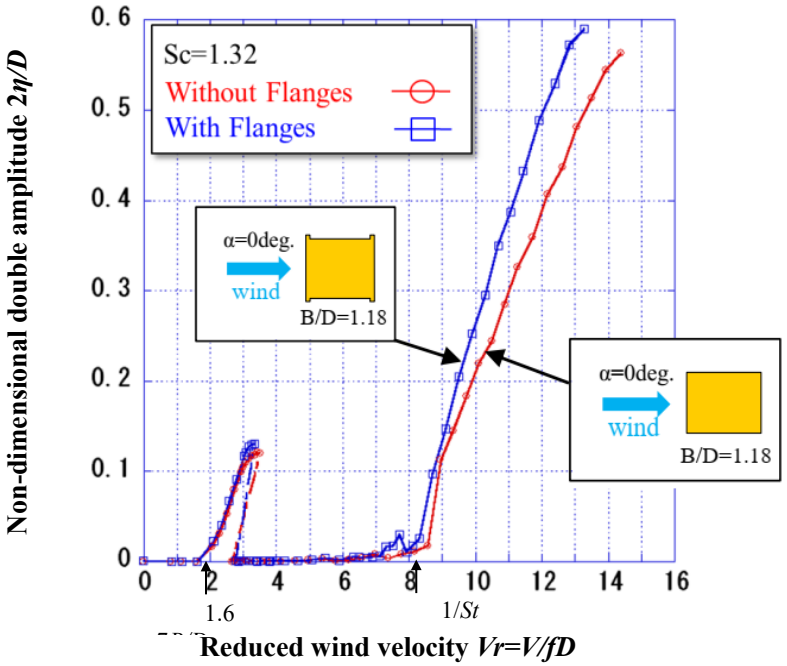

Figure 2.3.1 *V-A* diagram of the bracing member of Ikitsuki Bridge and rectangular cross sections of B/D=1.18 (α=0°)[15]

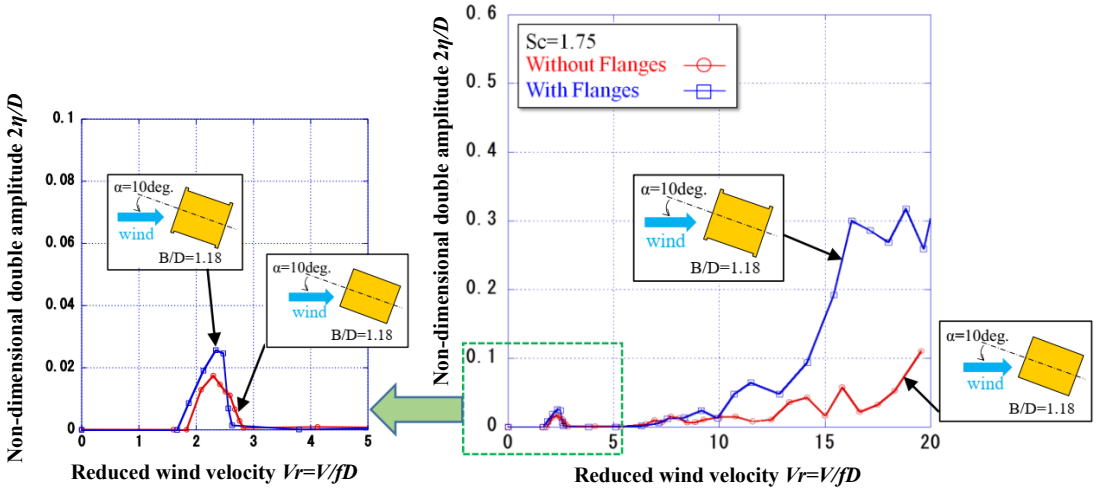

Figure 2.3.2 *V-A* diagram of the bracing member of Ikitsuki Bridge and rectangular cross sections of *B/D*=1.18 (*α*=10°)[15)]

larger, the existence of flange tends to exercise an effect on the patterns of the flows around the cross section[15)].

The Strouhal number *St* measured on the cross section with flanges was *St*=0.124[15)]. Its inverse number is the critical onset reduced wind velocity of the Kármán vortex-induced vibration. In other words, because V_r=1/*St*=8.1, a vibration beginning in the vicinity of a reduced wind velocity of V_r=8 can be judged as the Kármán vortex-induced vibration. Furthermore, from the fact that the Scruton number *Sc*=1.32 in this case was small, it was found that the Kármán vortex-induced vibration changed to a galloping along with the increase in wind velocity.

2.3.2 Measurement of Unsteady Aerodynamic Lift for the Bracing Member in Ikitsuki Bridge

The unsteady aerodynamic lift obtained by the forced oscillation method is shown by the following equation[16), 17)]:

$$Lift = \pi\rho D^3\omega^2 \left(C_{L\eta R} + iC_{L\eta i}\right)\frac{\eta}{D} \tag{2.3.1}$$

where *Lift* is the unsteady aerodynamic lift per unit length [N/m], ρ: air density [kg/m^3], ω: circular frequency of the forced oscillation [rad/s], $C_{L\eta R}$: real part of unsteady aerodynamic lift coefficients, $C_{L\eta i}$: imaginary part of unsteady aerodynamic lift coefficients, η: vertical oscillation amplitude [m] and *D*: height of model [m].

Substituting equation (2.3.1) into the external force term of the equation of motion and the following equations can be obtained:

$$m\ddot{\eta} + c\dot{\eta} + k\eta = \pi\rho D^3\omega^2\{(C_{L\eta R} + iC_{L\eta i})\frac{\eta}{D}\} \quad (2.3.2)$$

where m: mass, c: damping coefficient, k: stiffness.

$$m\ddot{\eta} + (c - \pi\rho D^2\omega C_{L\eta i})\dot{\eta} + (k - \pi\rho D^2\omega^2 C_{L\eta R})\eta = 0 \quad (2.3.3)$$

$$c - \pi\rho D^2\omega C_{L\eta i} < 0 \quad (2.3.4)$$

Accordingly, from equation (2.3.4), if the damping constant c is very small, and $C_{L\eta i}$ is a positive value, it means that the structure is aerodynamically unstable.

Figure 2.3.3 shows unsteady aerodynamic lift coefficients $C_{L\eta i}$ for the bracing

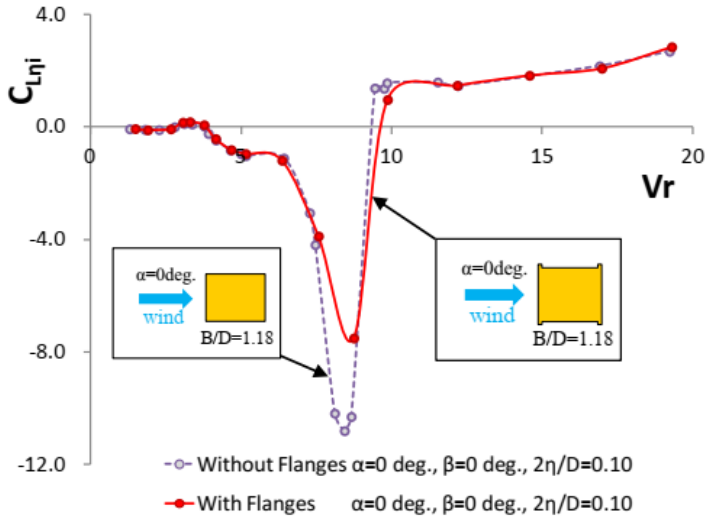

Figure 2.3.3 Unsteady aerodynamic lift coefficients $C_{L\eta i}$ for the bracing member of Ikitsuki Bridge and rectangular cross sections[18)]

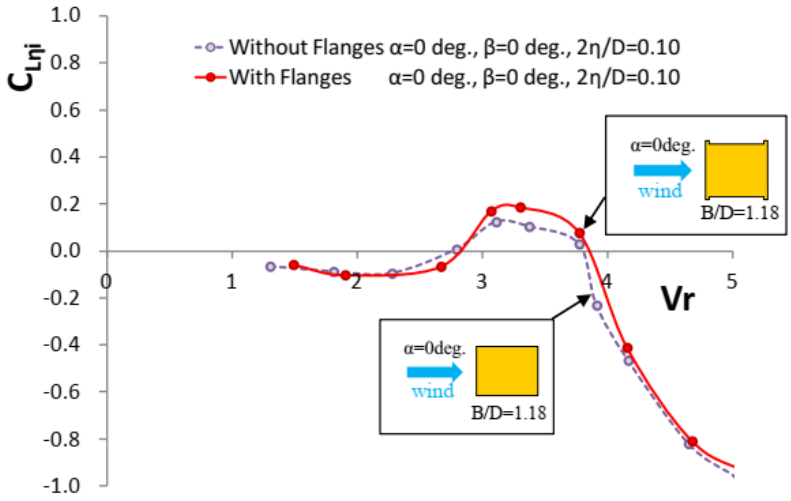

Figure 2.3.4 Unsteady aerodynamic lift coefficients $C_{L\eta i}$ for the bracing member of Ikitsuki Bridge and rectangular cross sections (enlarged view of Figure 2.3.3)[18)]

member of Ikitsuki Bridge and rectangular cross sections[18]. **Figure 2.3.4** shows an enlarged view of **Figure 2.3.3** in the wind velocity range of V_r=0-5[18]. $C_{L\eta i}$ in the ranges of the wind velocity of the motion-induced vortex vibration and the Kármán vortex-induced vibration are positive values and they correspond to the results of the spring-supported tests shown in **Figure 2.3.1**. A similar unsteady aerodynamic lift characteristic at a low wind velocity region was also confirmed for a rectangular cross section with side ratio of B/D=1.0 from previous wind tunnel tests[19), 20), 21)].

2.3.3 Flow Patterns around Rectangular Cross Sections with Small Side Ratios

Figure 2.3.5 shows the results of flow visualization tests for rectangular cross section of B/D=1.18[22)]. When the model was at rest, only the Kármán vortex were formed in the wake of the model, as shown in **Figure 2.3.5 (a)**. At the onset wind velocity of the motion-induced vortex vibration V_{cr}=1.67B/D=2.0 in a forced-oscillating amplitude of $2\eta/D$=0.10, although the formation of the separated vortex from leading edge were confirmed, there were no secondary vortex at trailing edge formed as shown in **Figure 2.3.5 (b)**. According to the conventional conception on the motion-induced vortex vibration, the generation of motion-induced vortex vibration is considered to be caused by the unification of the separated vortex from leading edge and the secondary vortex at trailing edge[4)]. Nevertheless, according to the results of the spring-supported tests and the measurement of the unsteady lift for rectangular cross section of B/D=1.18, the aerodynamic vibration occurring at V_r=2.0 was suggested to be the motion-induced vortex vibration, as shown in **Figure 2.3.1** and **Figure 2.3.4**. Therefore, it can be considered that the motion-induced vortex vibration would possibly occur at the range of low wind velocity even in the cases of side ratio

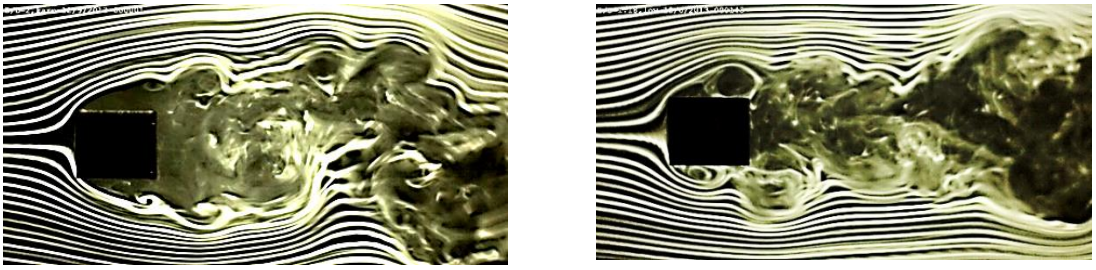

(a) At rest **(b) V_r=2.0, $2\eta/D$=0.10 (at the top displacement)**

Figure 2.3.5 Results of flow visualization tests for rectangular cross section of B/D=1.18[22)].

where the secondary vortex at trailing edge was not confirmed.

Figure 2.3.6-Figure 2.3.10 show the results of flow visualization tests for rectangular cross section of B/D=0.50-1.5 at the empirical onset wind velocity of the motion-induced vortex vibration V_{cr}=1.67B/D[22]. In the experimental results with non-dimensional double amplitude $2\eta/D$=0.050, the generation of the separated vortex from leading edge were confirmed in all cross sections. However, as a result of non-

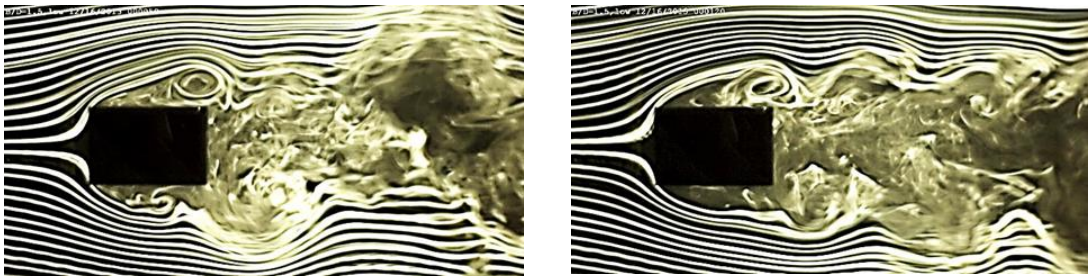

(a) $2\eta/D$=0.050 **(b) $2\eta/D$=0.025**

Figure 2.3.6 Results of flow visualization tests for rectangular cross section of B/D=1.5 (V_r=1.67B/D=2.5, at the top displacement) [22]

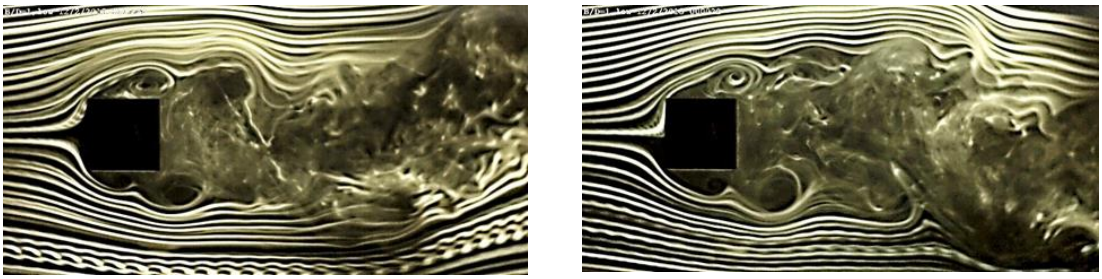

(a) $2\eta/D$=0.050 **(b) $2\eta/D$=0.025**

Figure 2.3.7 Results of flow visualization tests for rectangular cross section of B/D=1.0 (V_r=1.67B/D=1.7, at the top displacement) [22]

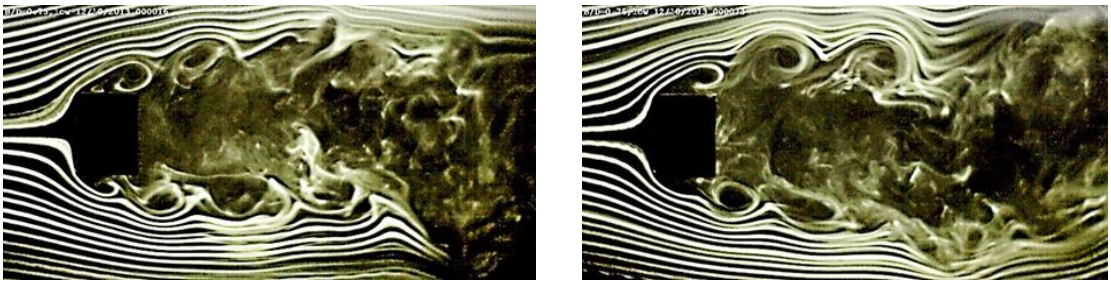

(a) $2\eta/D$=0.050 **(b) $2\eta/D$=0.025**

Figure 2.3.8 Results of flow visualization tests for rectangular cross section of B/D=0.75 (V_r=1.67B/D=1.3, at the top displacement) [22]

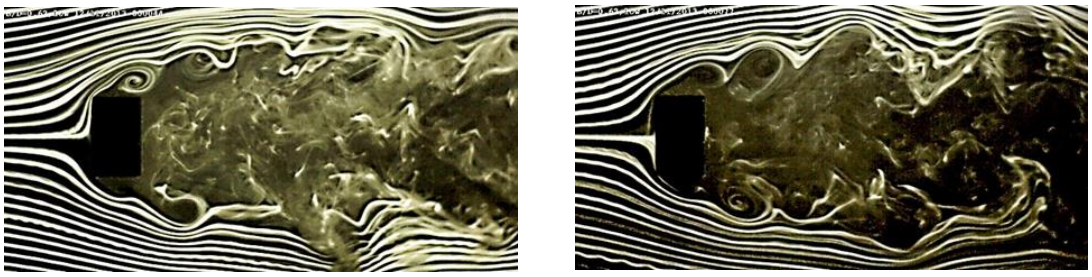

(a) $2\eta/D$=0.050 **(b) $2\eta/D$=0.025**

Figure 2.3.9 Results of flow visualization tests for rectangular cross section of B/D=0.62 (V_r=1.67B/D=1.0, at the top displacement) [22)]

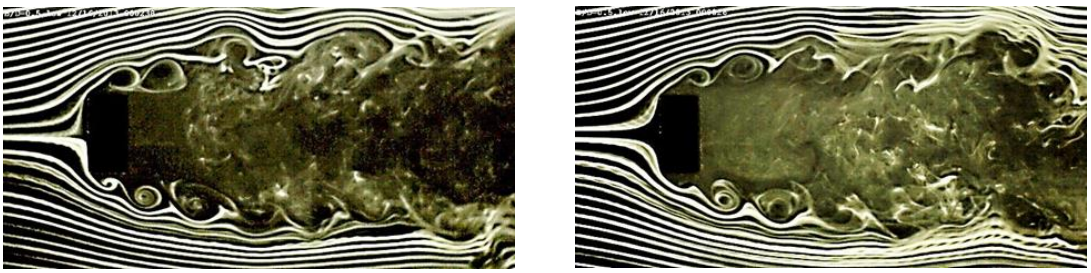

(a) $2\eta/D$=0.050 **(b) $2\eta/D$=0.025**

Figure 2.3.10 Results of flow visualization tests for rectangular cross section of B/D=0.50 (V_r=1.67B/D=0.8, at the top displacement) [22)]

dimensional double amplitude $2\eta/D$=0.025, the separated vortex from leading edge were gradually separating from the top and bottom surfaces of the cross sections with side ratios less than B/D=0.62 and flowing downward. The generation of secondary vortices at trailing edge was not confirmed clearly in all cross sections with side ratios less than B/D=1.5. Thus, a possibility was suggested that motion-induced vortex vibration might be generated even at side ratios of less than B/D=2.0 where the generation of secondary vortices at trailing edge was not confirmed. Regarding this consideration, further investigation should be undertaken to confirm.

References

1) Naudascher, E. and Wang, Y., 1993. Flow-induced vibrations of prismatic bodies and grids of prisms, Journal of Fluids and Structures, 7, 341-373.
2) Parker, R. and Welsh, M. C., 1981. The effect of sound on flow over bluff bodies, International Journal Heat and Fluid Flow, 4, 113-127.
3) Rockwell, D. and Naudascher, E., 1979. Self-sustained oscillations of impinging free shear layers, Annual Review of Fluid Mechanics, 11, 67-94.
4) Shiraishi, N. and Matsumoto, M., 1983. On classification of vortex-induced oscillation and its application for bridge structures, Journal of Wind Engineering and Industrial Aerodynamics, 14 (1-3), 419-430.
5) Ohya, Y., Nakamura, Y., Ozono, S., Tsuruta, H. and Nakayama, R., 1992. A numerical study of vortex shedding from flat plates with square leading and trailing edges, Journal of Fluid Mechanics, 236, 445-460.
6) Nakamura, Y., Ohya, Y. and Tsuruta, Y., 1991. Experiments on vortex shedding from flat plates with square leading and trailing edges, Journal of Fluid Mechanics, 222, 437-447.
7) Stokes, A. N., and Welsh, M. C., 1986. Flow-resonant sound interaction in a duct containing a plate; II: Square leading edge, Journal of Sound and Vibration, 104, 55-73.
8) Kubo, Y., Hirata, K. and Mikawa, K., 1992. Mechanism of aerodynamic vibrations of shallow bridge girder sections, Journal of wind Engineering and Industrial Aerodynamics, 41-44, 1297-1308.
9) Shiraishi, N. and Matsumoto, M., 1982. On vortex-induced oscillations of bluff cross sections used for bridge structures, Proceedings of the Japan Society of Civil Engineers, 322, 37-50. (in Japanses)
10) Shiraishi, N. and Matsumoto, M., 1984. On physical mechanism of vortex-induced oscillation and its response evaluation, Wind Engineers, Japan Association for Wind Engineering, No. 20, 103-127. (in Japanese)
11) Komatsu, S. and Kobayashi, H., 1980. Vortex-induced oscillation of bluff cylinders, Journal of Wind Engineering and Industrial Aerodynamics, 6, 335-362.
12) Shimada, K., 1999. Evaluation of aerodynamic characteristics and aerodynamic elasticity behavior forecast of rectangular cylinders using k-ε model, Doctor's thesis, Kyoto University. (in Japanese)

13) Miyata, T., Miyazaki, M. and Yamada, H., 1983. Pressure distribution measurements for wind induced vibrations of box girder bridges, Journal of wind Engineering and Industrial Aerodynamics, 14, 223-234.
14) Shimada, K. and Ishihara, T., 2012. Predictability of unsteady two-dimensional *k*-ε model on the aerodynamic instabilities of some rectangular prisms, Journal of Fluids and Structures, 28, 20-39.
15) Matsuda, K., Kato, K., Tamai, Y. and Suda, K., 2016. Experimental study on aerodynamic vibrations of rectangular cross sections having low side ratios, Proceedings of 8th International Colloquium on Bluff Body Aerodynamics and Applications, Boston, USA.
16) Luo, S. C. and Bearman, P. W., 1990. Predictions of fluctuating lift on a transversely oscillating square-section cylinder, Journal of Fluids and Structures, 4, 219-228.
17) Bearman, P. W. and Luo, S. C., 1988. Investigation of the aerodynamic instability of a square-section cylinder by forced oscillation, Journal of Fluids and Structures, 2, 161-176.
18) Tamai, Y., Matsuda, K., Kato, K., Misawa, K. and Ikeda, I., 2014. Experimental study on aerodynamic vibration of a bracing member with a rectangular cross section of the long-spanned truss bridge, Proceedings of the 23rd National Symposium on Wind Engineering, 211-216. (in Japanese)
19) Yagi, T., Shinjo, K., Narita, S., Nakase, T. and Shirato, H., 2013. Interferences of vortex sheddings in galloping instability of rectangular cylinders, Journal of Structural Engineering, Japan Society of Civil Engineers, 59A, 552-561. (in Japanese)
20) Nakamura, Y. and Mizota, T., 1975. Unsteady lifts and wakes of oscillating rectangular prisms, Journal of the Engineering Mechanics Division, American Society of Civil Engineers, 101, 6, 855-871.
21) Mizota, T. and Okajima, A., 1982. Experimental studies of flow patterns around oscillating rectangular prisms and their unsteady aerodynamic forces, Proceedings of the Japan Society of Civil Engineers, 327, 49-60. (in Japanese)
22) Matsuda, K., Kato, K., Tamai, Y., Misawa, K. and Ikeda, I., 2015. Experimental study on aerodynamic vibrations of a bracing member with a rectangular cross section of the long-spanned truss bridge, Proceedings of 14th International Conference on Wind Engineering, Porto Alegre, Brazil.

Chapter 3: The Role of Secondary Vortex at Trailing Edge in Motion-induced Vortex Vibration for Rectangular Cylinders with Small Side Ratios

In general, the motion-induced vortex vibration is considered to be caused by the unification of the separated vortex from leading edge and the secondary vortex at trailing edge[1]. However, the aerodynamic characteristics of the bracing member in Ikitsuki Bridge has revealed that the motion-induced vortex vibration in the heaving mode might occur without the formation of the secondary vortex at trailing edge, regarding a rectangular cross section with a side ratio of B/D=1.18[2]. On the other hand, the motion-induced vortex vibration is considered to occur on the rectangular cross sections with side ratio of B/D=2.0-8.0, according to the previous wind tunnel tests[1]. A rectangular cross section with a side ratio of B/D=1.18 is not the acknowledged cross section where the motion-induced vortex vibration has been confirmed to occur. Thus, this chapter concentrates on rectangular cross sections with small side ratios. Spring-supported and flow visualization tests for rectangular cross sections with side ratios of B/D=0.50-1.18 were carried out, for the purpose of clarifying the role of the secondary vortex at trailing edge in the motion-induced vortex vibration for rectangular cross sections with small side ratios.

3.1 Wind Tunnel Tests for Rectangular Cylinders of B/D=0.50-1.18 in the Heaving Mode

3.1.1 Spring-supported Tests

(1) Wind tunnel

In order to obtain the response characteristics of the target rectangular cross sections, the spring-supported tests in the heaving mode were conducted in a closed circuit wind tunnel at Kyushu Institute of Technology. **Figure 3.1.1** shows the schematic illustration of the closed circuit wind tunnel. **Table 3.1.1** shows the specification of the closed circuit wind tunnel. The spring-supported tests were carried

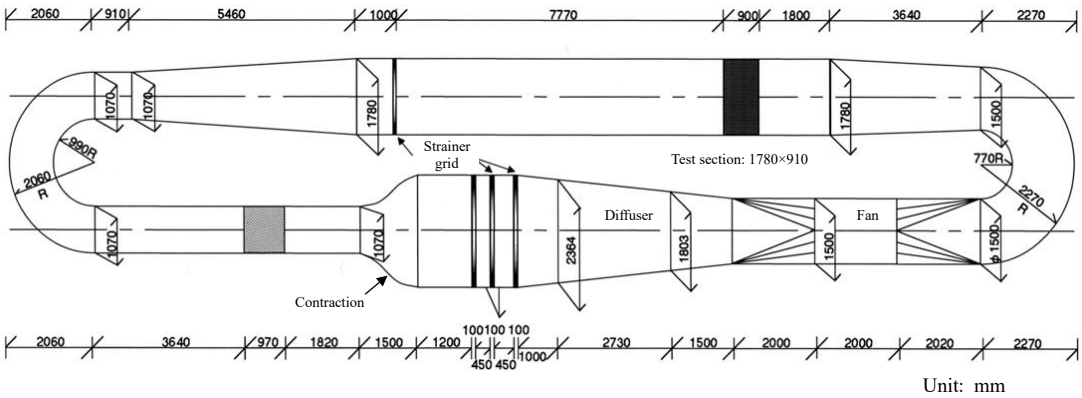

Figure 3.1.1 Schematic illustration of the closed circuit wind tunnel

Table 3.1.1 Specification of the closed circuit wind tunnel

Test section	Height	1780mm
	Width	910mm
Fan	Air quantity	34.3m^3/sec
	Rotational speed	80-800r.p.m
Electric motor	Output	30kw, 200V
	Rotational speed	150-1500r.p.m

out in a smooth flow with a turbulence of less than 0.5%. The wind velocity V in the spring-supported tests was from 1.5m/s to 10m/s. The Reynolds number in the wind velocity region of the motion-induced vortex vibration was $Re=VD/\nu=1.8\times10^4$-4×10^4, where V: wind velocity (m/s), D: cross-wind length (m), ν: kinematic viscosity (m^2/s).

(2) Specifications of target models

Rectangular cross sections with side ratios of B/D=0.50, 0.62, 0.75, 1.0, 1.18 were selected as the target cross sections. The model of B/D=0.50 was constructed of cypress wood attached with two end plates at both ends of the model, in order to make the flow around the models appear as a two-dimensional flow. The models of B/D=0.62, 0.75, 1.0, 1.18 were the composed of the model of B/D=0.50 and polystyrene foams whose purpose was to alter the side ratios of the models. **Figure 3.1.2** shows the model of B/D=1.0 used in spring-supported tests. It should be noted that as the side ratios of the models are smaller than B/D=2.0, the onset reduced wind velocities of the motion-induced vortex vibrations are very low, because it has been suggested that the onset reduced wind velocity of the motion-induced vortex vibration depends on the side ratio of the model[1)]. However, in order to ensure that the wind in the wind tunnel is a smooth

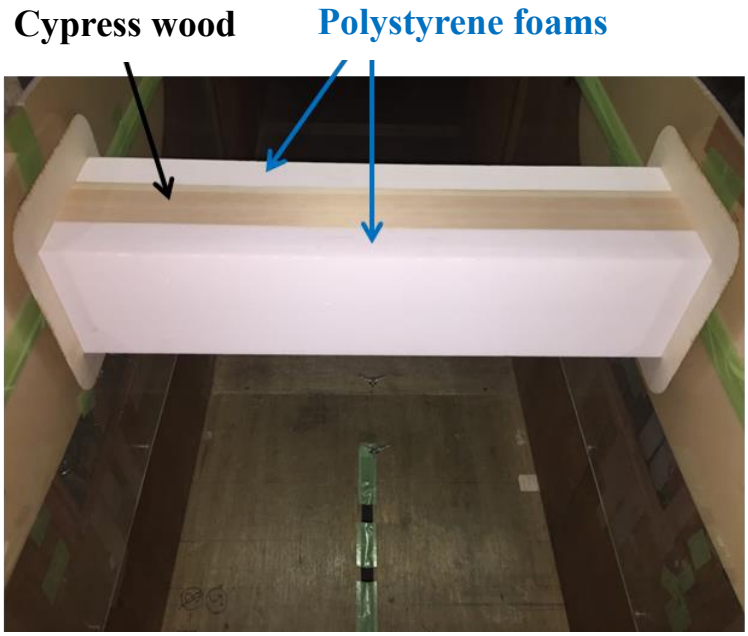

Figure 3.1.2 Sectional model of *B/D*=1.0 in the wind tunnel

Table 3.1.2 The size of the target models used in spring-supported tests

Side ratio *B/D*	1.18	1.0	0.75	0.62	0.5
Along-wind length *B*(mm)	212.4	180	135	111.6	90
Cross-wind length *D*(mm)	180				
Model length *L*(mm)	828				
Aspect ratio *L/D*	4.6				

flow, the wind velocity in the wind tunnel must be set at no less than 1.5m/s. Therefore, larger models with a cross-wind length of *D*=180mm were used and the blockage ratio in the spring-supported tests was moderated to 10%. **Table 3.1.2** shows the size of the target models.

(3) Measurement system

Figure 3.1.3 shows the schematic illustration of the suspension apparatus for the spring-supported tests in the heaving mode. The models were suspended in the wind tunnel by two coil springs at each side. The vibration system was so well designed that the structural damping of the vibration system could be reduced to as a small value as possible. Further, in order to ensure that the spring-supported tests for the models with

side ratios of *B/D*=0.50, 0.62 can be conducted normally in both low and high reduced wind velocity regions, two different springs were used in the cases with side ratios of *B/D*=0.50, 0.62 due to the restriction of wind velocity range. The spring with a high natural frequency was used in the low reduced wind velocity region. On the contrary, the spring with a low natural frequency was used in the high reduced wind velocity region. Therefore, the results of spring-supported test for the cases with side ratios of *B/D*=0.50, 0.62 were composed of both the result obtained by using the spring with a high natural frequency and the result obtained by using the spring with a low natural frequency.

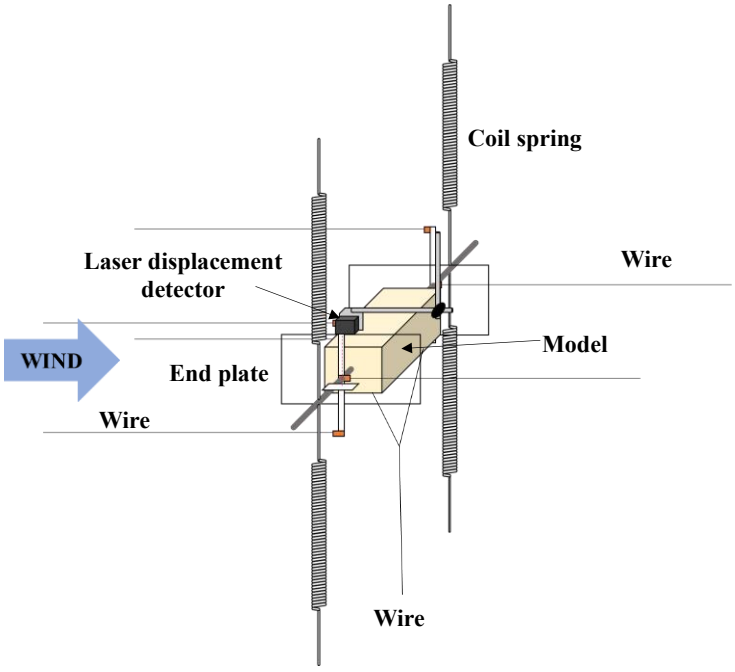

Figure 3.1.3 Schematic illustration of the suspension apparatus

Figure 3.1.4 shows the setting situation of the magnetic dampers. The magnetic dampers which connect the model with two metal wires was installed under the floor of the wind tunnel, in order to adjust the structural damping of the vibration system.

In the measurement system, the response amplitude, divergence and decrement of the models during vibration were measured by a laser displacement detector. The measured data was converted to digital data via an analog-to-digital converter after passing through a low-pass filter. Then the digital data was stored in a computer. Meanwhile, a spectral analysis was carried out by the computer in order to determine the response amplitude, frequency and logarithmic decrement of structural damping. The processing and storage of the data were conducted by the LabVIEW software. The

Figure 3.1.4 Setting situation of the magnetic dampers

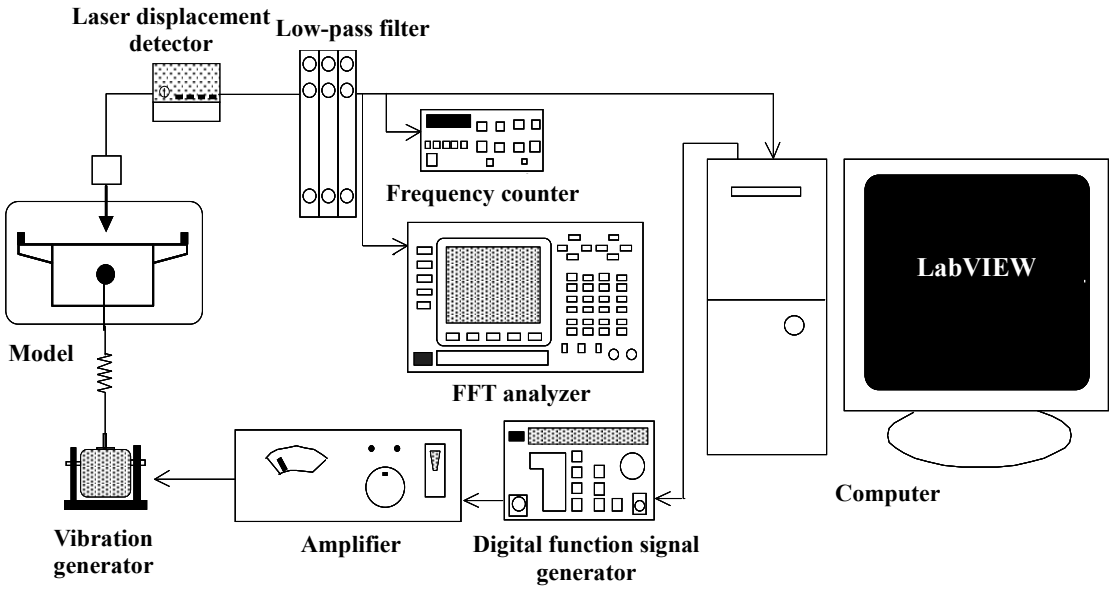

Figure 3.1.5 Measurement system of spring-supported tests

measurement system is shown in **Figure 3.1.5**.

(4) Experimental conditions of spring-supported tests

Table 3.1.3 shows the experimental conditions for the spring-supported tests. The Scruton number *Sc* for each cross section was adjusted as the same value. In addition, in order to get a better grasp on the response characteristics of the motion-induced vortex vibration for the models with small side ratios, spring-supported test for the cases with side ratios of *B/D*=0.50, 0.62 were conducted in the low wind velocity region again when the Scruton number *Sc* was set as minimum.

Table 3.1.3 Experimental conditions for spring-supported tests

B/D	*B* (mm)	*D* (mm)	Natural frequency *f* (Hz)	Air density ρ (kg/m^3)	Mass per unit length *m* (kg/m)	Logarithmic decrement of structural damping δ	*Sc* $=2m\delta/\rho D^2$
0.50	90	180	13.28	1.20	3.67	0.0065	1.2
			13.12	1.20	3.79	0.0083	1.6
			6.12	1.23	3.27	0.0097	1.6
0.62	111.6	180	10.13	1.20	3.69	0.0043	0.8
			10.05	1.20	3.82	0.0082	1.6
			6.24	1.23	3.14	0.0101	1.6
0.75	135	180	9.07	1.20	3.62	0.0086	1.6
1.0	180	180	6.70	1.20	3.61	0.0086	1.6
1.18	212.4	180	5.64	1.20	3.67	0.0085	1.6

Model length: 828mm

(5) Measurement of the Strouhal number

In order to better understand the response characteristics of the target models, the measurement of the Strouhal number *St* was also carried out. The models used in the measurement of the Strouhal number were the same as the models used in spring-supported tests. **Figure 3.1.6** shows the schematic illustration of the measurement position for the I-type probe. The measurement positions of the Strouhal number *St* are shown in **Table 3.1.4.**

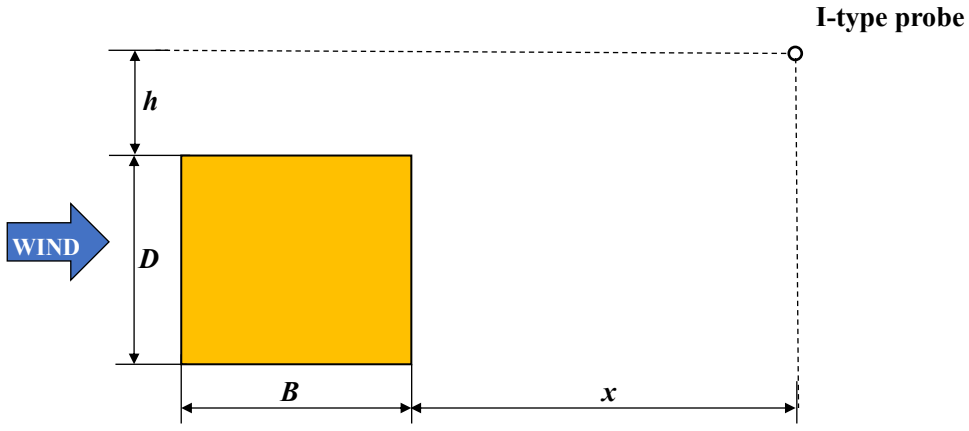

Figure 3.1.6 Schematic illustration of the measurement position for the I-type probe

Table 3.1.4 Measurement position of the Strouhal number

Side ratio *B/D*	0.50	0.62	0.75	1.0	1.18
Vertical distance of I-type probe *h*	0.6*D*	0.7*D*	0.5*D*	0.5*D*	0.4*D*
Horizontal distance of I-type probe *x*	2.6*B*	3.0*B*	2.0*B*	1.5*B*	1.9*B*

3.1.2 Flow Visualization Tests

(1) Wind tunnel

Flow visualization around a forced-oscillating model was conducted in a small-sized wind tunnel (0.4m high×0.4m width) at Kyushu Institute of Technology with a turbulence intensity of less than 0.5%. The wind velocity V in the flow visualization tests was set as 0.6m/s which was good for visualization. **Figure 3.1.7** shows the flow field in the small-sized wind tunnel.

The Reynolds number in the flow visualization tests was $Re=VD/\nu=1.6\times10^3$, which is smaller than that in the spring-supported tests by approximately one order of magnitude. Nevertheless, regarding a rectangular cross section, the separation point is fixed, and does not depend on the Reynolds number. Thus, it is deemed that the influence caused by different Reynolds numbers on the separated vortex from leading edge and the secondary vortex at trailing edge is small for rectangular cross sections.

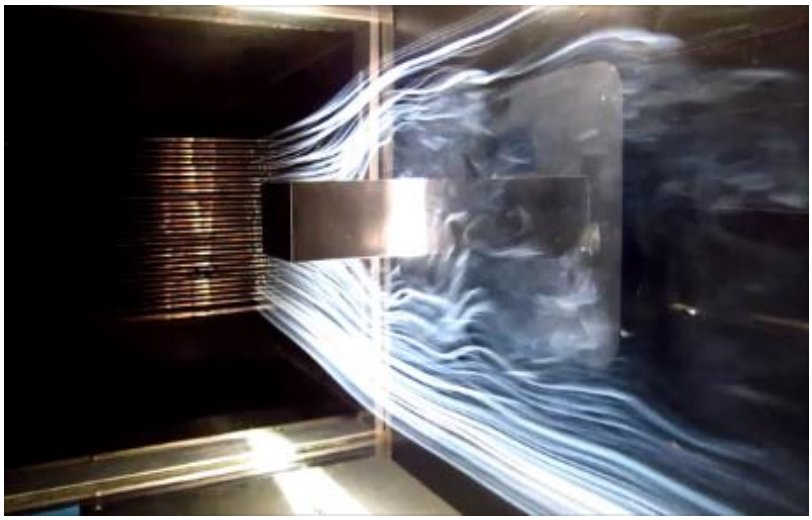

Figure 3.1.7 Flow field inside the small-sized wind tunnel

In addition, according to the results of the measurements of the Strouhal numbers *St* in various Reynolds number range for rectangular cross section with side ratio of *B/D*=1.0, the Strouhal numbers in the Reynolds number range of $Re=1.6\times10^3$ and $Re=1.8\times10^3$-4.0×10^4 are *St*=0.13 and *St*=0.14, respectively[3]. Hence, it can be considered that the influence of the difference in Reynolds number on the flow field is small. Therefore, it is reasonable to have qualitative discussion based on the results of spring-supported and flow visualization tests.

(2) Specifications of target models

The models used in flow visualization tests were made of transparent acrylic panels. All the models were painted in black while the central part of the models which were illuminated by a light source was transparent, for the sake of making the flow patterns around the model as bright as possible. An end plate was attached at the end of each model for the sake of ensuring that the flow around the model was two-dimensional. **Figure 3.1.8** shows the schematic illustration of the model used in flow visualization tests. **Table 3.1.5** shows the size of the models.

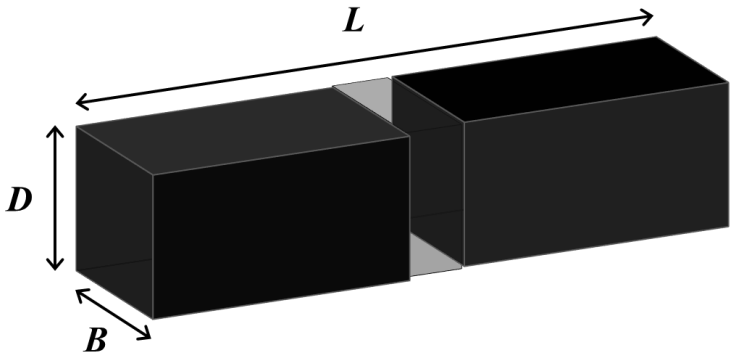

Figure 3.1.8 Schematic illustration of the model used in flow visualization tests

Table 3.1.5 The size of the target models used in flow visualization tests

Side ratio *B/D*	1.18	1.0	0.75	0.62	0.5
Along-wind length *B*(mm)	47.2	40	30	24.8	20
Cross-wind length *D*(mm)	40				
Model length *L*(mm)	150				
Aspect ratio *L/D*	3.8				

(3) Measurement system

Flow visualization around a forced-oscillating model were conducted by the smoke wire method. **Figure. 3.1.9** and **Figure. 3.1.10** show the schematic illustration of the forced oscillation system and the experimental setup for flow visualization tests, respectively. The forced-oscillating amplitude was provided by a vibration generator. The forced frequency and amplitude were adjusted by the digital function signal generator and the amplifier, respectively. Metal wires coated with liquid paraffin and metal powders were placed at a position upstream of the model. Further, the metal wires at the upstream of the model were tightened by additional weight in order to make the metal wires as tight as possible, so that the wires could avoid vibration induced by wind. These wires were heated by an electric current, then the white smoke was shed into the flow. A short time later, when the flow patterns formed by the white smoke became stable and bright enough, the flow patterns around the model were photographed with a high-speed camera. Thus, the flow patterns around the model could be visualized. It should be noted that the white smoke was distributed only on

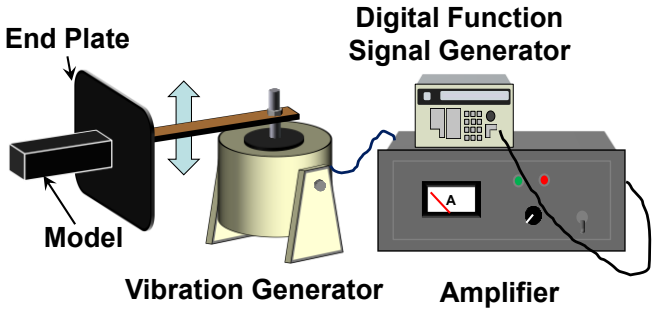

Figure 3.1.9 Schematic illustration of the forced oscillation system for flow visualization tests

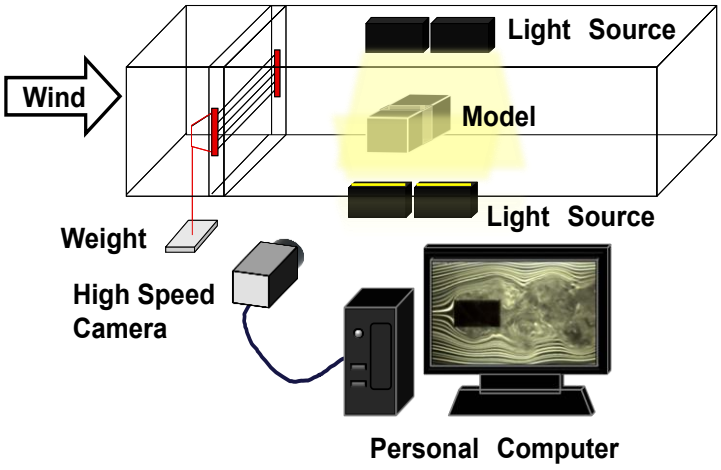

Figure 3.1.10 Schematic illustration of the experimental setup for flow visualization tests

the upper and lower sides of the centerline of the model, in order to ensure that the white smoke around the model was a two-dimensional flow. The photographed pictures were processed with the Motion Studio X64 software in a computer.

(4) Experimental conditions of flow visualization tests

Table 3.1.6 shows the experimental conditions of flow visualization tests. Based on the results obtained from the spring-supported test, at the onset wind velocity of the motion-induced vortex vibration for each cross section, the forced-oscillating amplitude was set as $2\eta/D$=0.02-0.15 (every 0.01 intervals) for the sake of verifying the relation between the secondary vortex at trailing edge and the generation of the motion-induced vortex vibration. The models were photographed for ten periods of vibration at their onset reduced wind velocity of the motion-induced vortex vibration in each forced-oscillating amplitude.

Table 3.1.6 Experimental conditions for flow visualization tests

B/D	*B* (mm)	*D* (mm)	Wind velocity *V* (m/s)	Forced-oscillating frequency *f* (Hz)	Reduced wind velocity $V_r=V/fD$	Non-dimensional forced-oscillating amplitude $2\eta/D$
0.50	20	40	0.6	18.0	0.84	0.04-0.10
0.62	24.8	40	0.6	14.5	1.0	0.04-0.11
0.75	30	40	0.6	12.0	1.3	0.04-0.14
1.0	40	40	0.6	9.0	1.7	0.02-0.15
1.18	47.2	40	0.6	7.6	2.0	0.02-0.15

Model length: 150mm

3.2 Validity of the Experimental Method

It should be pointed out that the blockage ratio in the spring-supported tests is 10%, which is larger than the conventional requirement of the blockage ratio 5% in the wind tunnel test. Therefore, it is necessary to confirm the validity of the spring-supported tests. **Figure 3.2.1** shows the comparison of the *V-A* diagrams of a rectangular cross section with a side ratio of *B/D*=1.18 in the present and previous studies[4]. By comparing the result with a blockage ratio of 10% in this study with the previous result whose blockage ratio is 5%, it is confirmed that the onset wind velocity and maximum response amplitude of the vortex-induced vibration in the present and previous studies have approximately the same value. Thus, it can be considered that

the experimental method of spring-supported tests in this study is validated and appropriated.

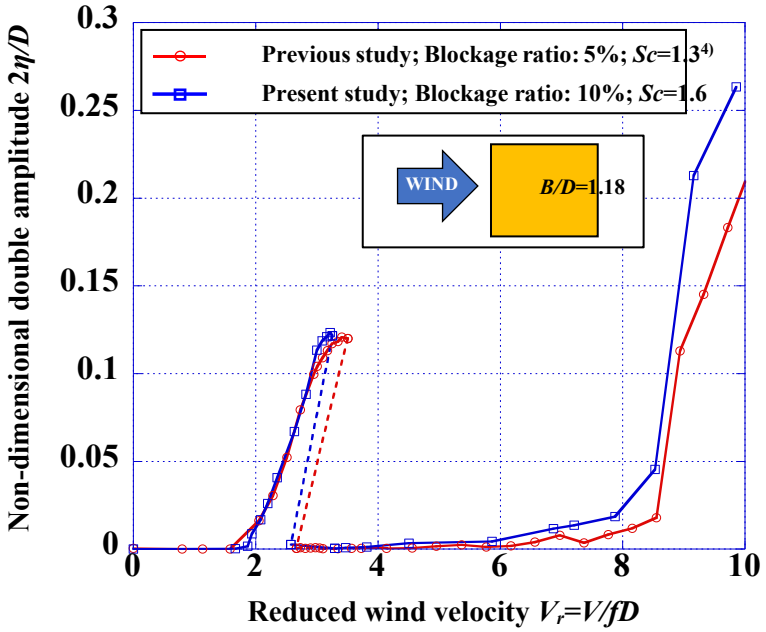

Figure 3.2.1. Comparison of the results of present and previous studies[4)]

3.3 Response Characteristics of Rectangular Cylinders of *B/D*＝0.50-1.18 in the Heaving Mode

The results of spring-supported tests for rectangular cylinders with side ratios of *B/D*=0.50-1.18 are shown in **Figure 3.3.1-Figure 3.3.5**. The motion-induced vortex vibration was confirmed at around V_{cr}=1.67*B/D* in the cases of *B/D*=0.75, 1.0, 1.18. It is noted that the motion-induced vortex vibration was also confirmed for the case of *B/D*=0.62 when the Scruton number was set as 0.8, as shown in **Figure 3.3.6**. With regard to the cross section of *B/D*=0.50, the motion-induced vortex vibration was not confirmed, even if the Scruton number was set as 1.2. By comparing these *V-A* diagrams, it was clear that as the side ratio *B/D* becomes larger, the maximum response amplitude of the motion-induced vortex vibration tends to increase.

Table 3.3.1 shows the results of flow visualization tests for the side ratios of *B/D*=0.50-1.18 at the onset wind velocity of the motion-induced vortex vibration in the same forced-oscillating amplitude of *2η/D*=0.10. Focusing on the flow patterns of the separated vortex from leading edge, it was found that in the cross sections with

side ratios of *B/D*=0.50, 0.62, the separated vortex from leading edge gradually separated from the upper and lower surfaces of the model and flowed down, instead of moving along the upper and lower surfaces of the model. Thus, the fluctuating lift provided by the separated vortex from leading edge did not seem to fully act on the upper and lower surfaces of the model. As the side ratio *B/D* became larger, the separated vortex from leading edge tended to come closer to the model and move along the surface. Therefore, the fluctuating lift of the motion-induced vortex vibration was considered to increase as the side ratio *B/D* became larger.

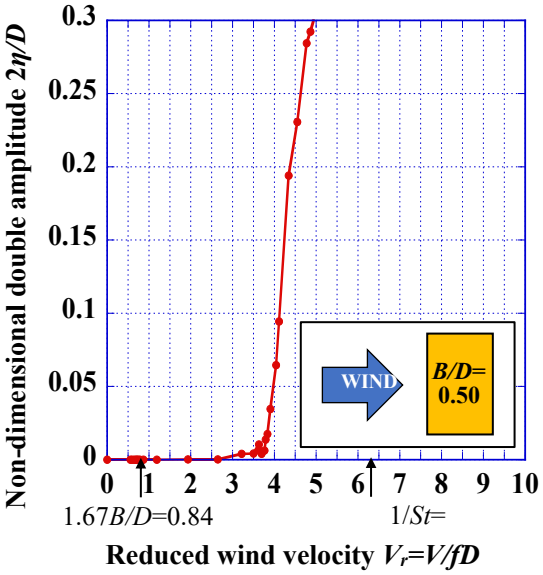

Figure 3.3.1 *V-A* diagram of *B/D*=0.50, *Sc*=1.6

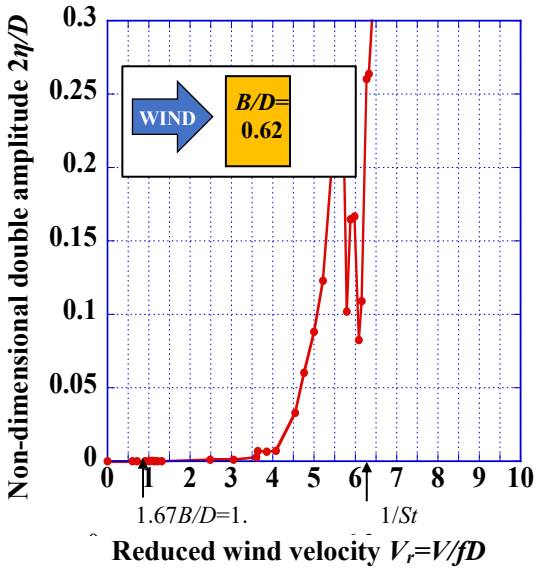

Figure 3.3.2 *V-A* diagram of *B/D*=0.62, *Sc*=1.6

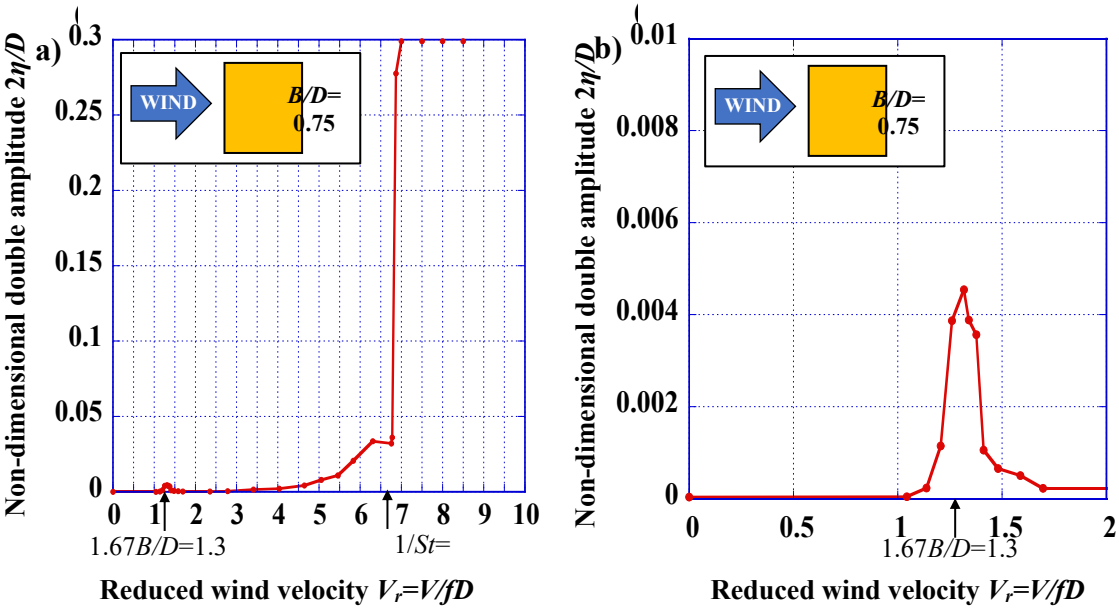

Figure 3.3.3 (a) *V-A* diagram of *B/D*=0.75 and (b) enlarge view of wind velocity region of motion-induced vibration, *Sc*=1.6

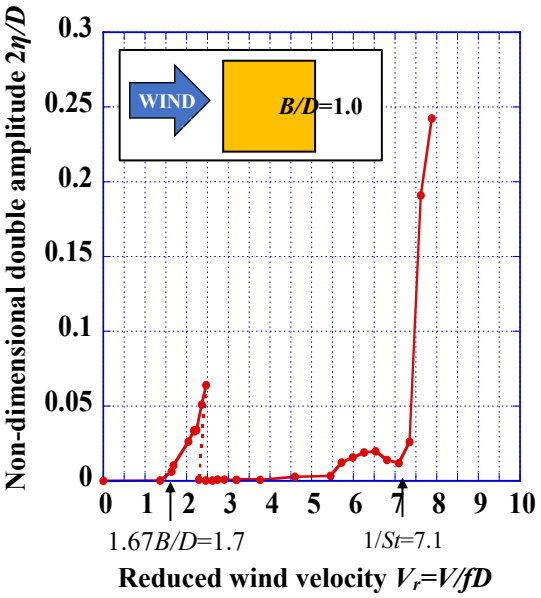

Figure 3.3.4 *V-A* diagram of *B/D*=1.0, *Sc*=1.6

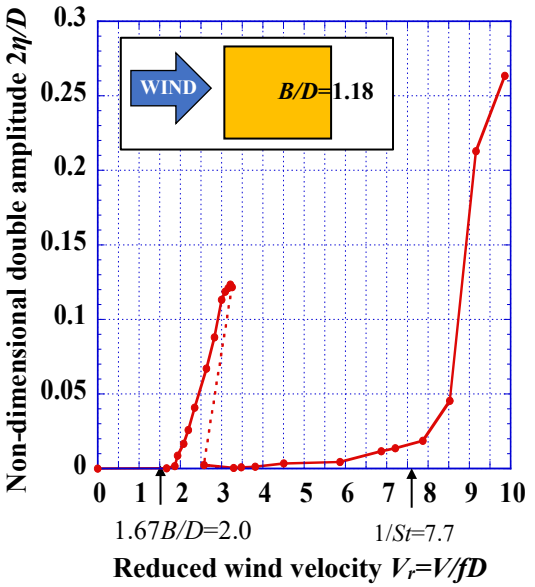

Figure 3.3.5 *V-A* diagram of *B/D*=1.18, *Sc*=1.6

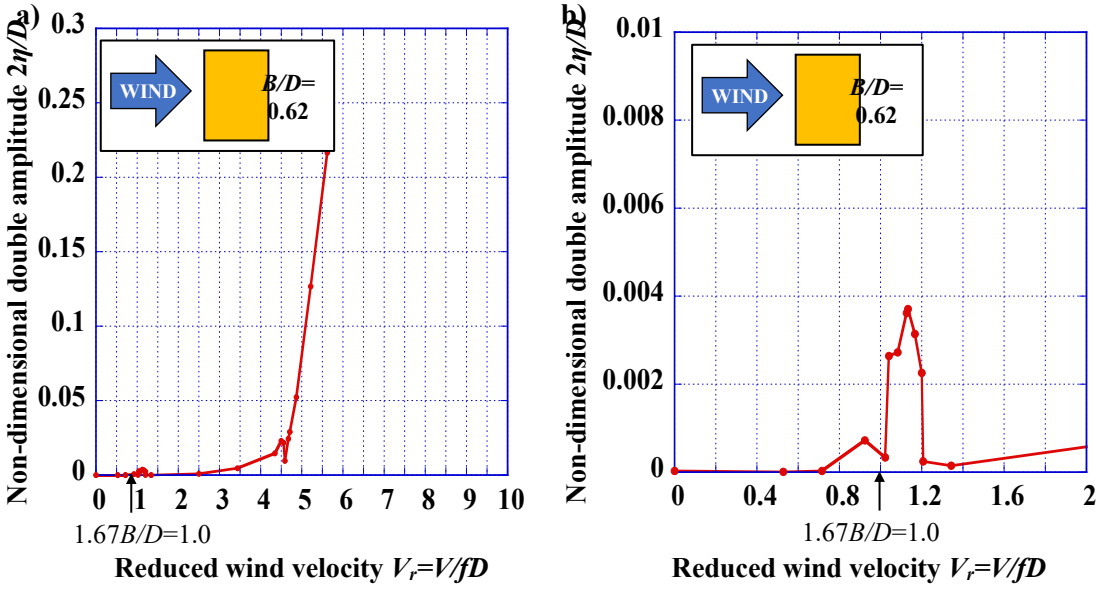

Figure 3.3.6 (a) *V-A* diagram of *B/D*=0.62 and (b) enlarge view of wind velocity region of motion-induced vibration, *Sc*=0.8

The inverse of Strouhal numbers 1/*St* was indicated in the *V-A* diagrams for each cross section. The Kármán vortex-induced vibration was confirmed in the cross sections of *B/D*=0.75, 1.0, 1.18 in the vicinity of the inverse of the Strouhal number 1/*St*. However, there was an obvious discrepancy between the estimated onset wind velocity of the Kármán vortex-induced vibration 1/*St* and the experimental one for the cross sections of *B/D*=0.50, 0.62. The aerodynamic vibrations were confirmed occurring at the vicinity of V_r=4, instead of the inverse of Strouhal numbers 1/*St*. These

Table 3.3.1 Results of flow visualization test of B/D=0.50-1.18 ($2\eta/D$=0.10 for all cases)

B/D	$V_r=V/fD$	Results of flow visualization test at middle displacement with maximum **upward** velocity	Results of flow visualization test at middle displacement with maximum **downward** velocity
0.5	0.84 =1.67B/D	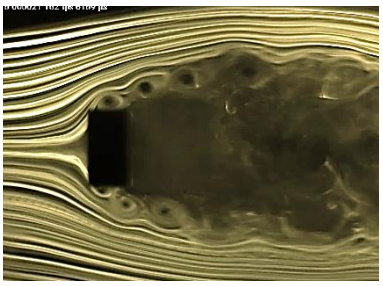	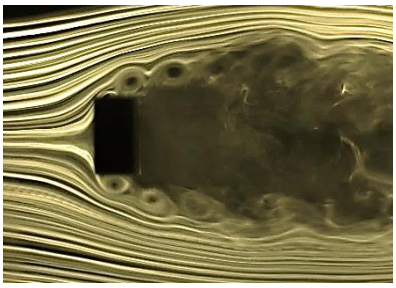
0.62	1.0 =1.67B/D	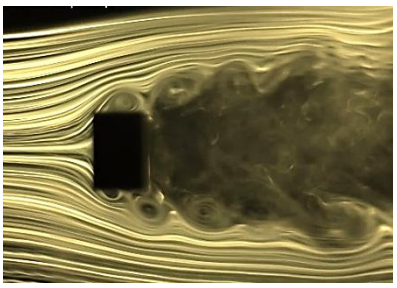	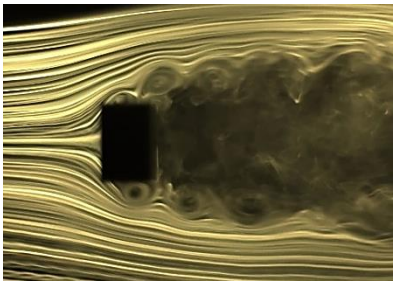
0.75	1.3 =1.67B/D	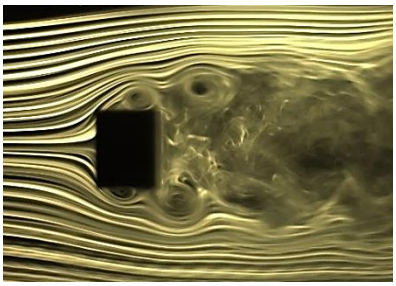	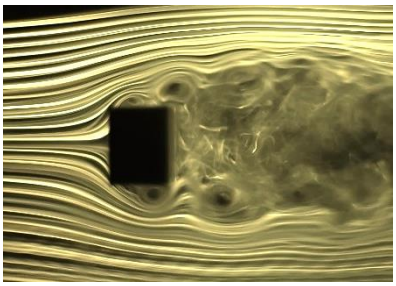
1.0	1.7 =1.67B/D	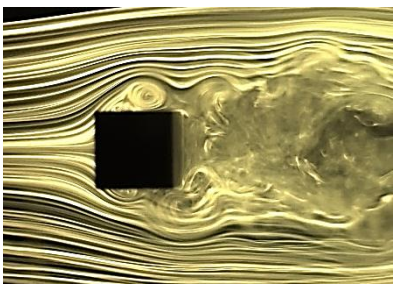	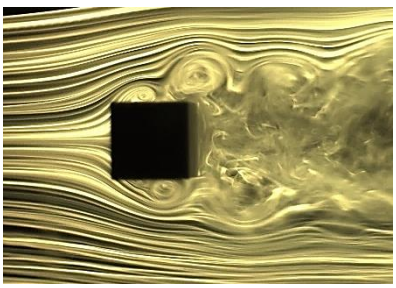
1.18	2.0 =1.67B/D	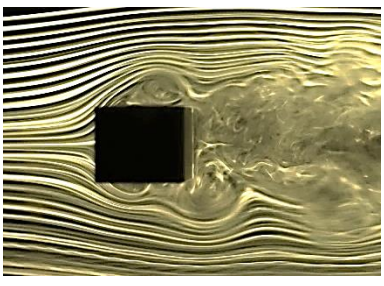	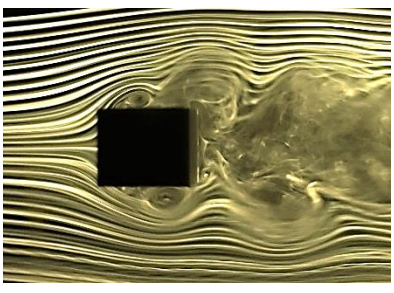

aerodynamic vibrations are considered to be the low-speed galloping, according to the results obtained from previous wind tunnel tests[5]. The low-speed galloping is associated with the occurrence of negative fluid dynamic damping, which may arise over a range of low wind velocity below the Kármán vortex resonance velocity. Nevertheless, the low-speed galloping was not confirmed occurring on a rectangular cross section with a side ratio of B/D=0.60[6]. Further investigation therefore needs to be conducted.

One of the features of the low-speed galloping is that the growth of the response amplitude is slower than the vortex-induced vibration[5]. Thus, the measurements of time history waveforms based on the responses in the wind velocity region of the low-speed galloping and Kármán vortex-induced vibration for the cross sections of B/D=0.50, 0.62 were carried out. The results are shown in **Figure 3.3.7** and **Figure 3.3.8**, respectively. In the cross section of B/D=0.50, the response amplitude developed more rapidly as the wind velocity increased (from No.1 to No.4). Therefore, it is suggested that the response characteristics gradually change from the low-speed galloping to the Kármán vortex-induced vibration along with the increase of the wind velocity. On the other hand, in the cross section of B/D=0.62, it was also confirmed that the growth of the response amplitude at the wind velocity of V_r=5.2 (No. 1) is slower than that at the wind velocity of V_r=6.4 (No. 4). However, at the wind velocities

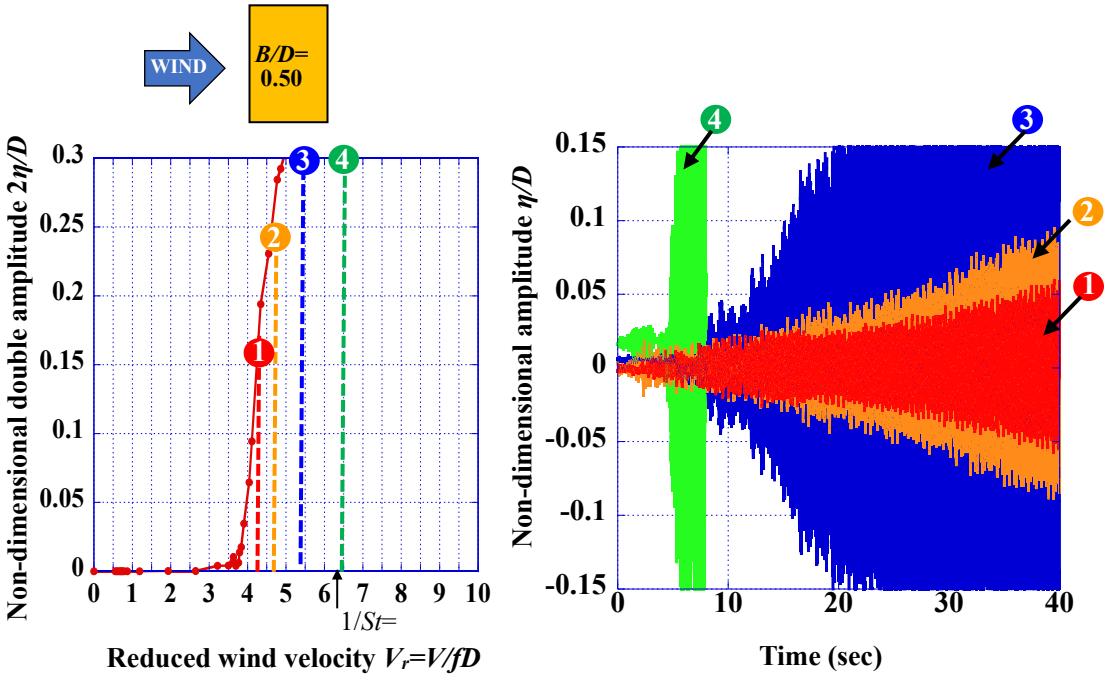

Figure 3.3.7 Time history response for B/D=0.50 (V_r=4.4, 4.7, 5.3, 6.4)

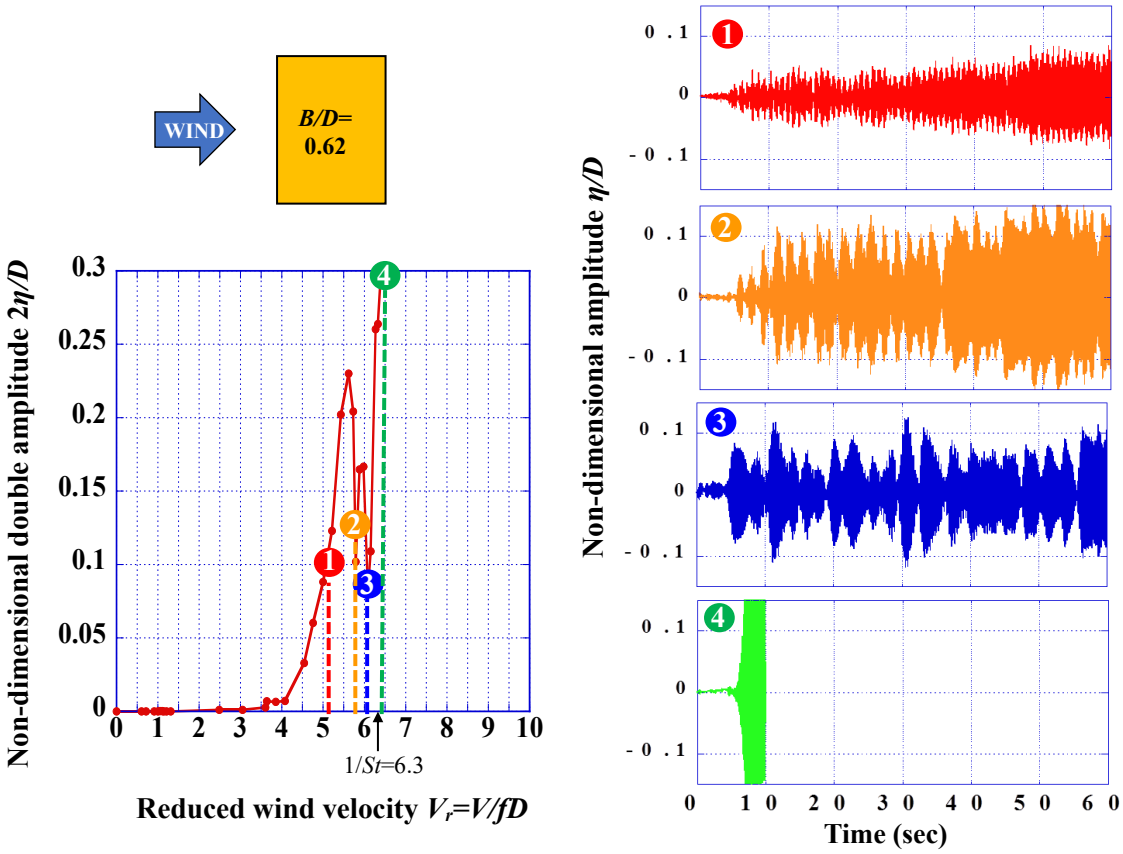

Figure 3.3.8 Time history response for *B/D*=0.62 (V_r=5.2, 5.9, 6.1, 6.4)

of V_r=5.9, 6.1 (No. 2, No. 3) which are the intermediate wind velocity region of the low-speed galloping and the Kármán vortex-induced vibration, turbulent response waveforms were confirmed. This wind velocity region is considered to be the transition region from the low-speed galloping to the Kármán vortex-induced vibration. Thus, this wind velocity region is an unstable area where both the response characteristics of the low-speed galloping and the Kármán vortex-induced vibration are mixed.

3.4 Necessity of Secondary Vortex at Trailing Edge for the Onset of Motion-induced Vortex Vibration for Rectangular Cylinders of *B/D*＝0.62-1.18 in the Heaving Mode

In one period of vibration, there will be up to two secondary vortices at trailing edge generated at the rear corner of the model. Therefore, when the model is forced-oscillated for ten periods, there will be up to twenty secondary vortices at trailing edge generated. Thus, the generation probability of the secondary vortex at trailing edge is

defined as (the number of generation times in ten periods/20) ×100 (%), and it was used as an index showing the extent of stability of the secondary vortex at trailing edge. **Figure 3.4.1(a)-Figure 3.4.4 (a)** show the relation between the generation probability of secondary vortex at trailing edge calculated in ten periods of vibration and the forced-oscillating amplitude at the wind velocity where the motion-induced vortex vibration has generated, regarding the cross sections with side ratios of *B/D*=0.62-1.18. **Figure 3.4.1(b)-Figure 3.4.4 (b)** show the photographs of flow visualization tests in a higher and a lower forced-oscillating amplitude, respectively. A red dotted rectangle was added at the rear corner in the bottom surface in order to recognize whether or not the secondary vortex at trailing edge is generated. **Figure 3.4.1(c)-Figure 3.4.4 (c)** show the *V-A* diagrams in the wind velocity region of the motion-induced vortex vibration. It is noted that in the case of *B/D*=0.62, due to the high forced-oscillating frequency, flow visualization tests were not conducted successfully in higher forced-oscillating amplitudes where the generation probability of the secondary vortex at trailing edge can reach 100%. Nevertheless, it does not have influence on the discussion of the experimental results, because the main attention in this study is focused in the low forced-oscillating amplitude range.

The separated vortex from leading edge was observed in all the cross sections, regardless of the forced-oscillating amplitude. On the other hand, it was confirmed that the generation probability of secondary vortex at the trailing edge can reach 100% only in extremely high forced-oscillating amplitude, which is much higher than the response amplitude of motion-induced vortex vibration. For instance, in the case of *B/D*=0.75

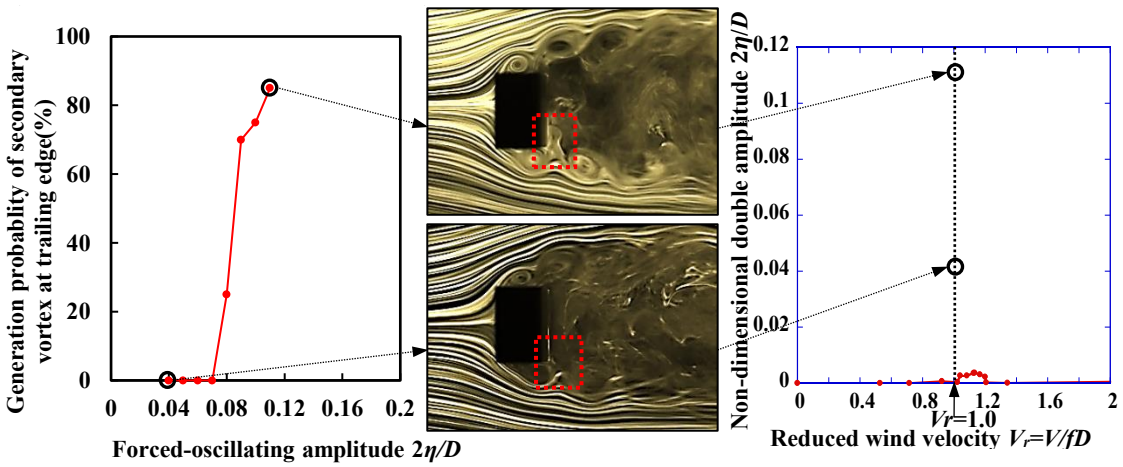

Figure 3.4.1 (a) Generation probability for secondary vortex at the trailing edge of *B/D*=0.62 at V_r=1.0, (b) flow visualization result of *B/D*=0.62 at bottom displacement at V_r=1.0 and (c) *V-A* diagram of *B/D*=0.62 (*Sc*=0.8)

shown in **Figure 3.4.2**, the generation probability of the secondary vortex at trailing edge reached 100% in the amplitude of $2\eta/D$=0.12 at the reduced wind velocity of V_r=1.3. However, the secondary vortex at trailing edge was not observed in amplitudes smaller than $2\eta/D$=0.07. A similar tendency was confirmed in all other cross sections, as shown in **Figure 3.4.1, Figure 3.4.3** and **Figure 3.4.4**. At the wind velocity where motion-induced vortex vibration has been generated, in the lower forced-oscillating amplitude range, the generation probability of the secondary vortex at trailing edge was zero. These results indicate that the motion-induced vortex vibration can occur without the shedding of the secondary vortex at trailing edge. Therefore, it is suggested that the shedding of secondary vortex at trailing edge is not a necessary condition for the generation of the motion-induced vortex vibration.

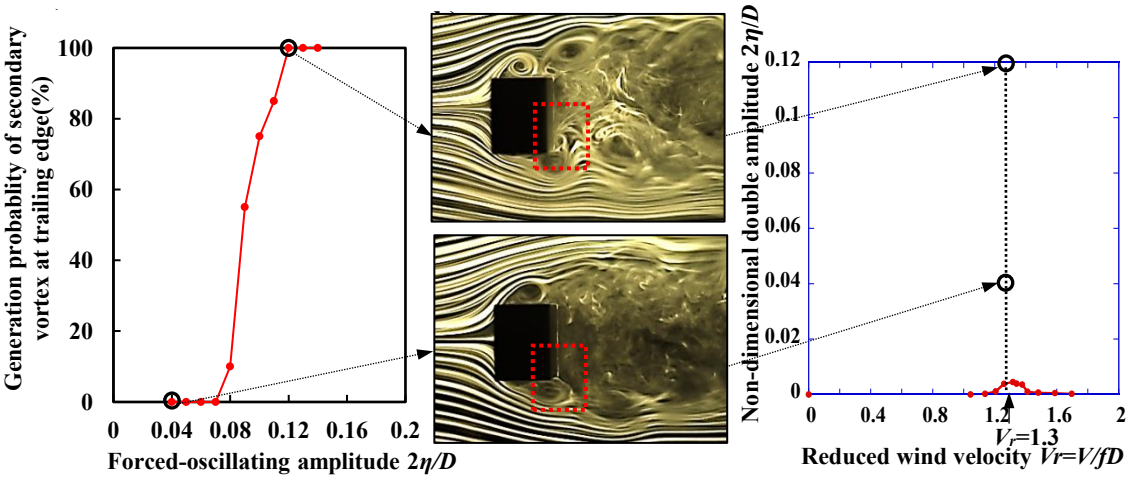

Figure 3.4.2 (a) Generation probability for secondary vortex at the trailing edge of *B/D*=0.75 at V_r=1.2, (b) flow visualization result of *B/D*=0.75 at bottom displacement at V_r=1.2 and (c) *V-A* diagram of *B/D*=0.75 (*Sc*=1.6)

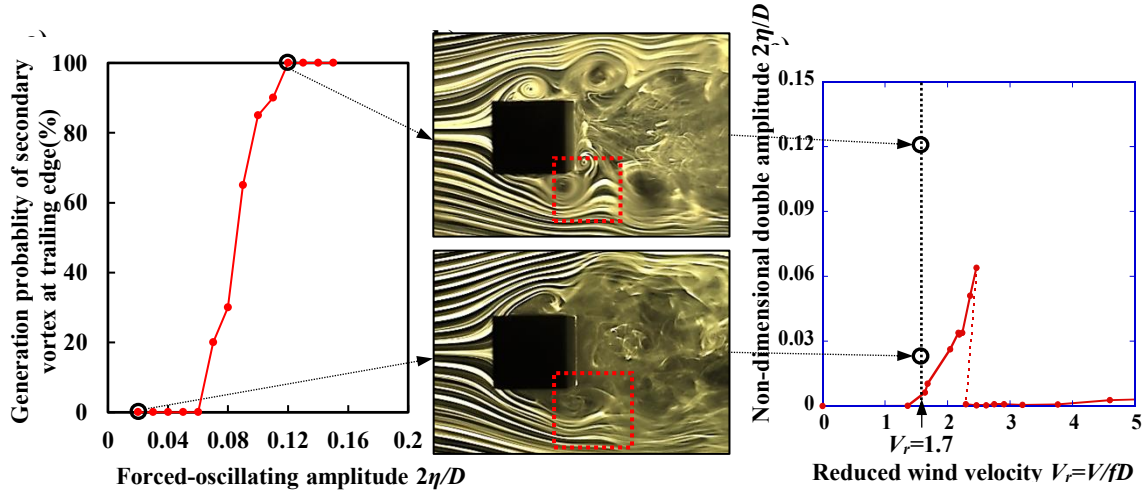

Figure 3.4.3 (a) Generation probability for secondary vortex at the trailing edge of *B/D*=1.0 at V_r=1.7, (b) flow visualization result of *B/D*=1.0 at bottom displacement at V_r=1.7 and (c) *V-A* diagram of *B/D*=1.0 (*Sc*=1.6)

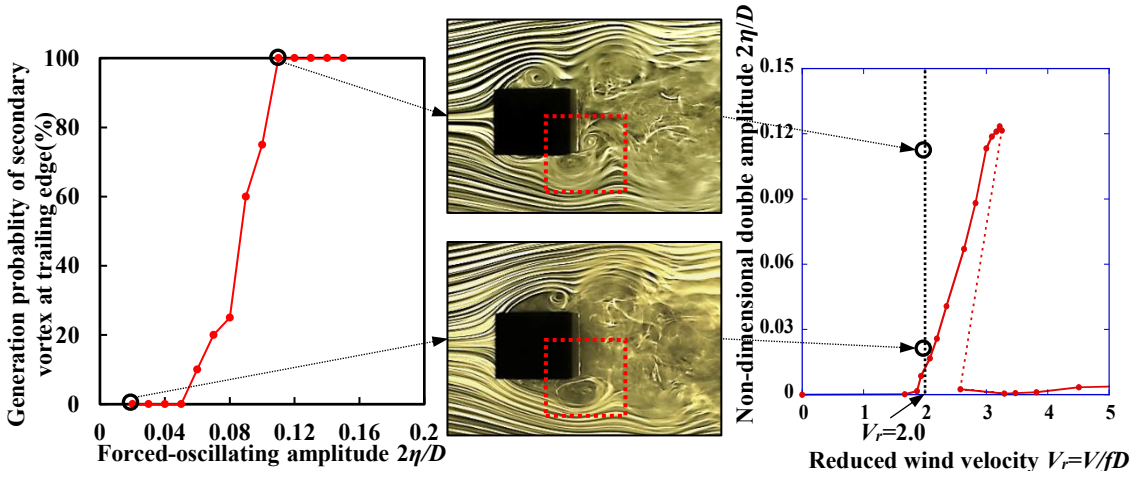

Figure 3.4.4 (a) Generation probability for secondary vortex at the trailing edge of *B/D*=1.18 at V_r=2.0, (b) flow visualization result of *B/D*=1.18 at bottom displacement at V_r=2.0 and (c) *V-A* diagram of *B/D*=1.18 (*Sc*=1.6)

3.5 Summary

In this chapter, spring-supported and flow visualization tests in the heaving mode for rectangular cross sections with side ratios of *B/D*=0.50, 0.62, 0.75, 1.0, 1.18 are explained. Subsequently, the response characteristic of rectangular cross sections with small side ratios are obtained. Finally, the necessity of the secondary vortex at trailing edge for the motion-induced vortex vibration for rectangular cross sections with small side ratios are investigated. As a consequence, following conclusions have been drawn:

1. The motion-induced vortex vibration can be generated even on the rectangular cross sections with side ratios of *B/D*=0.62, 0.75, 1.0, 1.18, notwithstanding the motion-induced vortex vibration is considered to occur on the rectangular cross sections with side ratio of *B/D*=2.0-8.0, according to the previous wind tunnel tests[1]. As the side ratio *B/D* becomes larger, the maximum response amplitude for the side ratios of *B/D*=0.62-1.18 tends to increase. Because the separated vortex from leading edge separates away from the models, instead of moving along the upper and lower surfaces of the models for the cross section with small side ratios. Thus, it is considered that the fluctuating lift provided by separated vortex from leading edge does not seem to fully act on the models for smaller side ratios.

2. Regarding the rectangular cross sections with side ratios of *B/D*=0.50, 0.62, the low-speed galloping was confirmed in the wind velocity region lower than the estimated onset wind velocity of the Kármán vortex-induced vibration. Furthermore, the response characteristics gradually change from the low-speed

galloping to the Kármán vortex-induced vibration along with the increase of the wind velocity.

3. Based on the results obtained from flow visualization tests, it is clear that the motion-induced vortex vibration can be generated without the shedding of the secondary vortex at trailing edge. Therefore, it is suggested that the secondary vortex at trailing edge is not a necessary condition for the generation of motion-induced vortex vibration regarding the rectangular cross sections with side ratios of B/D=0.62, 0.75, 1.0, 1.18.

References

1) Shiraishi, N. and Matsumoto, M., 1983. On classification of vortex-induced oscillation and its application for bridge structures, Journal of Wind Engineering and Industrial Aerodynamics, 14 (1-3), 419-430.
2) Tamai, Y., Matsuda, K., Kato, K., Misawa, K. and Ikeda, I., 2014. Experimental study on aerodynamic vibration of a bracing member with a rectangular cross section of the long-spanned truss bridge, Proceedings of the 23rd National Symposium on Wind Engineering, 211-216. (in Japanese)
3) Okajima, A., 1990. Numerical simulation of flow around rectangular cylinders, Journal of Wind Engineering and Industrial Aerodynamics, 33, 171-180,
4) Matsuda, K., Kato, K., Hisatomi, K. and Suda, K., 2013. Low speed instability of two-dimensional rectangular prims, Proceeding of the ASME 2013 Pressure Vessels and Piping Conference (PVP2013), 97353, Paris, France.
5) Hirata, K., 1993. Study on Galloping generation mechanism, Doctor's thesis, Kyushu University. (in Japanese)
6) Nakamura, Y. and Matsukawa, T., 1987. Vortex excitation of rectangular cylinders with a long side normal to the flow, Journal of Fluid Mechanics, 180, 171-191.

Chapter 4: The Role of Secondary Vortex at Trailing Edge in Motion-induced Vortex Vibration for Rectangular Cylinders of *B/D* =2, 4, 6 in a Heaving Mode

The necessity of the secondary vortex at trailing edge for the motion-induced vortex vibration with respect to the rectangular cross sections with side ratios of *B/D*=0.62-1.18 has been discussed in chapter 3. Nevertheless, it is deemed that the motion-induced vortex vibration is confirmed occurring on the rectangular cross sections with side ratios of *B/D*=2.0-8.0, according to the summary of the results of previous wind tunnel tests[1]. The considerations based on the results which were obtained from the rectangular cross sections with side ratios smaller than *B/D*=2.0 may have their particularities in terms of the side ratio. Hence, with regard to the rectangular cross sections with side ratios of *B/D*=2.0-8.0, it is necessary to investigate the effect of the secondary vortex at trailing edge on the motion-induced vortex. This chapter therefore focuses on the rectangular cross sections with side ratios of *B/D*=2.0-8.0. Spring-supported and flow visualization tests for rectangular cross sections with side ratios of *B/D*=2.0, 4.0, 6.0 were carried out, in order to clarify the role of the secondary vortex at trailing edge in the motion-induced vortex vibration for the rectangular cross sections with side ratios of *B/D*=2.0-8.0.

4.1 Wind Tunnel Tests for Rectangular Cylinders of *B/D*=2, 4, 6 in a Heaving Mode

4.1.1 Spring-supported Tests

(1) Wind tunnel

In order to obtain the response characteristics of the target rectangular cross sections, the spring-supported tests in the heaving mode were conducted in a closed circuit wind tunnel at Kyushu Institute of Technology. This closed circuit wind tunnel is the same as the one which has been demonstrated in chapter 3. The spring-supported tests were carried out in a smooth flow with a turbulence of less than 0.5%. The wind velocity V in the spring-supported tests was from 1.5m/s to 12m/s. The Reynolds

number in the wind velocity region of the motion-induced vortex vibration was $Re=VD/\nu=9.8\times10^3$-3.4×10^4, where V: wind velocity (m/s), D: cross-wind length (m), ν: kinematic viscosity (m^2/s).

(2) Specifications of target models and splitter plate

Rectangular cross sections with side ratios of B/D=2.0, 4.0, 6.0 were selected as the target cross sections. The model of B/D=2.0 was constructed of cypress wood attached with two end plates at both ends of the model, in order to make the flow around the models appear as a two-dimensional flow. The models of B/D=4.0, 6.0 were the composed of the model of B/D=2.0 and cubic polystyrene foams whose purpose was to alter the side ratios of the models. **Figure 4.1.1** shows the model of B/D=2.0 used in spring-supported tests. **Table 4.1.1** shows the size of the target models.

Figure 4.1.1 Sectional model of *B/D*=2.0 in the wind tunnel

Table 4.1.1 The size of the target models used in spring-supported tests

Side ratio B/D	2.0	4.0	6.0
Along-wind length B(mm)	180	360	540
Cross-wind length D(mm)	90		
Model length L(mm)	828		
Aspect ratio L/D	9.2		

According to the results of previous wind tunnel tests, the reduced frequencies of the Kármán vortex *St* and the separated vortex from leading edge 0.6*D/B* are close to each other on the cross sections with side ratios of *B/D*=2.8-6.0[2]. Thus, in the wind velocity region where the motion-induced vortex vibration occurs, the separated vortex from leading edge and the secondary vortex at trailing edge are strongly influenced by the Kármán vortex synchronizing with the vibration of the model, regarding the rectangular cross sections with side ratios of *B/D*=4.0, 6.0. However, the main research objective in this study is the effect of the secondary vortex at trailing edge on the motion-induced vortex vibration. Therefore, a splitter plate (hereinafter referred as S.P.) was installed at the downstream of the model with the gap length *g* for the sake of eliminating the influence of the Kármán vortex for the cross section.

In general, although the S.P. is usually used as a tool for suppressing the Kármán vortex, it does not have direct relation with the secondary vortex at trailing edge. However, based on the fact that different gap lengths have different effects on response characteristics of the motion-induced vortex vibration[2), 3)], it is deemed that the interaction among the Kármán vortex, the separated vortex from leading edge and the secondary vortex at trailing edge is different due to the difference in the gap length. Thus, two different gap lengths were provided to each cross section for confirming the interaction among these vortices. On the other hand, it is indicated that the Kármán vortex has an effect which can reduce the separated vortex from leading edge[3)]. Regarding the cross section of *B/D*=2.0, the values of the reduced frequency of the separated vortex from leading edge and the Strouhal number *St* separate with each other[2)]. Therefore, it can be considered that the influence of the Kármán vortex on the motion-induced vortex vibration for *B/D*=2.0 is remarkably different from that for *B/D*=4.0, 6.0. In order to compare the influence of the Kármán vortex on the motion-induced vortex vibration in various side ratios, the S.P. was also used for the cross section of *B/D*=2.0.

Figure 4.1.2 and **Figure 4.1.3** show the schematic illustration and setting situation of the S.P., respectively. In order to ensure that the Kármán vortex can be eliminated effectively, the along-wind lengths of the S.P. were set as 20*D* [1800mm (*D*=90mm)], which is considered to be long enough, by referring to the result of previous wind tunnel test[3)]. The width and thickness of the S.P. were 900mm and 13mm, respectively.

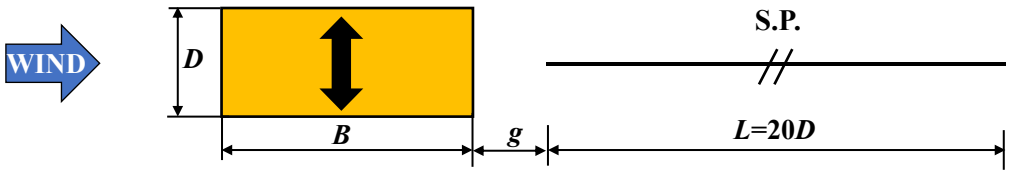

Figure 4.1.2 Schematic illustration of the S.P. and model

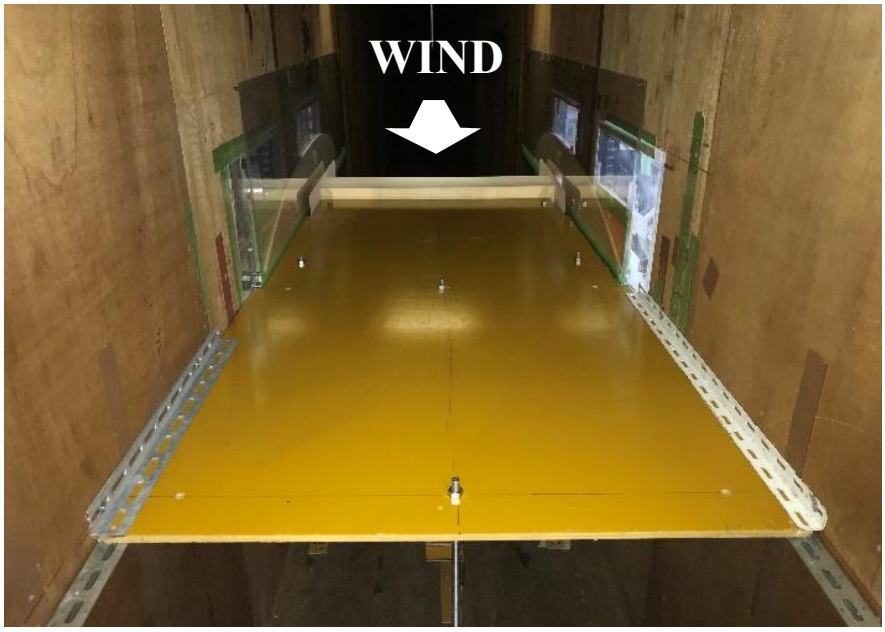

Figure 4.1.3 Setting situation of the S.P. in the wind tunnel

(3) Measurement system

The measurement and suspension systems are the same as the ones which have been demonstrated in chapter 3. The angle of attack was set as 0° for all the experiments. The models were supported in the wind tunnel elastically in the heaving mode by two coil springs at each side. The response amplitude of the models during vibration was measured by a laser displacement detector. **Figure 4.1.4** shows the suspension situation outside the wind tunnel. The vibration system was so well designed that the structural damping of the vibration system could be reduced to as a small value as possible. The structural damping of the vibration system was adjusted with a pair of magnetic dampers.

Figure 4.1.4 Suspension situation outside the wind tunnel

(4) Experimental conditions of spring-supported tests

Table 4.1.2 shows the experimental conditions for the spring-supported tests. The Scruton number *Sc* for each cross section was adjusted as a close value as possible. The gap length *g* between the model and S.P. was adjusted within a range of g=0.10B-0.33B.

Table 4.1.2 Experimental conditions for spring-supported tests

B/D	*B* (mm)	*D* (mm)	S.P.	Gap length *g*	Natural frequency *f* (Hz)	Air density ρ (kg/m^3)	Mass per unite length *m* (kg/m)	Logarithmic decrement of structural damping δ	$Sc=2m\delta/\rho D^2$
2	180	90	w/o	-	5.22	1.23	5.49	0.0043	4.7
			w	0.10*B*	5.15	1.24	5.36	0.0044	4.7
			w	0.25*B*	5.20	1.24	5.52	0.0048	5.2
4	360	90	w/o	-	6.25	1.25	3.82	0.0133	10.1
			w	0.10*B*	6.20	1.24	3.69	0.0135	9.9
			w	0.31*B*	6.23	1.23	3.85	0.0130	10.1
6	540	90	w/o	-	5.73	1.22	4.55	0.01561	14.4
			w	0.10*B*	5.66	1.23	4.44	0.02465	21.9
			w	0.33*B*	5.67	1.22	4.41	0.01619	14.4

Model length: 828mm

4.1.2 Flow Visualization Tests

(1) Wind tunnel

Flow visualization around a forced-oscillating model was conducted in a small-sized wind tunnel at Kyushu Institute of Technology. The small-sized wind tunnel is the same as the one demonstrated in chapter 3. The wind velocity V in the flow visualization tests was set as 0.8m/s which was good for visualization.

The Reynolds number in the flow visualization tests was $Re=VD/\nu=1.1\times10^3$, which is smaller than that in the spring-supported tests by approximately one order of magnitude. Nevertheless, according to the results of the measurements of the Strouhal numbers St in various Reynolds number range for a rectangular cross section with a side ratio of B/D=2.0, the Strouhal numbers in the Reynolds number range of $Re=1.1\times10^3$ and $Re=1.8\times10^3$-3.4×10^4 are St=0.08 and St=0.07, respectively[4]. A similar tendency is also confirmed for the cross section with a side ratio of B/D=4.0[5]. Hence, it can be considered that the influence of the difference in Reynolds number on the flow field is small. Therefore, it is reasonable to have qualitative discussion based on the results of spring-supported and flow visualization tests.

(2) Specifications of target models and splitter plate

The models used in flow visualization tests were made of transparent acrylic panels. All the models were painted in black while the central part of the models which were illuminated by a light source was transparent, for the sake of making the flow patterns around the model as bright as possible. An end plate was attached at the end of each model for the sake of ensuring that the flow around the model was two-dimensional. **Table 4.1.3** shows the size of the models. **Figure 4.1.5** shows the model of B/D=4.0 used in flow visualization tests inside the wind tunnel.

Table 4.1.3 The size of the target models used in flow visualization tests

Side ratio B/D	2.0	4.0	6.0
Along-wind length B(mm)	40	80	120
Cross-wind length D(mm)	20		
Model length L(mm)	150		
Aspect ratio L/D	7.5		

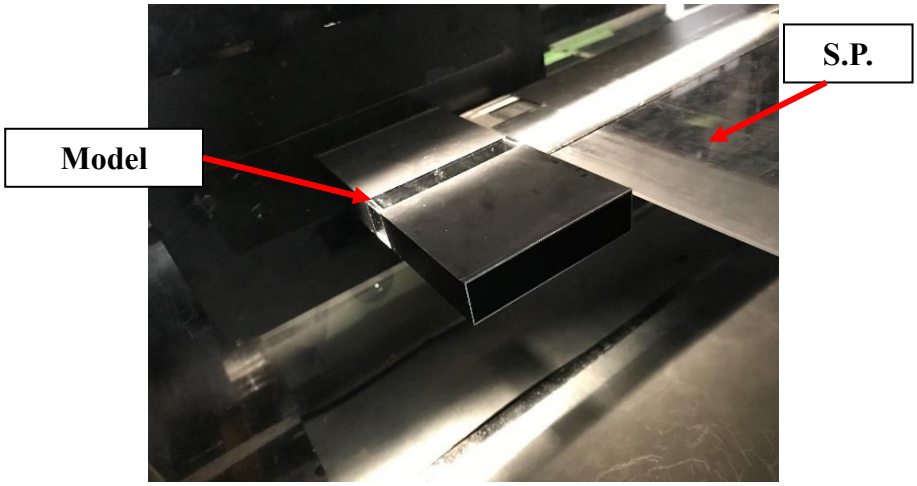

Figure 4.1.5 Setting situation of the model of *B/D*=4.0 inside the wind tunnel

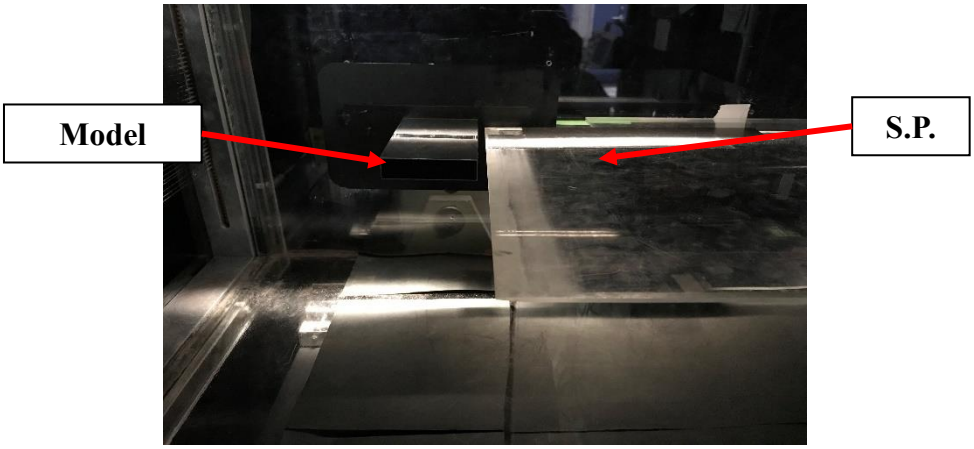

Figure 4.1.6 Setting situation of the S.P. inside the wind tunnel

The S.P. was also used and was set to the same configuration as the spring-supported tests. The along-wind length of the S.P. was 400mm. The width and thickness of the S.P. were 400mm and 3mm, respectively. **Figure 4.1.6** shows the setting situation of the S.P. inside the small-sized wind tunnel.

(3) Measurement system

Flow visualization around a forced-oscillating model were conducted by the smoke wire method. The experimental setup and forced oscillation system are the same as the ones which have been introduced in chapter 3. The forced-oscillating frequency and amplitude were adjusted by a digital function signal generator and an amplifier, respectively. The flow patterns around the model were photographed with a high-speed camera. In each forced-oscillating amplitude, the models were photographed for ten periods of vibration. The photographed pictures were processed with the Motion

Studio X64 software in a computer.

(4) Experimental conditions of flow visualization tests

Table 4.1.4 shows the experimental conditions of flow visualization tests. Based on the results obtained from the spring-supported tests, at the onset wind velocity of the motion-induced vortex vibration for each cross section, the non-dimensional forced-oscillating double amplitude was set as $2\eta/D$=0.02-0.34 (every 0.02 intervals), in order to verify the relation between the secondary vortex at trailing edge and the generation of the motion-induced vortex vibration. On the other hand, at the wind velocity where the maximum response amplitude of the motion-induced vortex vibration occurred, the non-dimensional forced-oscillating double amplitude was set as $2\eta/D$=0.20 in order to observe the effect of the secondary vortex at trailing edge on the response characteristics of the motion-induced vortex vibration at peak response amplitude.

Table 4.1.4 Experimental conditions for flow visualization tests

B/D	*B* (mm)	*D* (mm)	S.P.	Gap length *g*	Wind velocity *V* (m/s)	Forced-oscillating frequency *f* (Hz)	Reduced wind velocity *Vr=V/fD*	Non-dimensional forced-oscillating double amplitude $2\eta/D$
2	40	20	w/o	-	0.8	10.5	3.8	0.02-0.20
			w/o	-	0.8	7.3	5.5	0.20
			w	0.10*B*	0.8	7.3	5.5	0.20
			w	0.25*B*	0.8	7.3	5.5	0.20
4	80	20	w/o	-	0.8	10.5	3.8	0.02-0.20
			w/o	-	0.8	9.3	4.3	0.20
			w	0.10*B*	0.8	9.3	4.3	0.20
			w	0.31*B*	0.8	9.3	4.3	0.20
			w/o	-	0.8	5.6	7.1	0.02-0.34
			w/o	-	0.8	4.8	8.3	0.20
			w	0.10*B*	0.8	4.8	8.3	0.20
			w	0.31*B*	0.8	4.8	8.3	0.20
6	120	20	w/o	-	0.8	7.7	5.2	0.02-0.18
			w/o	-	0.8	7.4	5.4	0.20
			w	0.10*B*	0.8	7.4	5.4	0.20
			w	0.33*B*	0.8	7.4	5.4	0.20

Model length: 150mm

4.2 Response Characteristics of Rectangular Cylinders of *B/D* = 2, 4, 6 in a Heaving Mode

(1) *B/D*=2.0

Figure 4.2.1 shows the results of the spring-supported tests for the rectangular cross with a side ratio of *B/D*=2.0 with and without the S.P. Regardless of the presence or absence of the S.P., the vortex-induced vibrations were confirmed as occurring from approximately V_r=3. These vortex-induced vibrations are considered to be the motion-induced vortex vibrations, because the onset wind velocities of these vortex-induced vibrations approximately coincided with V_{cr}=1.67*B/D*=3.3. This result has a similar tendency as the previous research[1]. In the two cases with the S.P., the peak response amplitudes of the motion-induced vortex vibrations decreased. In addition, the nearer the S.P. was installed at the downstream side of the model, the smaller the peak response amplitude tended to be. According to the results of the spring-supported test and CFD with different *Sc* numbers[6], with regard to the rectangular cross section with a side ratio of *B/D*=2.0, the maximum response amplitudes in the case with *Sc*=1.6 and the case with *Sc*=2.0 nearly have the same value. Thus, it can be considered that when

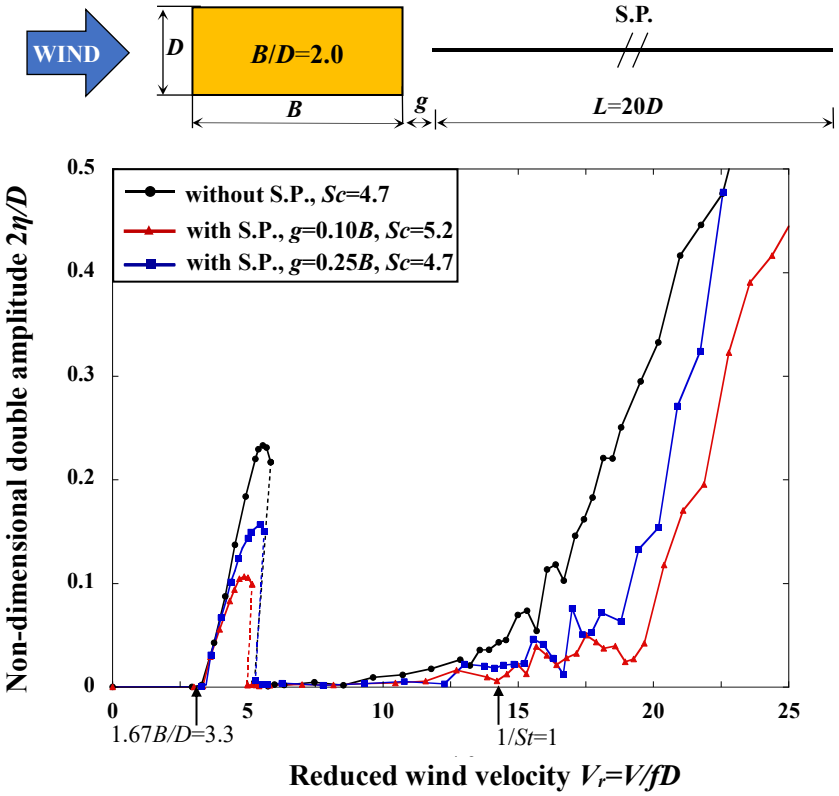

Figure 4.2.1 *V-A* **diagram of *B/D*=2.0 in the heaving mode**

the *Sc* number varies in a small range, it does not have significant influence on the maximum response amplitude of the motion-induced vortex vibration for the cross section of *B/D*=2.0 in the heaving mode. Therefore, although the *Sc* number in the case when the S.P. was installed at *g*=0.10*B* was slightly larger than that in the other two cases, it is deemed that the decline in the maximum response amplitude is primarily caused by the gap length *g*, instead of the difference in the *Sc* number.

Moreover, in the case when the S.P. was not installed, the Kármán vortex-induced vibration was confirmed at V_r=14 approximately and changed to galloping along with the increase in wind velocity. In the two cases when the S.P. was installed at *g*=0.10*B*, 0.25*B*, the Kármán vortex-induced vibration was suppressed. The galloping was confirmed at the higher wind velocity region than that in the case without the S.P.

(2) *B/D*=4.0

The results of the spring-supported tests of *B/D*=4.0 are shown in **Figure 4.2.2**. There were two vortex-induced vibrations confirmed. The first vortex-induced vortex vibration was confirmed occurring from V_r=3, the second one was confirmed occurring from V_r=7 approximately, regardless of the presence or absence of the S.P. These

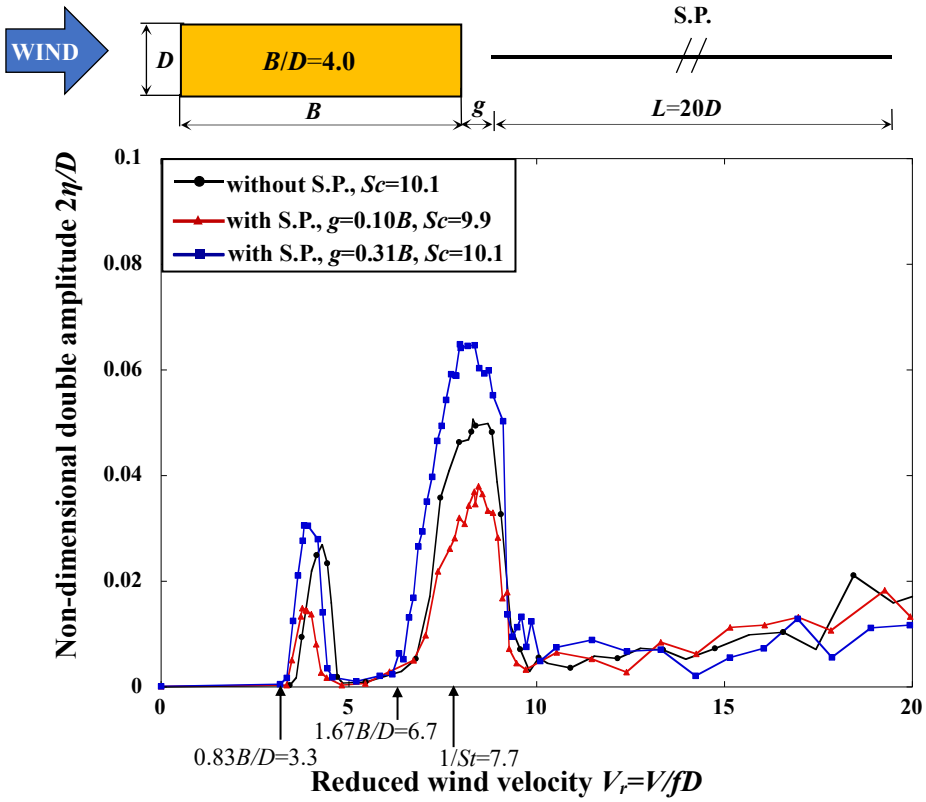

Figure 4.2.2 *V-A* diagram of *B/D*=4.0 in the heaving mode

vortex-induced vibrations are considered to be the motion-induced vortex vibrations. Because the onset wind velocities of these vortex-induced vibrations correspond to the empirical value of the onset wind velocity of the motion-induced vortex vibration V_{cr}=0.83B/D=3.3 and V_{cr}= 1.67B/D=6.7, and there was no change in the onset reduced wind velocity when the S.P. was installed. When the S.P. was installed at g=0.10B, the maximum response amplitude of the motion-induced vortex vibration decreased, whereas it increased when the S.P. was installed at g=0.31B. These results have a similar tendency as the previous researches[2), 3)].

(3) *B/D*=6.0

The results of the spring-supported tests of B/D=6.0 are shown in **Figure 4.2.3**. The vortex-induced vibrations occurring from approximately V_r =5 were confirmed. These vortex-induced vibrations are considered to be the motion-induced vortex vibrations, because they were occurring at V_{cr}=0.83B/D=5.0. In addition, there was no change in the onset reduced wind velocity when the S.P. was installed. Similarly, as the tendency obtained from the results of B/D=4.0, when the S.P. was installed at g = 0.10B, the response amplitude of the motion-induced vortex vibration was suppressed. However, the response amplitude increased when the S.P. was installed at g=0.33B.

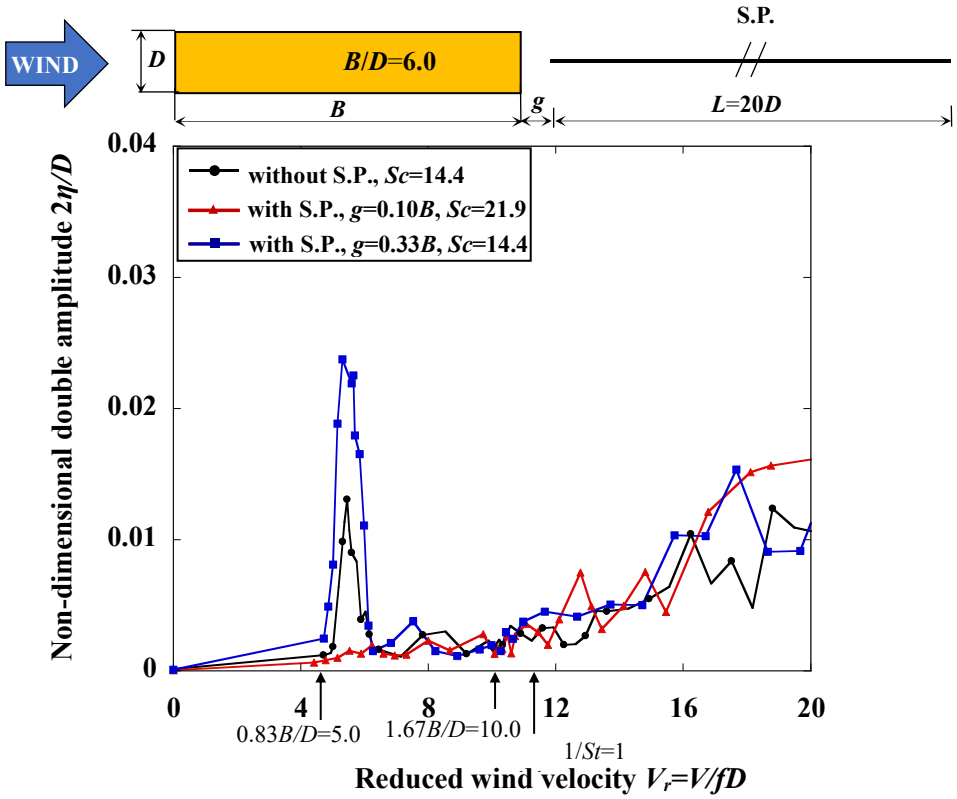

Figure 4.2.3 *V-A* diagram of *B/D*=6.0 in the heaving mode

Meanwhile, the motion-induced vortex vibration which is considered to occur at V_{cr}= 1.67*B/D*=10.0 was not confirmed.

Although the Scruton numbers *Sc* in the results of spring-supported tests for the side ratios of *B/D*=2.0, 4.0, 6.0 were not adjusted to the same value, according to the results of spring-supported tests for the side ratios of *B/D*=3.0, 4.0, 5.0 with the same Scruton number, it is indicated that the maximum response amplitude of the motion-induced vortex vibration tends to become smaller as the side ratio *B/D* becomes larger[7]. In other words, the correlation between the maximum response amplitude and side ratios for the cross sections of *B/D*=2.0, 4.0, 6.0 is contrary to that for the side ratios of *B/D*=0.62-1.18, which have been discussed in chapter 3.

Table 4.2.1 shows the results of flow visualization tests for the side ratios of *B/D*=2.0, 4.0 at the onset reduced wind velocity of the motion-induced vortex vibration,

Table 4.2.1 Results of flow visualization test of *B/D*=2.0, 4.0, 6.0 (2*η*/*D*=0.18)

B/D	V_r=*V*/*fD*	Results of flow visualization test at middle displacement with maximum **upward** velocity	Results of flow visualization test at middle displacement with maximum **downward** velocity
2.0	3.8 ≈1.67*B/D*	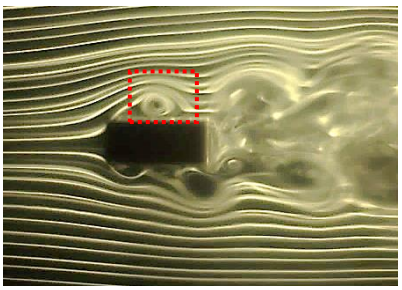	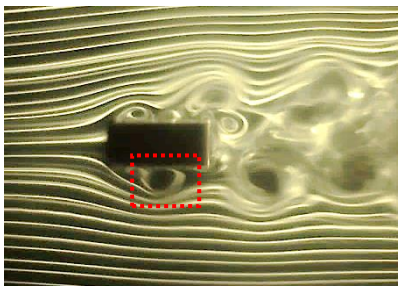
4.0	7.1 ≈1.67*B/D*	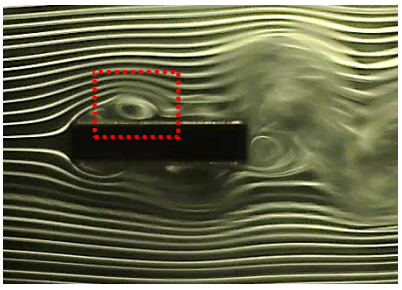	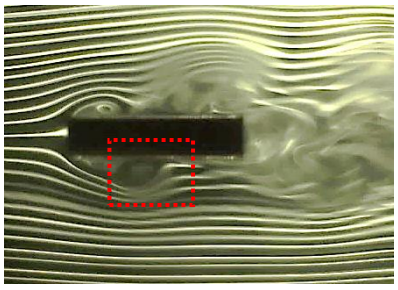
6.0	10.0 =1.67*B/D*	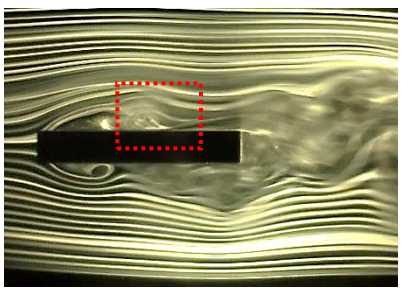	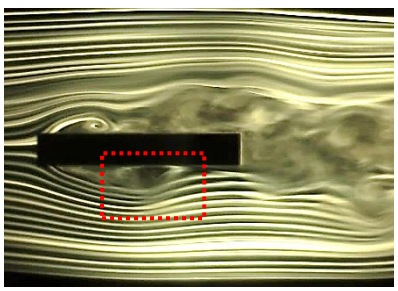

and for B/D=6.0 at the reduced wind velocity of V_r=1.67B/D =10.0 where the motion-induced vortex is considered to occur in the same forced-oscillating amplitude of $2\eta/D$=0.18. By comparing the flow patterns of the separated vortex from leading edge surrounded by a red dotted line in different cross sections, it is found that as the side ratio B/D becomes larger, the separated vortex from leading edge tends to become unstable while moving toward the leeward part of the model. Especially in the case of B/D=6.0, the separated vortex from leading edge dispersed on the middle of the upper and lower surfaces of the model. With regard to this property of the separated vortex from leading edge, a similar tendency was also obtained in the previous wind tunnel test[3]. Therefore, the fluctuating lift provided by the separated vortex from leading edge is considered to become weak as the side ratio B/D becomes larger.

4.3 Necessity of Secondary Vortex at Trailing Edge for the Onset of Motion-induced Vortex vibration for Rectangular Cylinders of *B/D*=2, 4, 6 in a Heaving Mode

In one period of vibration, there will be up to two secondary vortices at trailing edge generated at the rear corner of the model. Therefore, when the model is forced-oscillated for ten periods, there will be up to twenty secondary vortices at trailing edge generated. Thus, the generation probability of the secondary vortex at trailing edge is defined as (the number of generation times in ten periods/20) ×100 (%). It was used as an index showing the extent of the stability of the secondary vortex at trailing edge. Although the formation of the secondary vortex at trailing edge was identified by eye recognition, the generation probability of the secondary vortex at trailing edge was measured by four experimenters. As a result, the generation probabilities of the secondary vortex at trailing edge measured by different experimenters did not show significant differences. Therefore, it is reasonable to evaluate the extent of the stability of the secondary vortex at trailing edge by using the generation probability of the secondary vortex at trailing edge. The results of the generation probability of the secondary vortex at trailing shown in the below were selected from one of the results obtained by all the experimenters.

Figure 4.3.1(a)-Figure 4.3.4(a) show the relation between the generation probability of the secondary vortex at trailing edge calculated in ten periods of vibration and the forced-oscillating amplitude at the wind velocity where the motion-

induced vortex vibration has generated, regarding the cross sections with side ratios of *B/D*=2.0, 4.0, 6.0. **Figure 4.3.1(b)-Figure4.3.4(b)** show the photographs of flow visualization tests in a higher and a lower forced-oscillating amplitude, respectively. A red dotted rectangle was added at the rear corner in the bottom surface in order to recognize whether or not the secondary vortex at trailing edge is generated. **Figure 4.3.1(c)-Figure 4.3.4(c)** show the *V-A* diagrams in the wind velocity region of the motion-induced vortex vibration when the S.P. was not installed.

The separated vortex from leading edge was observed in all the cross sections, regardless of the forced-oscillating amplitude. On the other hand, it was confirmed that

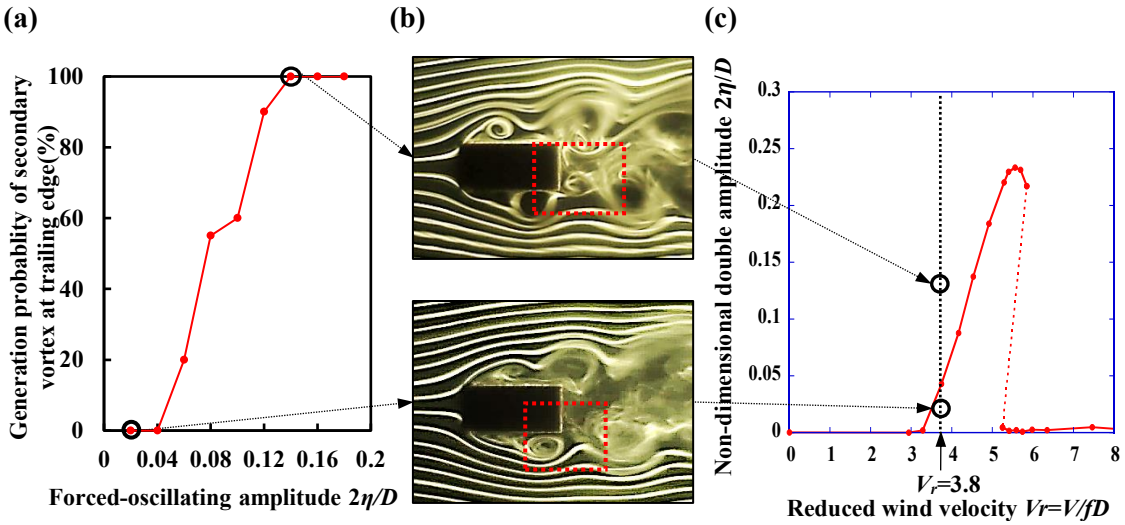

Figure 4.3.1 (a) Generation probability for secondary vortex at trailing edge of *B/D*=2.0 at V_r=3.8, (b) flow visualization result of *B/D*=2.0 at bottom displacement at V_r=3.8 and (c) *V-A* diagram of *B/D*=2.0 (without S.P., *Sc*=4.7)

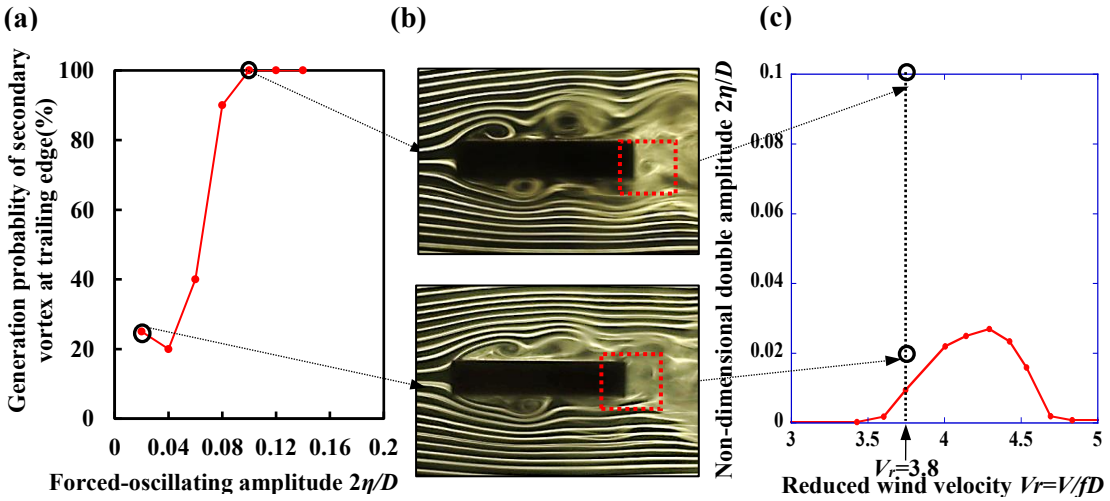

Figure 4.3.2 (a) Generation probability for secondary vortex at trailing edge of *B/D*=4.0 at V_r=3.8, (b) flow visualization result of *B/D*=4.0 at bottom displacement at V_r=3.8 and (c) *V-A* diagram of *B/D*=4.0 (without S.P., *Sc*=10.1)

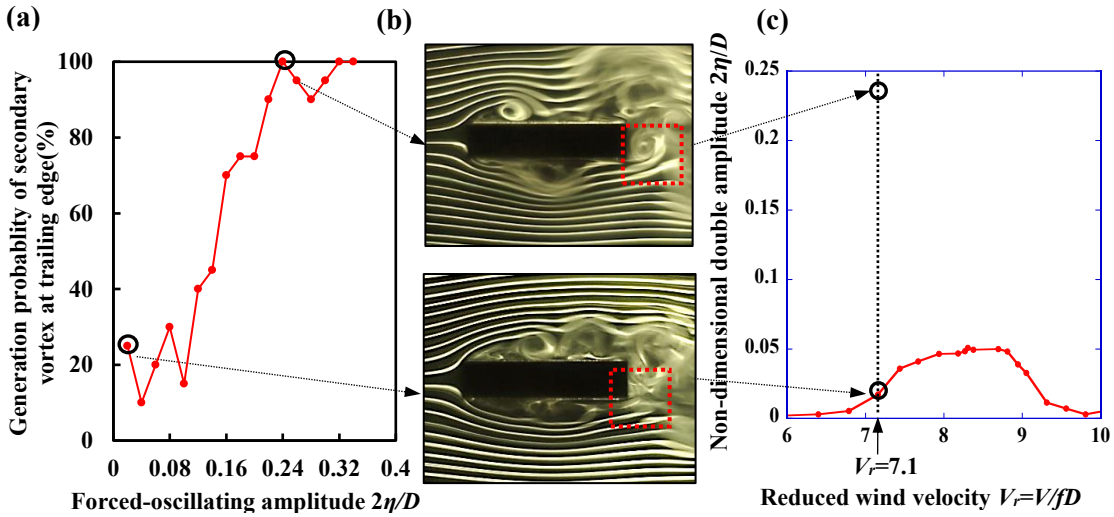

Figure 4.3.3 (a) Generation probability for secondary vortex at trailing edge of *B/D*=4.0 at V_r=7.1, (b) flow visualization result of *B/D*=4.0 at bottom displacement at V_r=7.1 and (c) *V-A* diagram of *B/D*=4.0 (without S.P., *Sc*=10.1)

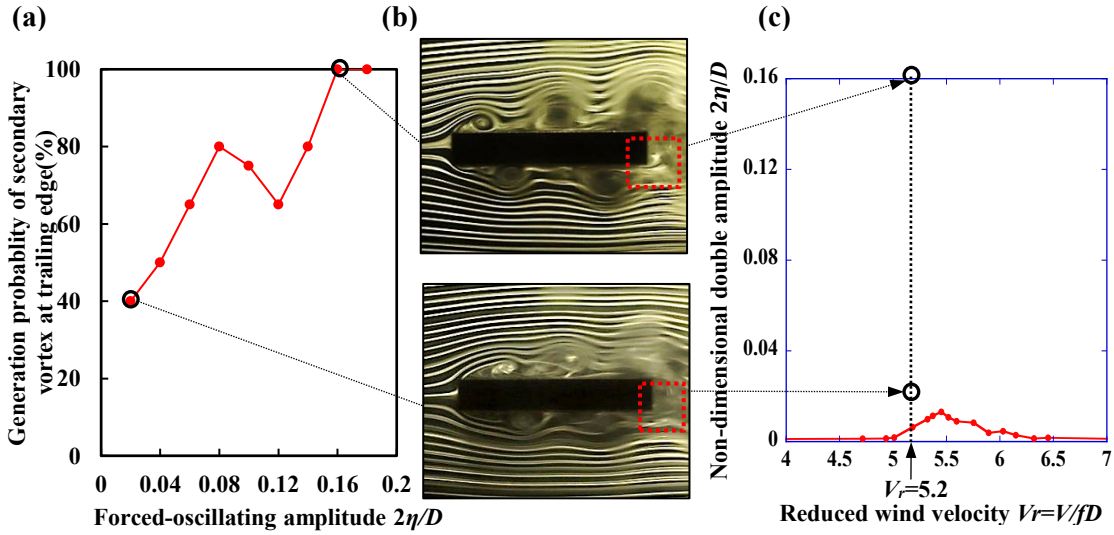

Figure 4.3.4 (a) Generation probability for secondary vortex at trailing edge of *B/D*=6.0 at V_r=5.2, (b) flow visualization result of *B/D*=6.0 at bottom displacement at V_r=5.2 and (c) *V-A* diagram of *B/D*=6.0 (without S.P., *Sc*=14.4)

the generation probability of secondary vortex at the trailing edge can reach 100% only in extremely high forced-oscillating amplitudes, which are much higher than the response amplitude of the motion-induced vortex vibration. For example, in the case of *B/D*=2.0 as shown in **Figure 4.3.1**, the generation probability of the secondary vortex at trailing edge reached 100% in the amplitude of $2\eta/D$=0.14 at a reduced wind velocity of V_r=3.8. This result corresponds to the previous wind tunnel test[1]. However, the secondary vortex at trailing edge was not observed in amplitudes smaller than $2\eta/D$=0.04. In other words, the motion-induced vortex vibration occurred while there was no secondary vortex at trailing edge produced. A similar tendency was confirmed

in the cases of *B/D*=4.0, 6.0 as shown in **Figure 4.3.2-Figure 4.3.4**. At the onset reduced wind velocity of the motion-induced vortex vibration, in a lower forced-oscillating amplitude range, the generation probability of the secondary vortex at trailing edge was very low. This result indicates that the shedding of a secondary vortex at trailing edge is very unstable in low amplitudes. The motion-induced vortex vibration can occur without the stable shedding of the secondary vortex at trailing edge. Therefore, it is suggested that the stable shedding of secondary vortex at trailing edge is not a necessary condition for the generation of the motion-induced vortex vibration for rectangular cross sections with side ratios of *B/D*=2.0, 4.0, 6.0 in the heaving mode.

4.4 The Effect of Secondary Vortex at Trailing Edge on Motion-induced Vortex Vibration at Peak Response for Rectangular Cylinders of *B/D*＝2, 4, 6 in a Heaving Mode

(1) *B/D*=2.0

It is known that the separated vortex from leading edge merges with the secondary vortex at trailing edge at the maximum and minimum displacements in a period of vibration[8]. In order to get a better understanding on the effect of the secondary vortex at trailing edge on the motion-induced vortex vibration, the main attention is concentrated on the flow patterns at the maximum and minimum displacements. **Figure 4.4.1-Figure 4.4.3** show the results of flow visualization tests with and without the S.P. for *B/D*=2.0 in the heaving mode at the vicinity of the maximum and minimum displacement at V_r=5.5 where the maximum response amplitude of the motion-induced vortex vibration occurred in the same forced-oscillating amplitude of $2\eta/D$=0.20. A red dotted rectangle was added at the rear corner in order to confirm the effect of the secondary vortex at trailing edge on the flow field characteristics. On one hand, in the case when the S.P. was not installed, it is observed that the separated vortex from leading edge merged with the secondary vortex at trailing edge strongly at the rear corner of the upper and bottom displacement, as shown in **Figure 4.4.1**. On the other hand, in the two cases when S.P. was installed at g=0.10B and g=0.25B, the development of the integrated vortex which was composed of the separated vortex from leading edge and the secondary vortex at trailing edge was inhibited due to the installation of the S.P. The intensity of the separated vortex from leading edge at the rear corner of the model was also weakened, as shown in

Figure 4.4.2 and **Figure 4.4.3**

In addition, according to the result of unsteady pressure distribution of B/D=2.0 in the heaving mode when the motion-induced vortex vibration occurs, the force acting on the leeward part of the model is an exciting force while the force acting on the

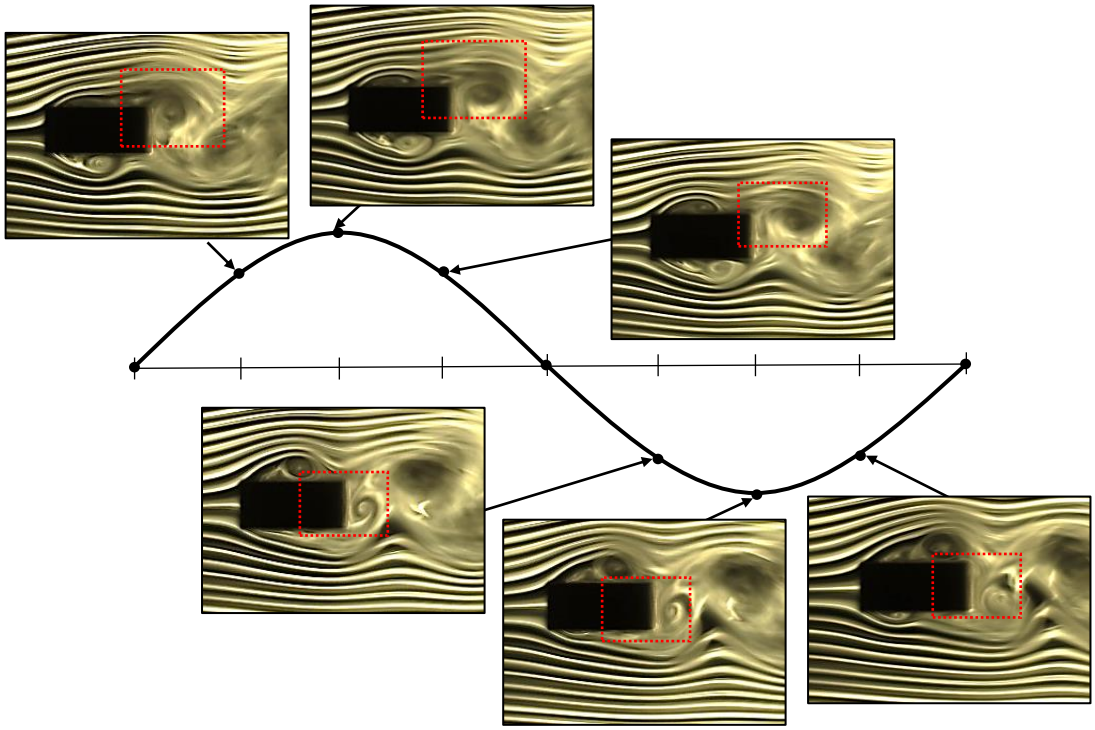

Figure 4.4.1 Results of Flow visualization tests for B/D=2.0 without S.P. in $2\eta/D$=0.20 at V_r=5.5

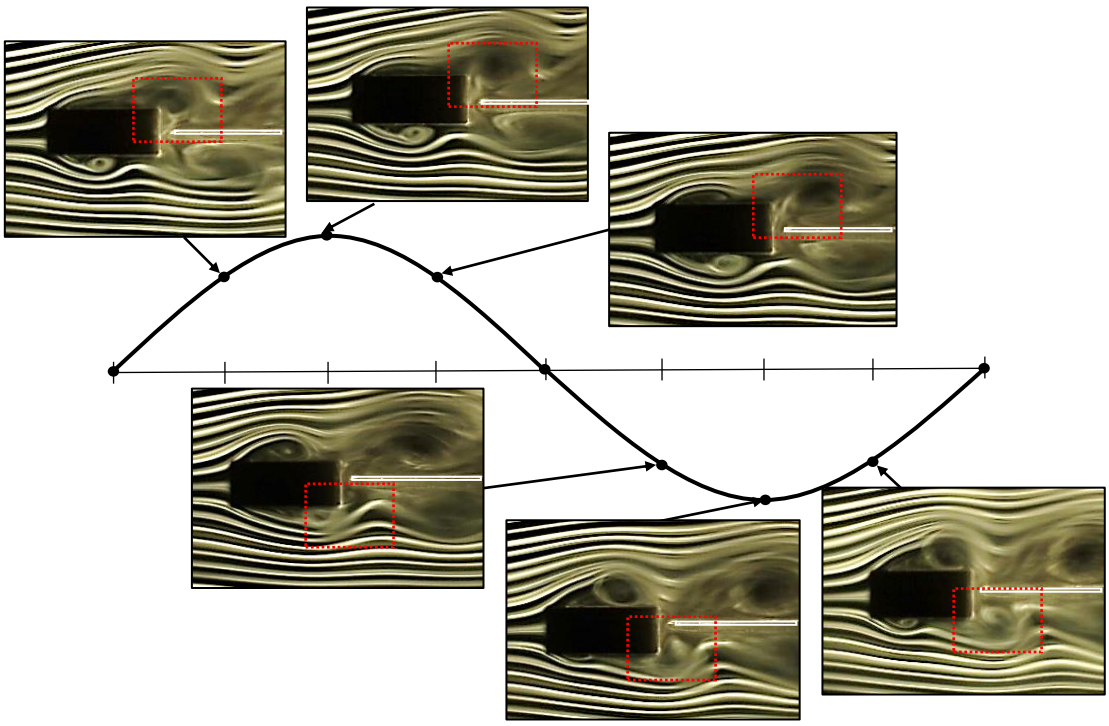

Figure 4.4.2 Results of Flow visualization tests for B/D=2.0 with S.P. (g=0.10B) in $2\eta/D$=0.20 at V_r=5.5

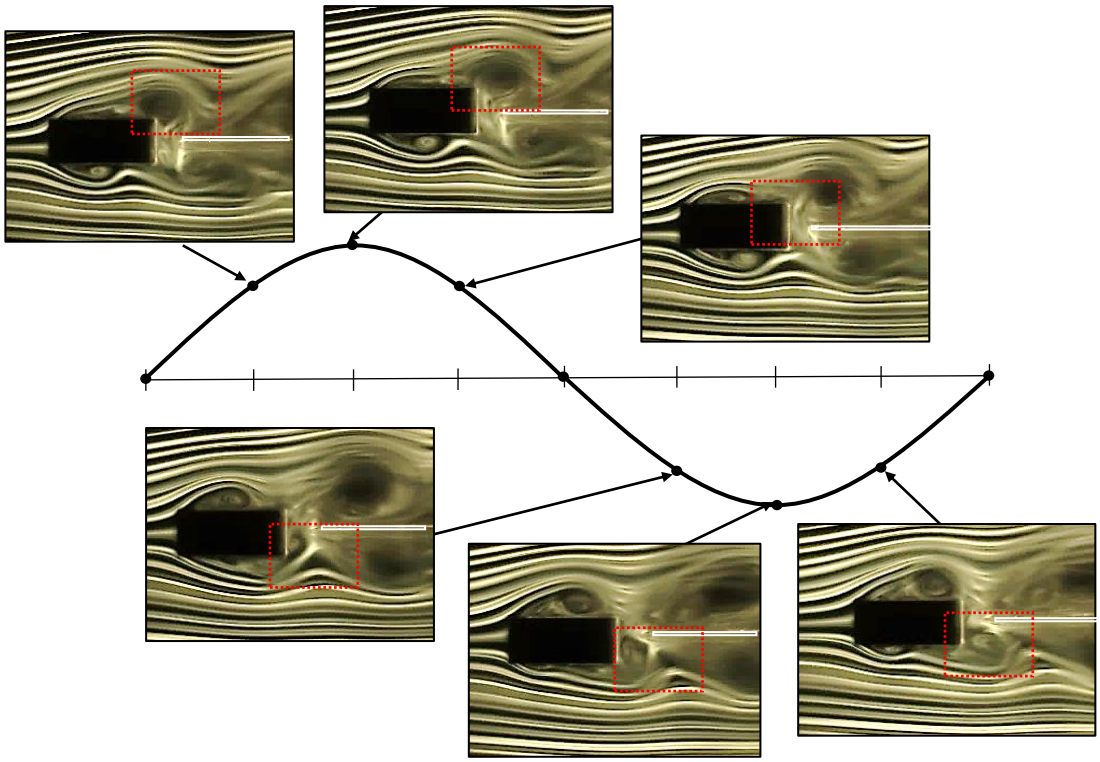

Figure 4.4.3 Results of Flow visualization tests for *B/D*=2.0 with S.P. (*g*=0.25*B*) in $2\eta/D$=0.20 at V_r=5.5

windward part of the model is a damping force[9]. Thus, it can be considered that the intensity of the integrated vortex composed of the separated vortex from leading edge and the secondary vortex at trailing edge has significant influence on the exciting force acting on the model. Therefore, it is suggested that the decline in the maximum response amplitude was attributed to the inhibition of the integrated vortex consisting of the separated vortex from leading edge and the secondary vortex at trailing edge. In other words, at the wind velocity where the maximum response amplitude of the motion-induced vortex vibration occurs, the secondary vortex at trailing edge can be relevant to the magnitude of the exciting force in a way that affects the intensity of the integrated vortex at the rear corner of the model for the rectangular cross section with the side ratio of *B/D*=2.0 in the heaving mode.

(2) *B/D*=4.0

Figure 4.4.4-Figure 4.4.6 show the results of flow visualization tests with and without the S.P. for *B/D*=4.0 in the heaving mode at the vicinity of the maximum and minimum displacement at V_r=8.3 where the maximum response amplitude of the motion-induced vortex vibration with an onset reduced wind velocity of V_{cr}=1.67*B/D* =6.7 occurred in the same forced-oscillating amplitude of $2\eta/D$=0.20. In the case when

the S.P. was installed at g=0.10B, the entrainment of the integrated vortex composed of the separated vortex from leading edge and the secondary vortex at trailing edge was inhibited due to the installation of the S.P. in comparison with the case when the S.P. was not installed, as shown in **Figure 4.4.4** and **Figure 4.4.5**. Besides, the result of unsteady pressure distribution of B/D=4.0 in the heaving mode indicates that the force acting on the leeward part of the model is an exciting force when the motion-induced vortex vibration occurs[6]. In other words, the intensity of the integrated vortex composed of the separated vortex from leading edge and the secondary vortex at trailing edge has significant influence on the exciting force acting on the model, just as the same as the cross section of B/D=2.0. Therefore, it is suggested that the reduction in the maximum response amplitude of the motion-induced vortex vibration was attributed to the inhibition of the integrated vortex consisting of the separated vortex from leading edge and the secondary vortex at trailing edge.

By comparing the case when the S.P. was installed at g=0.31B with the case without the S.P., it is confirmed that the integrated vortex of the separated vortex from leading edge and the secondary vortex at trailing edge was flowed away from the

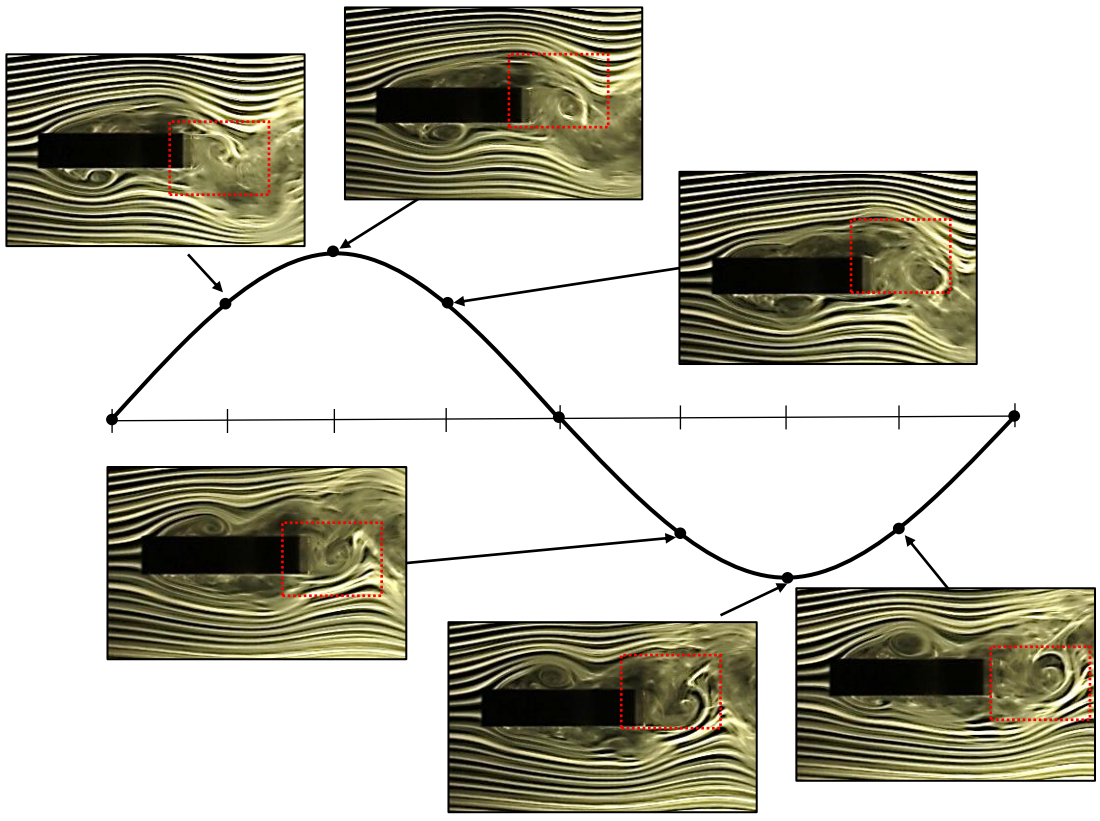

Figure 4.4.4 Results of Flow visualization tests for B/D=4.0 without S.P. in $2\eta/D$=0.20 at V_r=8.3

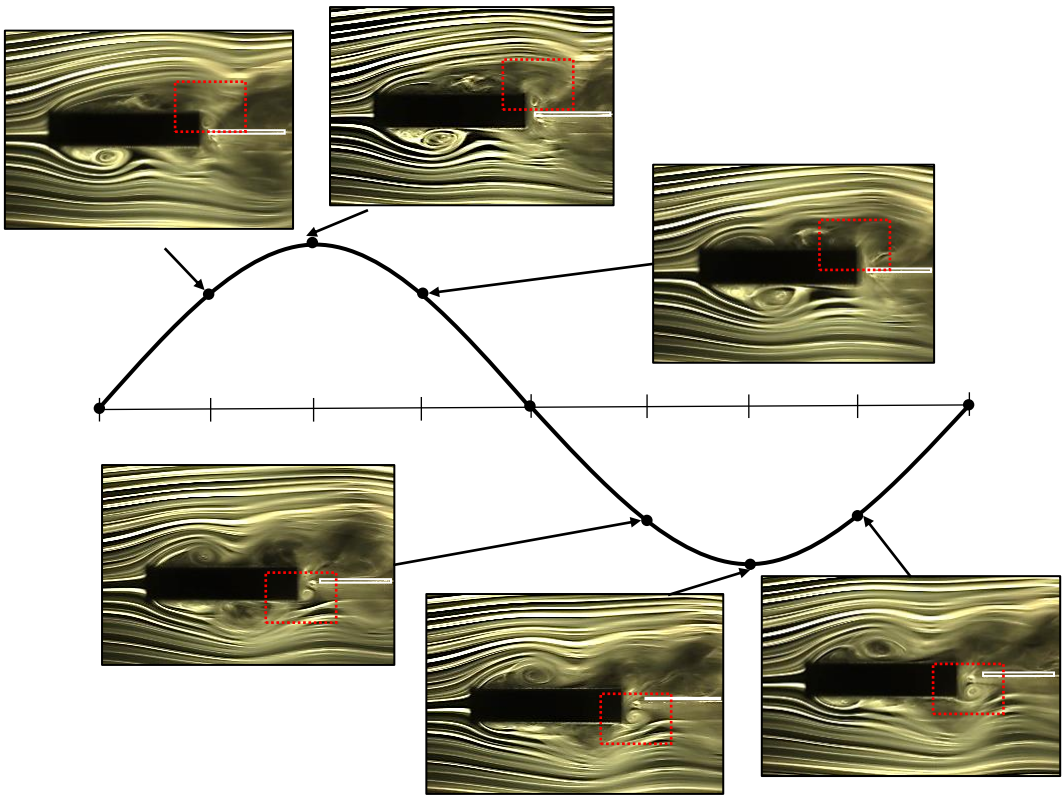

Figure 4.4.5 Results of Flow visualization tests for B/D=4.0 with S.P. (g=0.10B) in $2\eta/D$=0.20 at V_r=8.3

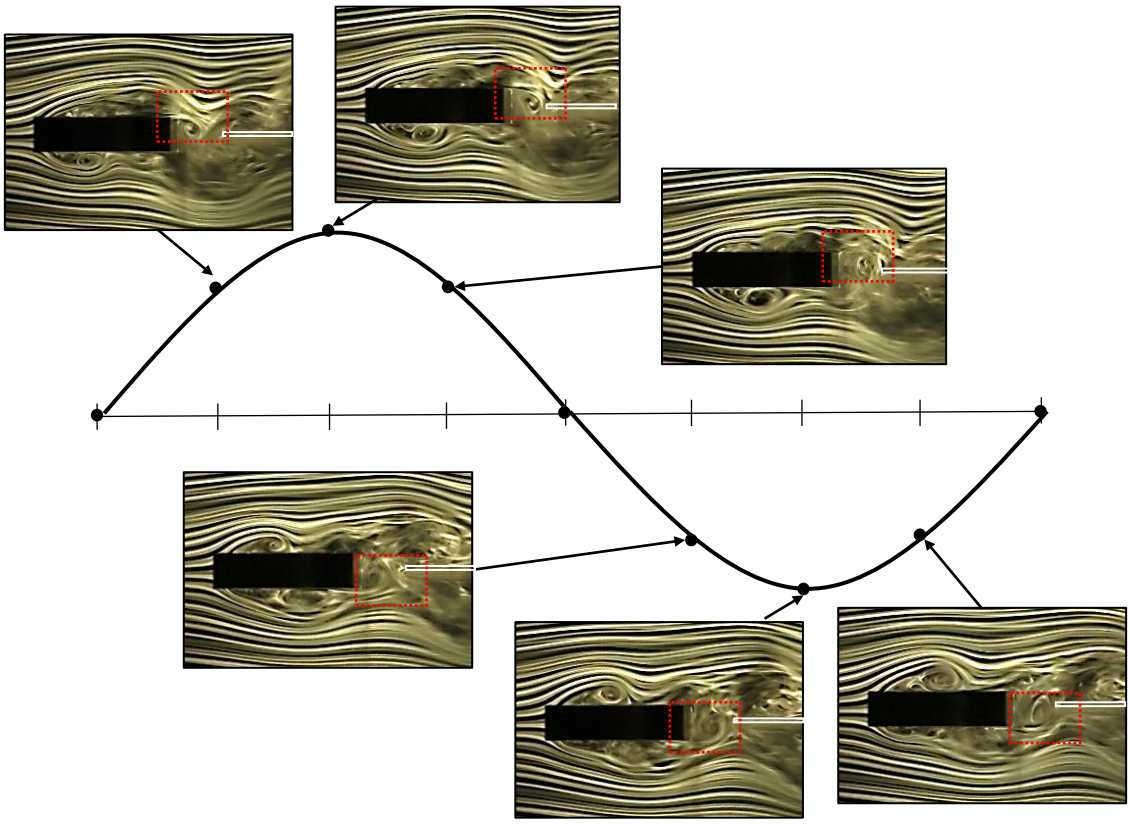

Figure 4.4.6 Results of Flow visualization tests for B/D=4.0 with S.P. (g=0.31B) in $2\eta/D$=0.20 at V_r=8.3

model in the case without S.P., whereas in the case when the S.P. was installed at g=0.31B, it is confirmed that the entrainment of the integrated vortex tended to become stronger and enter the gap between the S.P. and the model, as shown in **Figure 4.4.4** and **Figure 4.4.6**. Hence, it is supposed that when the S.P. was installed at g=0.31B, not only the Kármán vortex was suppressed, but the intensity of the integrated vortex composed of the separated vortex from leading edge and the secondary vortex at trailing edge became stronger. As a result, the exciting force acting on the model became large, and the maximum response amplitude of the motion-induced vortex vibration also became large. By combining these three cases with and without the S.P., it is suggested that the decrease or increase in the maximum response amplitude depends on the intensity of the integrated vortex. In other words, the secondary vortex at trailing edge can be relevant to the magnitude of the exciting force in a way that affects the intensity of the integrated vortex composed of the separated vortex from leading edge and the secondary vortex at trailing edge.

Figure 4.4.7-Figure 4.4.9 show the results of flow visualization tests with and without the S.P. for B/D=4.0 in the heaving mode at the vicinity of the maximum and

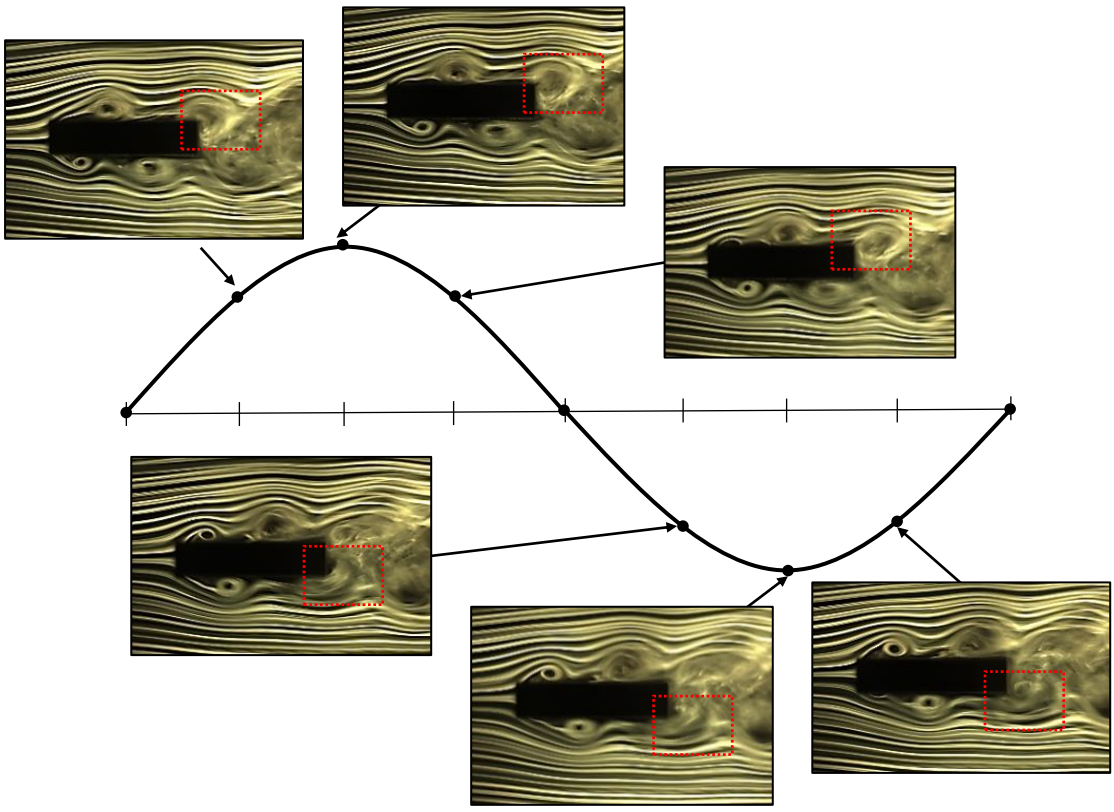

Figure 4.4.7 Results of Flow visualization tests for B/D=4.0 without S.P. in $2\eta/D$=0.20 at V_r=4.3

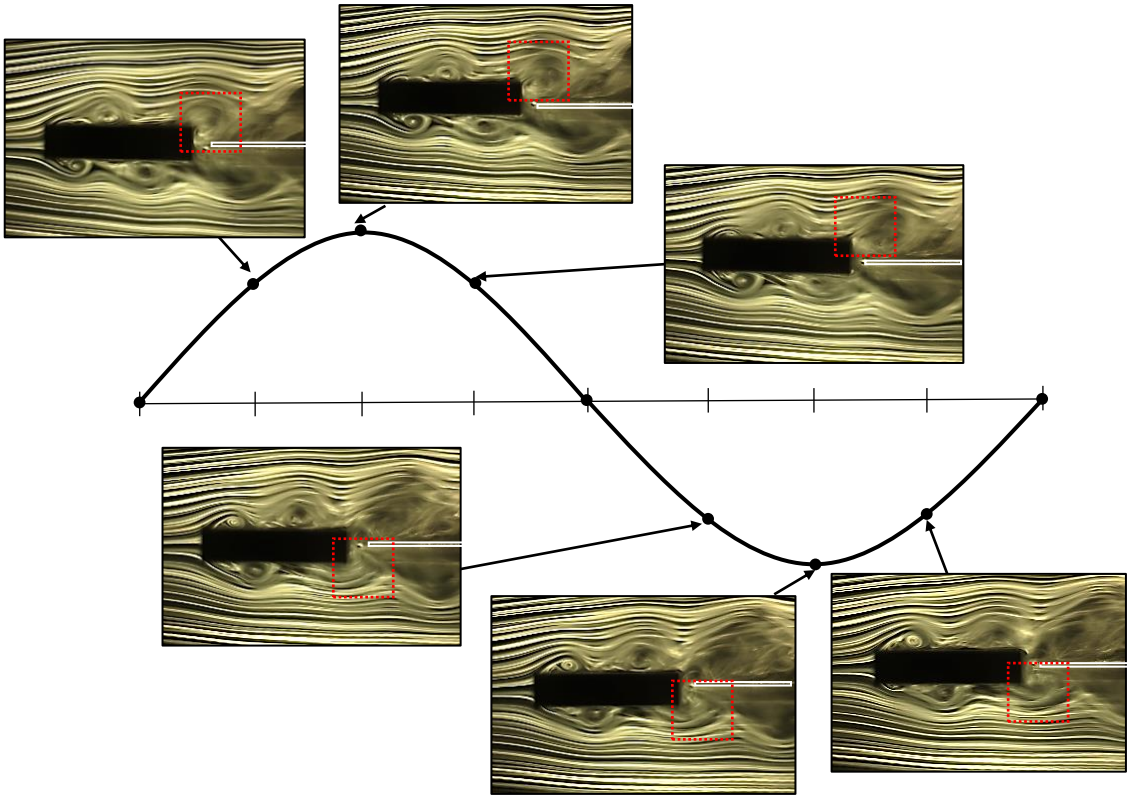

Figure 4.4.8 Results of Flow visualization tests for B/D=4.0 with S.P. (g=0.10B) in $2\eta/D$=0.20 at V_r=4.3

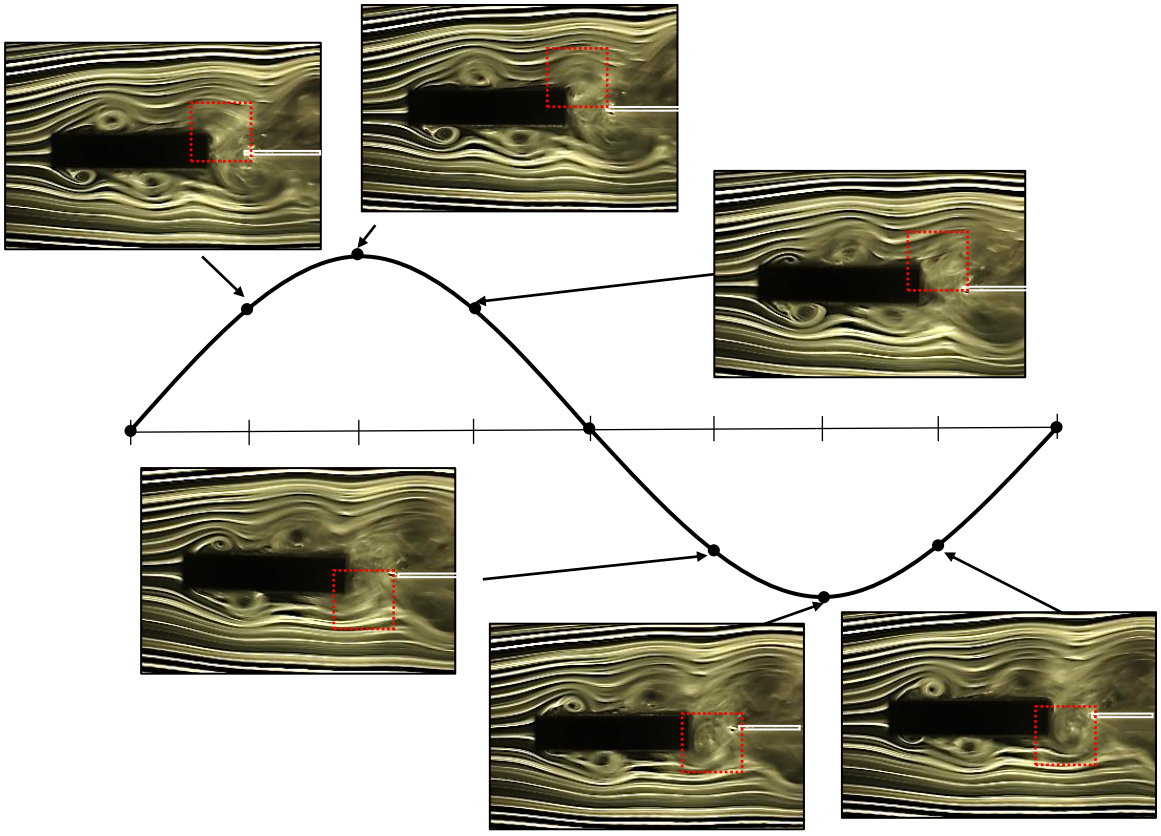

Figure 4.4.9 Results of Flow visualization tests for B/D=4.0 with S.P. (g=0.31B) in $2\eta/D$=0.20 at V_r=4.3

minimum displacement at V_r=4.3 where the maximum response amplitude of the motion-induced vortex vibration with an onset reduced wind velocity of V_{cr}=0.83*B/D* =3.3 occurred in the same forced-oscillating amplitude of $2\eta/D$=0.20. On one hand, in the case when the S.P. was installed at g=0.10*B*, the integrated vortex was inhibited due to the installation of the S.P. in comparison with the case without the S.P., as shown in **Figure 4.4.7** and **Figure 4.4.8**. Thus, it is suggested that the reduction in the maximum response amplitude was also attributed to the inhibition of the integrated vortex of the separated vortex from leading edge and secondary vortex at trailing edge. On the other hand, in the case when the S.P. was installed at g=0.31*B*, it is confirmed that the entrainment of the integrated vortex tended to become stronger and enter the gap between the S.P. and the model, as shown in **Figure 4.4.7** and **Figure 4.4.9**, although the degree of the enhancement of the integrated vortex is not as distinct as that at V_r=8.3. Therefore, it is suggested that the secondary vortex at trailing edge can be relevant to the magnitude of the exciting force in a way that affects the intensity of the integrated vortex composed of the separated vortex from leading edge and the secondary vortex at trailing edge for the rectangular cross section with the side ratio of *B/D*=4.0 in the heaving mode.

(3) *B/D*=6.0

Figure 4.4.10-Figure 4.4.12 show the results of flow visualization tests with and without the S.P. for *B/D*=6.0 in the heaving mode at the vicinity of the maximum and minimum displacement at V_r=5.4 where the maximum response amplitude of the motion-induced vortex vibration occurred in the same forced-oscillating amplitude of $2\eta/D$=0.20. By comparing the case when the S.P. was not installed with the cases when the S.P. was installed at g=0.10*B* and g=0.33*B*, it can be observed that the generation patterns of the secondary vortex at trailing edge in all three cases have the same tendency as those in the cross section of *B/D*=4.0. When the S.P. was installed at g=0.10*B*, the integrated vortex composed of the separated vortex from leading edge and the secondary vortex at trailing edge was inhibited due to the installation of the S.P. When the S.P. was installed at g=0.33*B*, the entrainment of the integrated vortex tended to become stronger and enter the gap between the S.P. and the model. Thus, it can be considered that the secondary vortex at trailing edge can be relevant to the

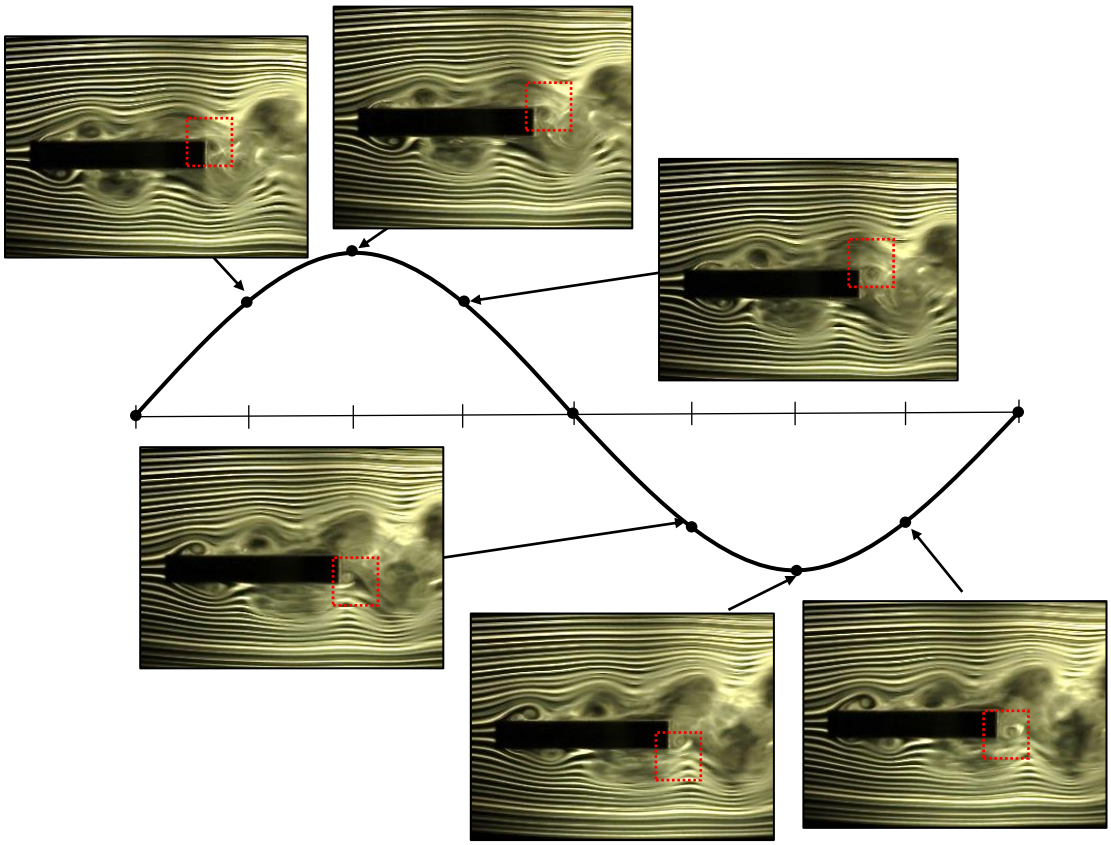

Figure 4.4.10 Results of Flow visualization tests for B/D=6.0 without S.P. in $2\eta/D$=0.20 at V_r=5.4

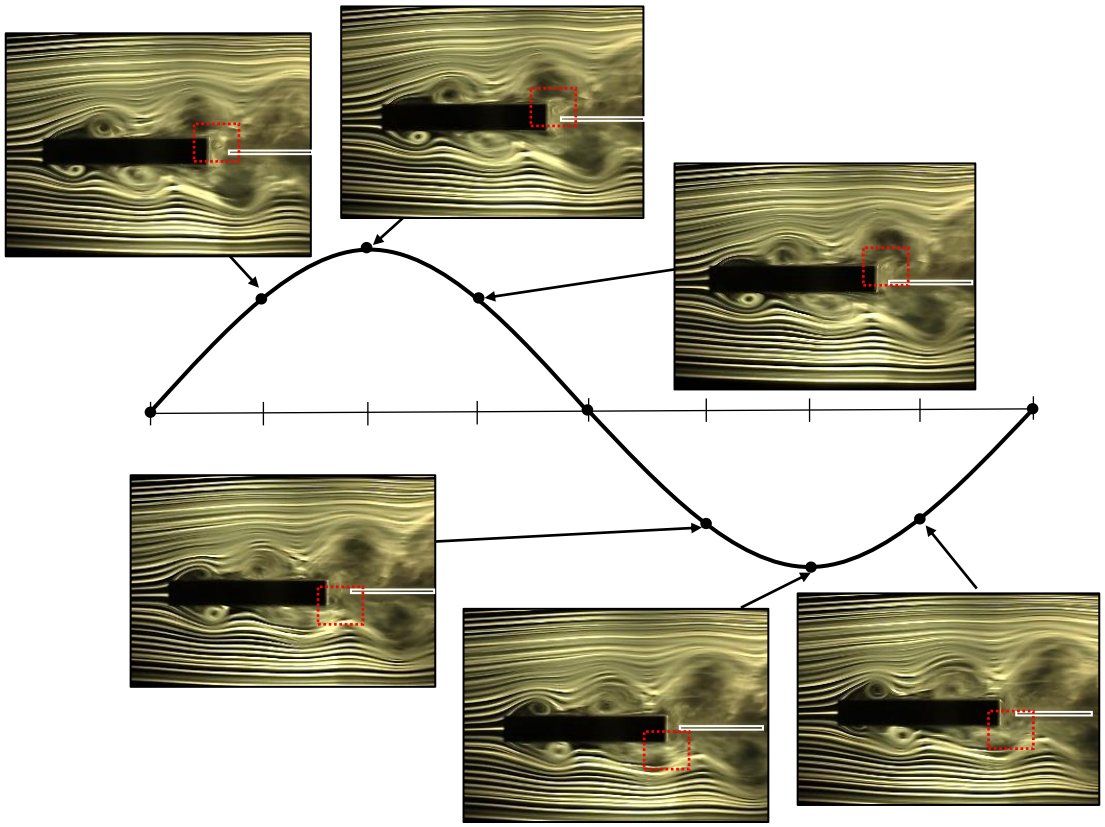

Figure 4.4.11 Results of Flow visualization tests for B/D=6.0 with S.P. (g=0.10B) in $2\eta/D$=0.20 at V_r=5.4

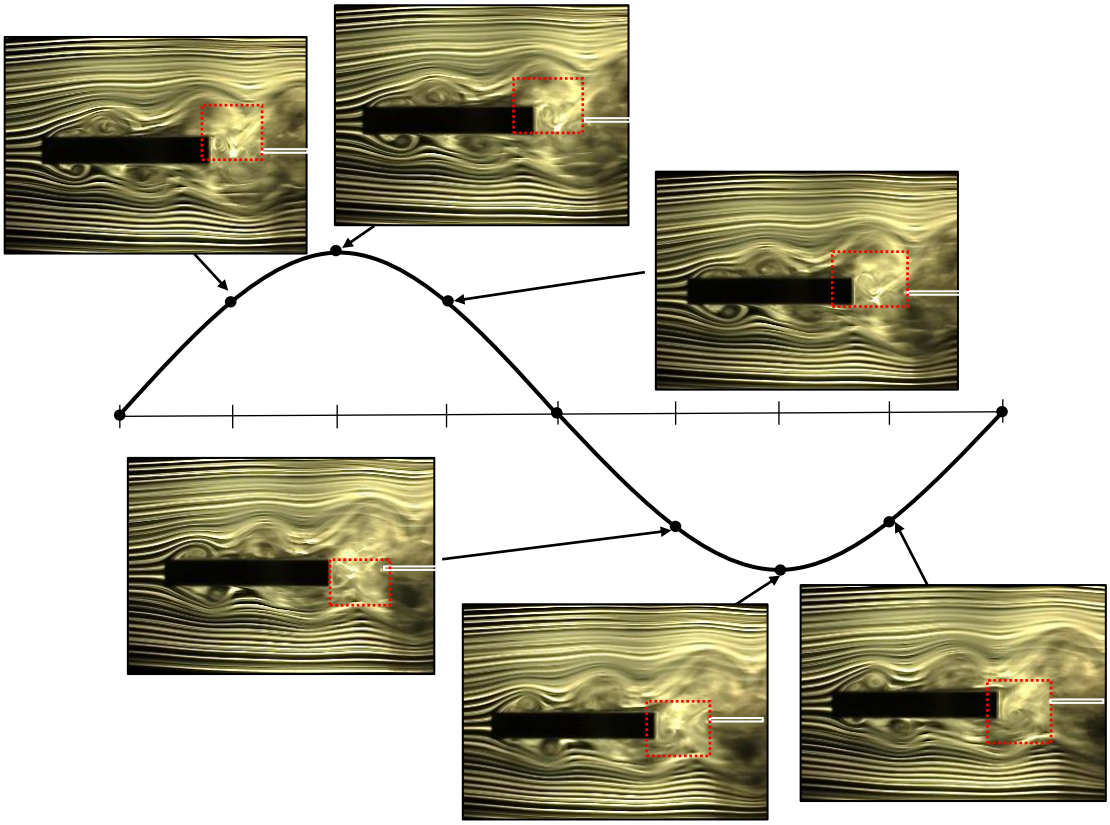

Figure 4.4.12 Results of Flow visualization tests for *B/D*=6.0 with S.P. (*g*=0.33*B*) in $2\eta/D$=0.20 at V_r=5.4

magnitude of the exciting force in a way that affects the intensity of the integrated vortex composed of the separated vortex from leading edge and the secondary vortex at trailing edge for the rectangular cross section with the side ratio of *B/D*=6.0 in the heaving mode.

4.5 Summary

This chapter concentrates on the rectangular cross sections with side ratios of *B/D*=2.0-8.0 where the motion-induced vortex vibration is considered to occur. Spring-supported and flow visualization tests in the heaving mode for rectangular cross sections with side ratios of *B/D*=2.0, 4.0, 6.0 are introduced. The response characteristic of rectangular cross sections with side ratios *B/D*=2.0, 4.0, 6.0 are confirmed. Subsequently, the necessity of the secondary vortex at trailing edge for the motion-induced vortex vibration for rectangular cross sections with side ratios of *B/D*=2.0, 4.0, 6.0 are investigated. Further, the effect of the secondary vortex at trailing edge on the response characteristics of the motion-induced vortex vibration at peak response amplitude is discussed. As a consequence, following conclusions have been drawn:

1. Regarding the rectangular cross sections with side ratios of *B/D*=2.0-6.0, as the side ratio *B/D* increases, the separated vortex from leading edge tends to become unstable while moving toward the leeward part of the model. Thus, the fluctuating lift provided by the separated vortex from leading edge is considered to decrease. As a result, the maximum response amplitude of the motion-induced vortex vibration decreases as the side ratio *B/D* becomes larger.

2. At the onset wind velocity of the motion-induced vortex vibration, the stable shedding of the secondary vortex at trailing edge is not a necessary condition for the generation of motion-induced vortex vibration for rectangular cross sections with side ratios of *B/D*=2.0, 4.0, 6.0 in the heaving mode.

3. On the other hand, at the peak response amplitude of the motion-induced vortex vibration, the secondary vortex at trailing edge can be relevant to the magnitude of the exciting force acting on the model in terms of affecting the intensity of the integrated vortex consisting of the separated vortex from leading edge and the secondary vortex at trailing edge for rectangular cross sections with side ratios of *B/D*=2.0, 4.0, 6.0 in the heaving mode.

References

1) Shiraishi, N. and Matsumoto, M., 1983. On classification of vortex-induced oscillation and its application for bridge structures, Journal of Wind Engineering and Industrial Aerodynamics, 14 (1-3), 419-430.
2) Matsumoto, M., Shiraishi, N., Shirato, H., Stoyanoff, S. and Yagi, T., 1993. Mechanism of, and turbulence effect on vortex- induced oscillations for bridge box girders, Journal of Wind Engineering and Industrial Aerodynamics, 49 (1-3), 467-476.
3) Matsumoto, M., Yagi, T., Tamaki, H. and Tsubota, T., 2008. Vortex-induced vibration and its effect on torsional flutter instability in the case of B/D=4 rectangular cylinder, Journal of Wind Engineering and Industrial Aerodynamics, 96 (6-7), 971-983.
4) Okajima, A., 1990. Numerical simulation of flow around rectangular cylinders, Journal of Wind Engineering and Industrial Aerodynamics, 33, 171-180.
5) Okajima, A, 1983. Flow around a rectangular cylinder with a section of various width/height ratios, Journal of Wind Engineering, Japan Association for Wind Engineering, 17, 1-19. (in Japanese)
6) Shimada, K. and Ishihara, T., 2012. Predictability of unsteady two-dimensional *k*-*ε* model on the aerodynamic instabilities of some rectangular prisms, Journal of Fluids and Structures, 28, 20-39.
7) Shimada, K., 1999. Evaluation of aerodynamic characteristics and aerodynamic elasticity behavior forecast of rectangular cylinders using k-ε model, Doctor's thesis, Kyoto University. (in Japanese)
8) Shiraishi, N. and Matsumoto, M., 1984. On physical mechanism of vortex-induced oscillation and its response evaluation, Journal of Wind Engineering, Japan Association for Wind Engineering, 20, 103-127. (in Japanese)
9) Miyata, T., Miyazaki, M. and Yamada, H., 1983. Pressure distribution measurements for wind induced vibrations of box girder bridges, Journal of wind Engineering and Industrial Aerodynamics, 14, 223-234.

Chapter 5: The Role of Secondary Vortex at Trailing Edge in Motion-induced Vortex Vibration for Rectangular Cylinders of *B/D* =2, 4, 6 in a Torsional Mode

Although the effect of the secondary vortex at trailing edge on the response characteristic of the motion-induced vortex vibration for the rectangular cross sections with side ratios of *B/D*=0.62-6.0 in the heaving mode was clarified qualitatively in chapter 3 and chapter 4, it is still unclear in the torsional mode. Besides, there are only a little previous researches focusing on the aerodynamic characteristics of the motion-induced vortex vibration in the torsional mode, and much less on the flow patterns of the secondary vortex at trailing edge. This chapter therefore aims to give a more comprehensive explanation on the effect of the secondary vortex at trailing edge on the motion-induced vortex vibration in the torsional mode. Rectangular cross sections with side ratios of *B/D*=2.0, 4.0, 6.0 were selected as the target cross sections, because it is deemed that rectangular cross sections with side ratios of *B/D*=2.0-8.0 are the acknowledged cross sections where the motion-induced vortex vibration has been confirmed to occur, according to the summary of the results of previous wind tunnel tests[1]. Spring-supported and flow visualization tests were carried out, in order to clarify the role of the secondary vortex at trailing edge in the motion-induced vortex vibration in the torsional mode for the rectangular cross sections with side ratios of *B/D*=2.0, 4.0, 6.0.

5.1 Wind Tunnel Tests for Rectangular Cylinders of *B/D*=2, 4, 6 in a Torsional Mode

5.1.1 Spring-supported Tests

(1) Wind tunnel

In order to obtain the response characteristics of the target rectangular cross sections, the spring-supported tests in the torsional mode were conducted in a closed circuit wind tunnel at Kyushu Institute of Technology. This closed circuit wind tunnel is the same as the one which has been demonstrated in chapter 3. The spring-supported

tests were carried out in a smooth flow with a turbulence intensity of less than 0.5%. The wind velocity V in the spring-supported tests was from 1.5m/s to 9.6m/s. The Reynolds number in the wind velocity region of the motion-induced vortex vibration was $Re=VD/\nu=9.6\times10^3$-1.7×10^4, where V: wind velocity (m/s), D: cross-wind length (m), ν: kinematic viscosity (m^2/s).

(2) Specifications of target models and splitter plate

Rectangular cross sections with side ratios of B/D=2.0, 4.0, 6.0 were selected as the target cross sections. The model of B/D=2.0 was constructed of cypress wood attached with two end plates at both ends of the model, in order to make the flow around the models appear as a two-dimensional flow. The models of B/D=4.0, 6.0 were the composed of the model of B/D=2.0 and cubic polystyrene foams whose purpose was to alter the side ratios of the models. In addition, an L-type aluminum rod was attached to each corner of the models of B/D=4.0, 6.0, for the sake of making the corner as sharp as possible. Two end plates were also attached to both ends of the models of B/D=4.0, 6.0. **Figure 5.1.1** shows the models of B/D=2.0, 4.0 used in spring-supported tests. It should be noted that in the case of B/D=2.0, according to the result of the previous wind tunnel test, the response amplitude of the motion-induced vortex vibration can be confirmed only when the Sc number is sufficiently small[2)]. Therefore, in order to reduce the Sc number of B/D=2.0 as much as possible so that the spring-supported tests for B/D=2.0 can be carried out successfully, a larger model was used and the blockage ratio was moderated to 10%. With regard to this moderation of the blockage ratio, according to the past results of spring-supported tests for B/D=1.18

(a) **(b)**

Figure 5.1.1 (a) Sectional models of B/D=2.0 and (b) B/D= 4.0 in the wind tunnel

with blockage ratio of 10% and 5%, it was confirmed that the difference in blockage ratio did not influence the response characteristics in the wind region of motion-induced vortex vibration[3), 4)]. Therefore, it can be considered that the influence of the moderation of blockage ratio for *B/D*=2.0 in the wind velocity region of the motion-induced vortex vibration is small. **Table 5.1.1** shows the size of the target models.

Table 5.1.1 The size of the target models used in spring-supported tests

Side ratio *B/D*	2.0	4.0	6.0
Along-wind length *B*(mm)	360	360	540
Cross-wind length *D*(mm)	180	90	90
Model length *L*(mm)	828		
Aspect ratio *L/D*	4.6	9.2	9.2

According to the results of previous wind tunnel tests, with regard to the rectangular cross sections with side ratios of *B/D*=4.0, 6.0, the reduced frequencies of the separated vortex from leading edge 0.6*D/B* and the Strouhal number *St* have a close value in the heaving mode[5)]. Thus, in the wind velocity region where motion-induced vortex vibration occurs, the Kármán vortex synchronizing with the vibration of the model strongly interferences with the separated vortex from leading edge and the secondary vortex at trailing edge. In the torsional mode, although the reduced frequencies of the separated vortex from leading edge 0.9*D/B* and the Kármán vortex *St* are not as close as they are in the heaving mode[6)], it is deemed that the separated vortex from leading edge and the secondary vortex at trailing edge still can be influenced by the Kármán vortex to some extent. Nevertheless, the main research objective in this study is the effect of the secondary vortex at trailing edge on the motion-induced vortex vibration. Therefore, a splitter plate (hereinafter referred to as S.P.) was installed at the downstream of the model with a gap length *g* for the sake of weakening the influence of the Kármán vortex.

In general, although the S.P. is usually used as a tool for suppressing the Kármán vortex, it does not have a direct relation with the separated vortex from leading edge and the secondary vortex at trailing edge. However, it has been revealed that different

gap lengths have different effects on the response characteristics of motion-induced vortex vibration in the heaving mode[5), 7)]. Thus, it is deemed that the interaction between the separated vortex from leading edge and the secondary vortex at trailing edge is different due to the difference in the gap length. Therefore, in the present study, two different gap lengths were provided to each cross section for confirming the flow patterns of the separated vortex from leading edge and the secondary vortex at trailing edge in the torsional mode.

On the other hand, it is indicated that the Kármán vortex has an effect which can reduce the separated vortex from leading edge, according to previous wind tunnel tests[7)]. Regarding the cross section of B/D=2.0, the values of the reduced frequencies of the separated vortex from leading edge and the Strouhal number St separate with each other[5)]. Hence, it can be considered that the influence of the Kármán vortex on the motion-induced vortex vibration for B/D=2.0 is remarkably different from that for B/D=4.0, 6.0. In order to compare the influence of the Kármán vortex on the motion-induced vortex vibration in various side ratios, the S.P. was also used for the cross section of B/D=2.0. In order to ensure that the Kármán vortex can be eliminated effectively, the along-wind lengths of the S.P. were set as 20D [(3600mm for B/D=2 (D=180mm), 1800mm for B/D=4, 6 (D=90mm)] which is considered to be long enough, by referring to previous wind tunnel tests[7)]. The width and thickness of the S.P. were 900mm and 13mm, respectively. **Figure 5.1.2** shows setting situation of the S.P. inside the wind tunnel for the model of B/D=2.0.

Figure5.1.2 Setting situation of the S.P. in the wind tunnel

(3) Measurement system

The measurement system is the same as the one which has been demonstrated in chapter 3. The angle of attack was set as 0° for all the experiments. All the models were suspended by two cross springs arranged at both sides of the wind tunnel, so that the models could only oscillate in the torsional mode with respect to the axis of rotation. The axis of rotation was in the centroid of the cross section. The response amplitude of the models during vibration was measured by a laser displacement detector. **Figure 5.1.3** shows the suspension situation outside the wind tunnel. The vibration system was so well designed that the structural damping of the vibration system could be reduced to as small as possible. The structural damping of the vibration system was adjusted with a pair of magnetic dampers.

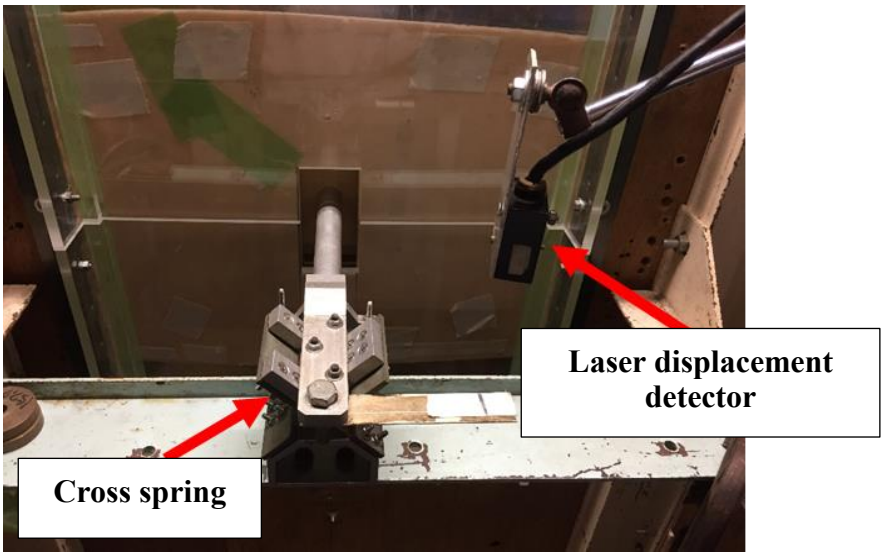

Figure 5.1.3 Suspension situation outside the wind tunnel

(4) Experimental conditions of spring-supported tests

Table 5.1.2 shows the experimental conditions for the spring-supported tests. The Scruton number $Sc=2I\delta/\rho D^4$ for each cross section was adjusted as close as possible. The gap length g between the model and the S.P. was adjusted as $g=0.10B$ and $0.31B$, by referring to previous wind tunnel tests[5), 7)].

Table 5.1.2 Experimental conditions for spring-supported tests

B/D	*B* (mm)	*D* (mm)	S.P.	Gap length *g*	Air density ρ (kg/m^3)	Moment of inertia per unit length *I* (kg·m^2/m)	Logarithmic decrement of structural damping δ (2ϕ=1°)	Natural frequency *f* (Hz)	*Sc*
2.0	360	180	w/o	-	1.22	0.039	0.0082	4.18	0.50
			w	0.10*B*	1.22	0.039	0.0081	4.18	0.50
			w	0.31*B*	1.21	0.039	0.0079	4.18	0.48
4.0	360	90	w/o	-	1.22	0.047	0.0136	4.84	16
			w	0.10*B*	1.21	0.049	0.0132	4.05	16
			w	0.31*B*	1.21	0.049	0.0129	4.04	16
6.0	540	90	w/o	-	1.23	0.092	0.0139	3.13	32
			w	0.10*B*	1.21	0.099	0.0128	2.84	32
			w	0.31*B*	1.21	0.099	0.0128	2.84	32

Model length: *L*=828mm

5.1.2 Flow Visualization Tests

(1) Wind tunnel

Flow visualization around a forced-oscillating model was conducted in a small-sized wind tunnel at Kyushu Institute of Technology. The small-sized wind tunnel is the same as the one demonstrated in chapter 3. The wind velocity *V* in the flow visualization tests was set as 0.8m/s which was good for visualization.

The Reynolds number in the flow visualization tests was $Re=VD/\nu=1.1\times10^3$, which is smaller than that in the spring-supported tests by approximately one order of magnitude. Nevertheless, according to the results of the measurements of the Strouhal numbers *St* in various Reynolds number range for a rectangular cross section with a side ratio of *B/D*=2.0, the Strouhal numbers in the Reynolds number range of $Re=1.1\times10^3$ and $Re=1.8\times10^3$-3.4×10^4 are *St*=0.08 and *St*=0.07, respectively[8]. A similar tendency is also confirmed for the cross section with a side ratio of *B/D*=4.0[9]. Hence, it can be considered that the influence of the difference in Reynolds number on the flow field is small. Therefore, it is reasonable to have qualitative discussion based on the results of spring-supported and flow visualization tests.

(2) Specifications of target models and splitter plate

The models used in flow visualization tests were made of transparent acrylic panels. All the models were painted in black while the central part of the models which were illuminated by a light source was transparent, for the sake of making the flow patterns around the model as bright as possible. An end plate was attached at the end of each model for the sake of ensuring that the flow around the model was two-dimensional. **Table 5.1.3** shows the size of the models. **Figure 5.1.4** shows the forced-oscillating model of *B/D*=2.0 inside the wind tunnel.

Table 5.1.3 Experimental conditions for flow visualization tests

Side ratio *B/D*	2.0	4.0	6.0
Along-wind length *B*(mm)	80	80	120
Cross-wind length *D*(mm)	40	20	60
Model length *L*(mm)	150		
Aspect ratio *L/D*	3.8	7.5	7.5

Figure 5.1.4 Forced-oscillating model of *B/D*=2.0 in the wind tunnel

The S.P. was also used and was set to the same configuration as the spring-supported tests. The along-wind length of the S.P. was 800mm for the model of *B/D*=2.0, 400mm for the models of *B/D*=4.0, 6.0. The width and thickness of the S.P. were 400mm and 3mm, respectively. **Figure 5.1.5** shows the setting situation of the

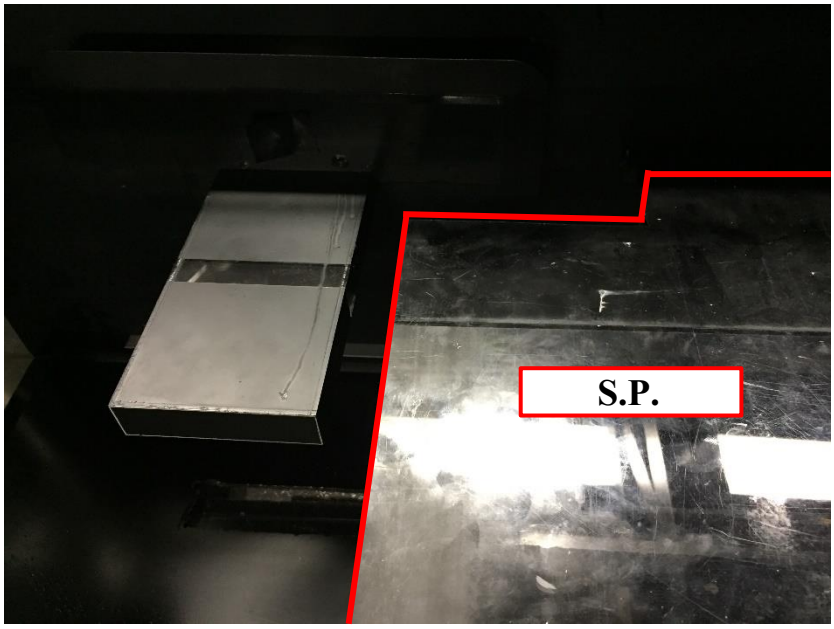

Figure 5.1.5 Setting situation of the S.P. inside the wind tunnel

S.P. inside the small-sized wind tunnel.

(3) Measurement system

Flow visualization around a forced-oscillating model were conducted by the smoke wire method. The models were suspended in the wind tunnel by a cross spring in a single torsional mode. The forced-oscillating frequency and amplitude were adjusted by a digital function signal and an amplifier, respectively. **Figure. 5.1.6** and **Figure. 5.1.7** show the schematic illustration and the setting situation of the forced oscillation system, respectively. The flow patterns around the model were

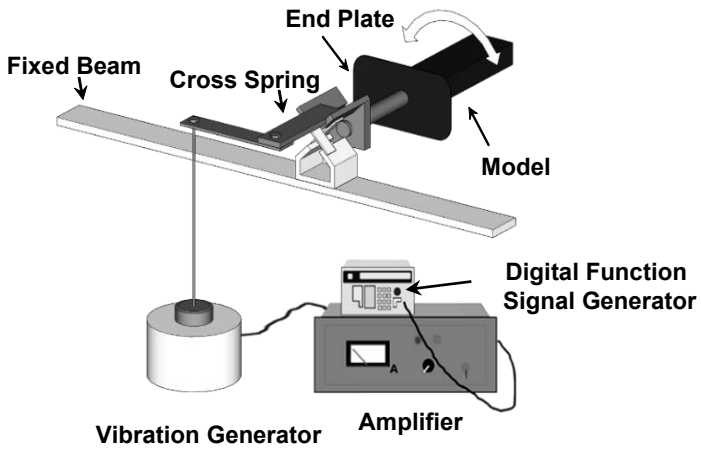

Figure. 5.1.6 Schematic illustration of the forced oscillation system

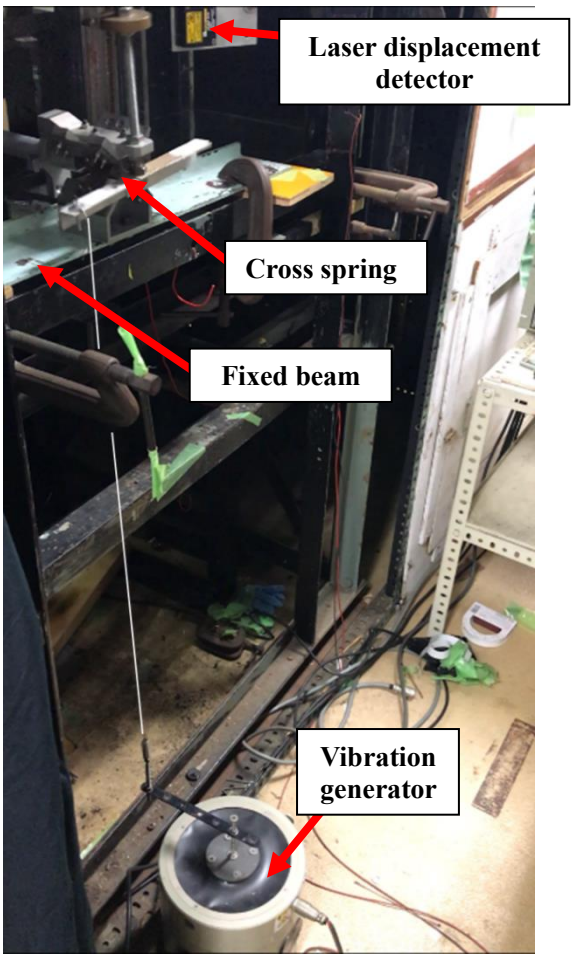

Figure. 5.1.7 Setting situation of the forced oscillation system

photographed with a high-speed camera. In each forced-oscillating amplitude, the models were photographed for ten periods of vibration. The photographed pictures were processed with the Motion Studio X64 software in a computer.

(4) Experimental conditions of flow visualization tests

Table 5.1.4 shows the experimental conditions of flow visualization tests. Based on the results obtained from the spring-supported tests, at the onset wind velocity of the motion-induced vortex vibration for each cross section, the forced-oscillating double amplitude was set as 2ϕ was set as 0.3°-10° (0.3°, 0.6°, 1°, 2°, 3°…) for the sake of verifying the relation between the secondary vortex at trailing edge and the generation of the motion-induced vortex vibration. On the other hand, at the wind velocity where the maximum response amplitude of the motion-induced vortex vibration occurred, the forced-oscillating double amplitude 2ϕ was set as constant in order to observe the effect of the secondary vortex at trailing edge on the motion-induced vortex vibration at peak response amplitude.

Table 5.1.4 Experimental conditions for flow visualization tests

B/D	*B* (mm)	*D* (mm)	S.P.	Gap length *g*	Wind velocity *V* (m/s)	Forced-oscillating frequency *f* (Hz)	Reduced wind velocity $V_r=V/fD$	Forced-oscillating double amplitude 2ϕ
2.0	80	40	w/o	-	0.8	7.7	2.6	0.3°-10°
			w/o	-	0.8	7.1	2.8	1°
			w	0.10*B*	0.8	7.1	2.8	1°
			w	0.31*B*	0.8	7.1	2.8	1°
4.0	80	20	w/o	-	0.8	8.9	4.5	0.3°-10°
			w/o	-	0.8	7.7	5.2	2°
			w	0.10*B*	0.8	7.7	5.2	2°
			w	0.31*B*	0.8	7.7	5.2	2°
6.0	120	20	w/o	-	0.8	6.5	6.2	0.3°-10°
			w/o	-	0.8	5.9	6.8	1°
			w	0.10*B*	0.8	5.9	6.8	1°
			w	0.31*B*	0.8	5.9	6.8	1°

Model length: *L*=150mm

5.2 Response Characteristics of Rectangular Cylinders of *B/D* = 2, 4, 6 in a Torsional Mode

(1) *B/D*=2.0

Figure 5.2.1 shows the results of the spring-supported tests for the rectangular cross with a side ratio of *B/D*=2.0 with and without the S.P. in the torsional mode. **Figure 5.2.2** shows the enlarge view of the wind velocity region of the motion-induced vortex vibration. Regardless of the presence or absence of the S.P., the vortex-induced vibrations were confirmed as occurring from approximately V_r=2.5. These vortex-induced vibrations are considered to be the motion-induced vortex vibrations, because the onset wind velocities of these vortex-induced vibrations approximately coincide with V_{cr}=2/3×1.67*B/D*=2.2. This result has a similar tendency as in the previous research[2]. In addition, in chapter 4, the results of spring-supported tests of *B/D*=2.0 in the heaving mode has revealed that the presence of S.P. and its gap length *g* have an influence on the maximum response amplitude of the motion-induced vortex vibration. However, this phenomenon was not observed in the torsional mode. It was confirmed that the maximum amplitude of the motion-induced vortex vibration remains at nearly the same value regardless of the presence of S.P. and its gap length *g*. With regard to this phenomenon, further discussion will be carried out in the results of flow

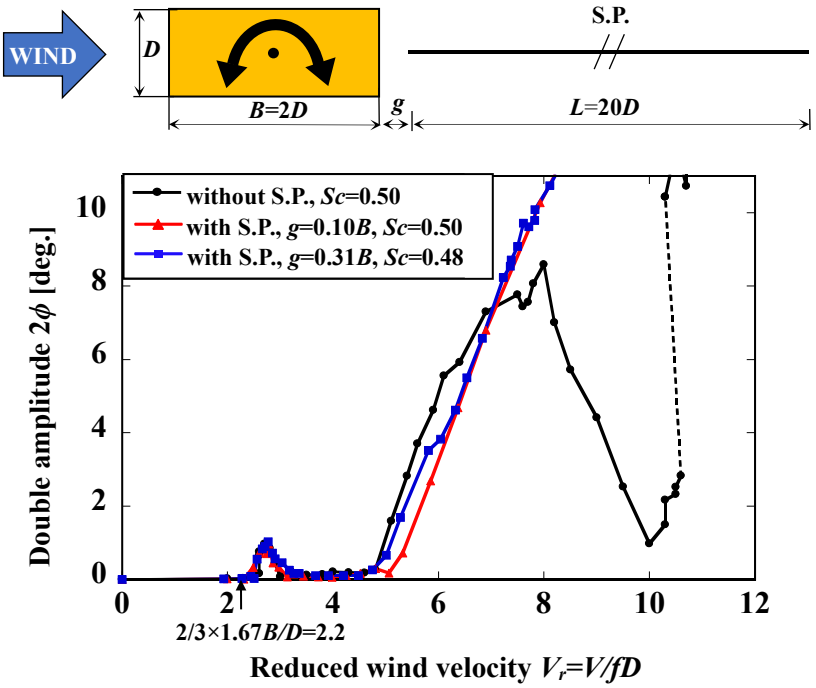

Figure 5.2.1 *V-A* diagram of *B/D*=2.0 in the torsional mode

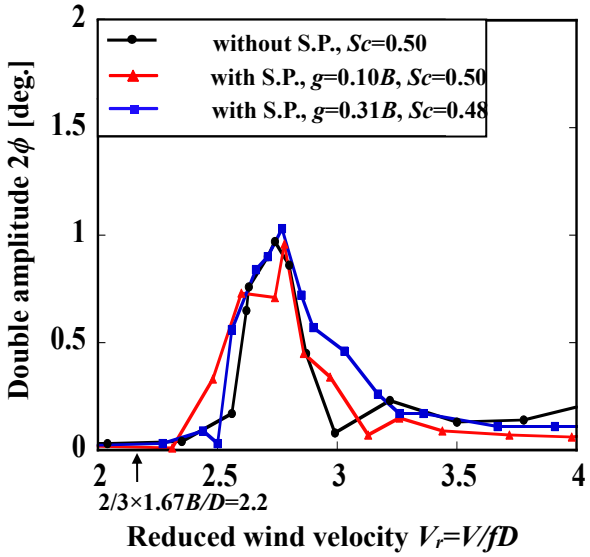

Figure 5.2.2 *V-A* diagram of *B/D*=2.0 in the torsional mode (Enlarge view of the wind velocity region of the motion-induced vibration)

visualization tests.

The low-speed torsional flutter was confirmed to occur from V_r=5 approximately in all three cases with and without S.P. The response amplitude of the case without S.P. began to decease at V_r=8 and the occurrence of the torsional flutter was confirmed from V_r=11 approximately. However, in the two cases when the S.P. was installed at g=0.10B and g=0.31B, the response amplitude increased continuously and changed to

the torsional flutter along with the increase in wind velocity. The discrepancy of response characteristics observed at the vicinity of V_r=8 can be attributed to the interference effect between the separated vortex from leading edge and the Kármán vortex. On one hand, it is deemed that the separated vortex from the leading edge which plays a role in triggering the low-speed flutter can be produced only at a low reduced wind velocity region[7]. On the other hand, it is suggested that the wind velocity region where separated vortex from the leading edge can be produced will expand when Kármán vortex is suppressed due to the installation of the S.P[10]. Therefore, it can be understood that in the case when the S.P. was not installed, the low-speed flutter occurred due to the existence of the separated vortex from leading edge at V_r=5, as the wind velocity increased, the generation of the separated vortex from leading edge was obstructed by the Kármán vortex gradually, thus, the response amplitude of the low-speed flutter began to decrease at V_r=8 in a consequence. In the two cases when the S.P. was installed at g=0.10B and g=0.31B, the generation of the separated vortex from leading edge was no longer influenced by the Kármán vortex. As a result, the response amplitude of the low-speed flutter increased continuously and changed to the torsional flutter along with the increase in wind velocity eventually.

(2) *B/D*=4.0

The results of the spring-supported tests of B/D=4.0 in the torsional mode are shown in **Figure 5.2.3**. The onset wind velocities of vortex-induced vibrations were confirmed at V_r=4 which corresponds to V_{cr}=2/3×1.67B/D=4.4, so that these vortex-induced vibrations were considered to be motion-induced vortex vibrations. When the S.P. was installed at g=0.10B, the maximum response amplitude of the motion-induced vortex vibration became smaller. This result has a similar tendency as in the previous research[7]. However, when the S.P. was installed at g=0.31B, the maximum response amplitude became slightly larger.

In the cases when the S.P. was installed at g=0.10B and 0.31B, the torsional flutter was confirmed as occurring at a lower reduced wind velocity. The smaller the gap length g was, the lower the onset wind velocity of the torsional flutter tended to be. This result can be explained in a way that the Kármán vortex was weakened then the separated vortex from leading edge, which is produced inside the local separation bubble was elicited due to the installation of S.P. As a result, the onset wind velocity of the torsional flutter became lower. This tendency also corresponds to the result of

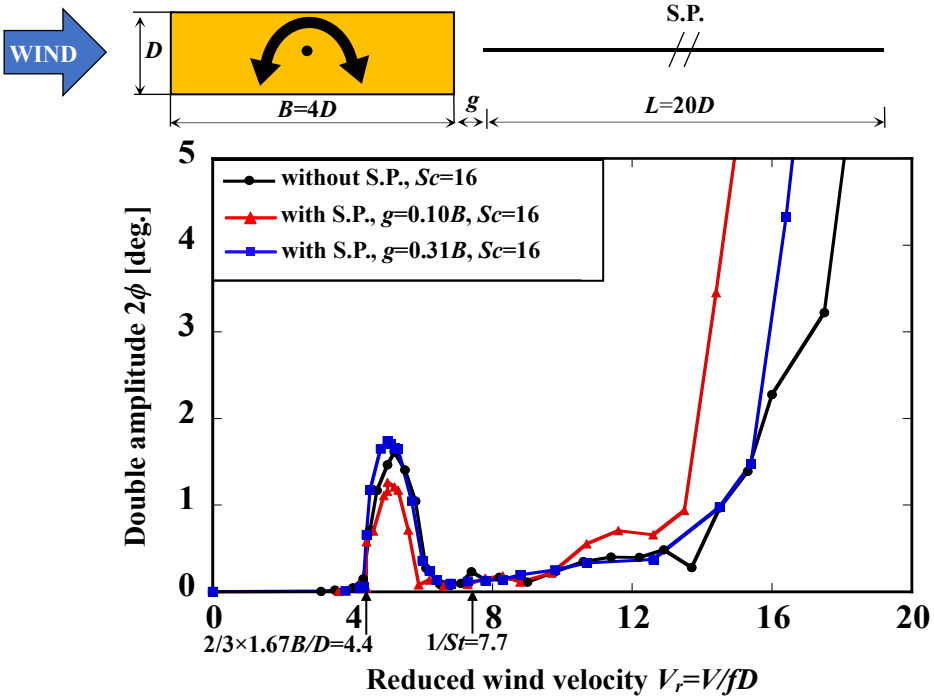

Figure 5.2.3 *V-A* diagram of *B/D*=4.0 in the torsional mode

previous research[7].

(3) *B/D*=6.0

The results of the spring-supported tests of *B/D*=6.0 in the torsional mode are shown in **Figure 5.2.4**. **Figure 5.2.5** shows the enlarge view of the wind velocity region of the motion-induced vortex vibration. The motion-induced vortex vibrations were confirmed occurring at V_r=6 approximately. These vortex-induced vibrations are considered to be the motion-induced vortex vibrations. Because the onset wind velocities of these vortex-induced vibrations correspond to the empirical value of the onset wind velocity of the motion-induced vortex vibration V_{cr}= 2/3×1.67*B/D*=6.7, Similarly as the results of *B/D*=4.0, when the S.P. was installed at *g*=0.10*B*, the wind velocity region of the motion-induced vortex vibration became narrower while it became wider when the S.P. was installed at *g*=0.31*B*. The relation between the onset wind velocity of the torsional flutter and the gap length *g* was also similar to the results of *B/D*=4.0. The smaller the gap length *g* was, the lower the onset wind velocity of torsional flutter tended to be.

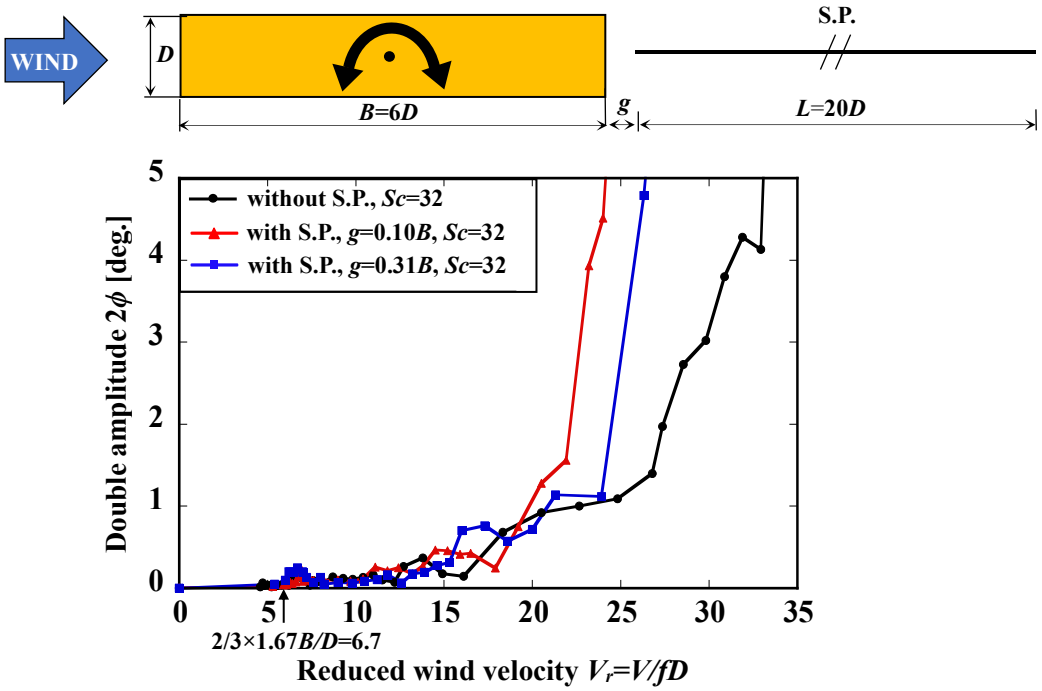

Figure 5.2.4 *V-A* diagram of *B/D*=6.0 in the torsional mode

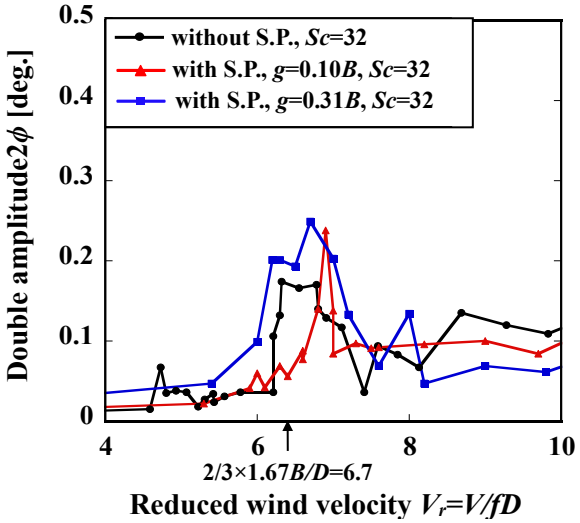

Figure 5.2.5 *V-A* diagram of *B/D*=6.0 in the torsional mode (Enlarge view of the wind velocity region of the motion-induced vibration)

5.3 Necessity of Secondary Vortex at Trailing Edge for the Onset of Motion-induced Vortex Vibration for Rectangular Cylinders of *B/D*=2, 4, 6 in a Torsional Mode

At the onset reduced wind velocity of the motion-induced vortex vibration, each model was photographed for ten periods of vibration when it was forced-oscillated at the onset reduced wind velocity of motion-induced vortex vibration. In one period of vibration, there will be up to two secondary vortices at trailing edge generated. Thus, in ten periods of vibration, there will be up to twenty secondary vortices at trailing edge generated. Therefore, the generation probability of the secondary vortex at trailing edge is defined as (the number of the secondary vortex at trailing edge/20) ×100(%). This was used as an index showing the extent of the stability of the secondary vortex at trailing edge. Although the stable formation of the secondary vortex at trailing edge was identified by eye recognition, the generation probability of the secondary vortex at trailing edge was measured by four experimenters. As a result, the generation probabilities of the secondary vortex at trailing edge measured by different experimenters did not show significant differences. Therefore, it is reasonable to evaluate the extent of the stability of the secondary vortex at trailing edge by using the generation probability of the secondary vortex at trailing edge. The results of the generation probability of the secondary vortex at trailing shown in the below were selected from one of the results obtained by all the experimenters.

Figure 5.3.1(a)-Figure 5.3.3(a) show the relation between the generation probability of the secondary vortex at trailing edge and forced-oscillating amplitude at the onset reduced wind velocity of motion-induced vortex vibration in the torsional mode for *B/D*=2.0, 4.0, 6.0. **Figure 5.3.1(b)-Figure5.3.3(b)** show the photographs of flow visualization tests taken in a higher and a lower amplitude. A red dotted rectangle was added at the rear corner in the bottom surface in order to recognize whether or not the secondary vortex at trailing edge is generated. **Figure 5.3.1(c)-Figure 5.3.3(c)** show the *V-A* diagrams in the wind velocity region of the motion-induced vortex vibration.

On one hand, in each cross section, the separated vortex from leading edge was observed regardless of the forced-oscillating amplitude. On the other hand, by comparing the generation probability of the secondary vortex at trailing edge with the

forced-oscillating amplitude, it was confirmed that the generation probabilities reached 100% only in extremely high forced-oscillating amplitudes, which far exceeded the response amplitude of motion-induced vortex vibrations. For example, in the case of B/D=2.0 as shown in **Figure 5.3.1**, the generation probability of the secondary vortex at trailing edge reached 100% in the amplitude of 2ϕ=10° at a reduced wind velocity of V_r=2.6. The unification of secondary vortex at trailing edge and separated vortex from leading edge was also observed. This result corresponds to the previous wind tunnel test[1]. However, the secondary vortex at trailing edge was not observed in amplitudes smaller than 2ϕ=0.6°. In other words, the motion-induced vortex vibration occurred while there was almost no secondary vortex at trailing edge

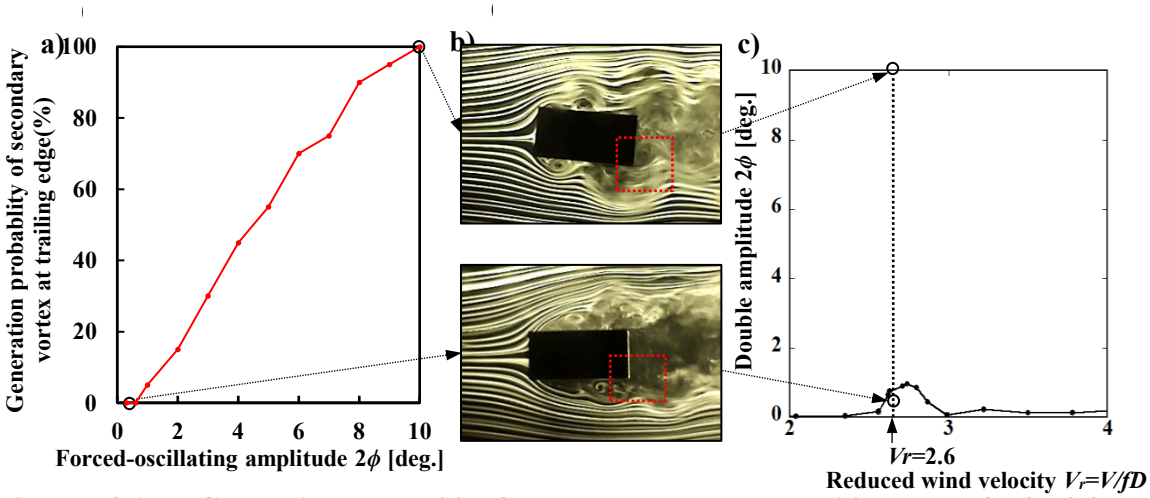

Figure 5.3.1 (a) Generation probability for secondary vortex at trailing edge of B/D=2.0 at V_r=2.6, (b) flow visualization result of B/D=2.0 at the maximum displacement in clockwise direction and (c) V-A diagram of B/D=2.0 (without S.P., Sc=0.50)

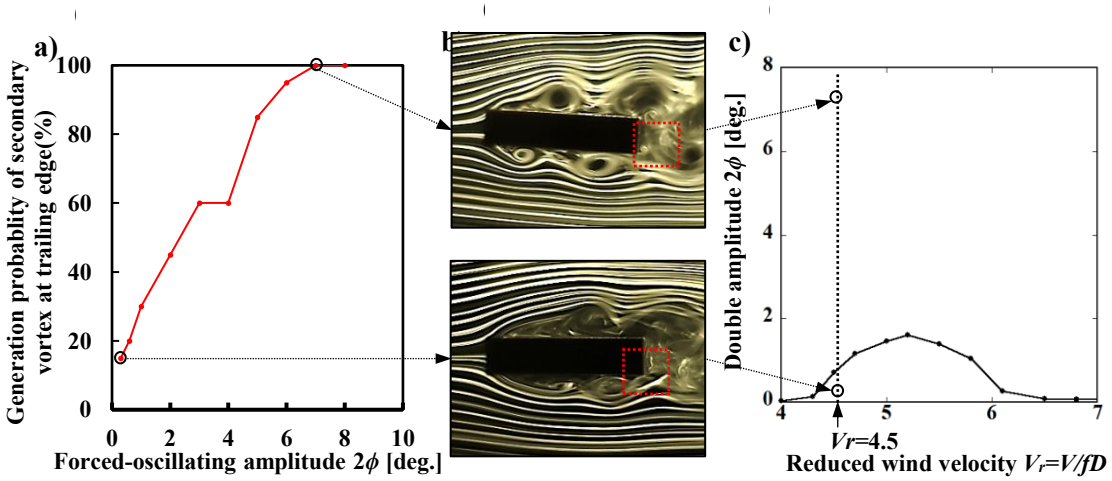

Figure 5.3.2 (a) Generation probability for secondary vortex at trailing edge of B/D=4.0 at V_r=4.5, (b) flow visualization result of B/D=4.0 at the maximum displacement in clockwise direction and (c) V-A diagram of B/D=4.0 (without S.P., Sc=16)

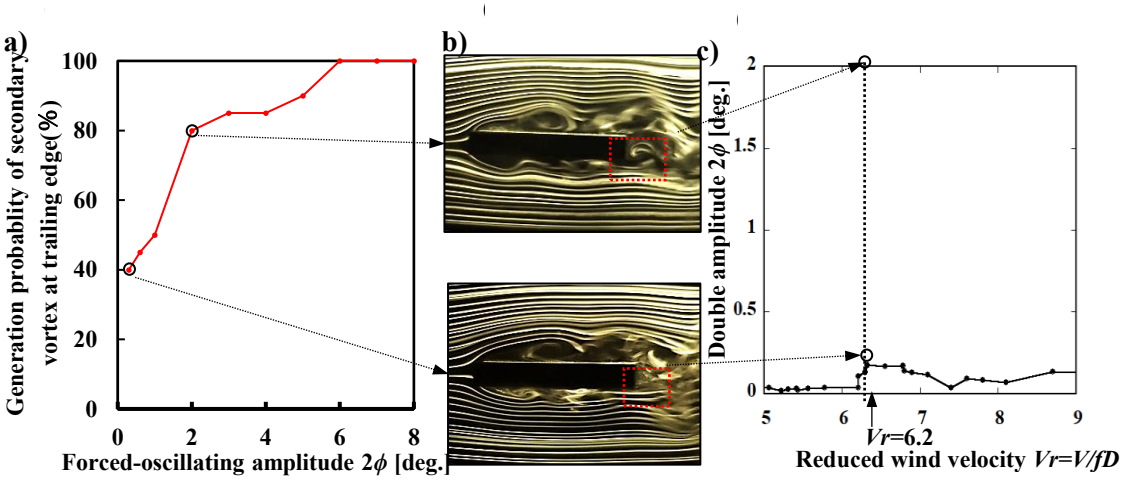

Figure 5.3.3 (a) Generation probability for secondary vortex at trailing edge of *B/D*=6.0 at V_r=6.2, (b) flow visualization result of *B/D*=6.0 at the maximum displacement in clockwise direction and (c) *V-A* diagram of *B/D*=6.0 (without S.P., *Sc*=32)

produced. A similar tendency was also confirmed in the cases of *B/D*=4.0, 6.0 as shown in **Figure 5.3.2** and **Figure 5.3.3**. At the onset reduced wind velocity of the motion-induced vortex vibration, in a lower forced-oscillating amplitude range, the generation probability of the secondary vortex at trailing edge was very low. This result indicates that the shedding of the secondary vortex at trailing edge is very unstable in low amplitudes, the motion-induced vortex vibration can occur without the stable shedding of the secondary vortex at trailing edge. Therefore, it is suggested that the stable shedding of secondary vortex at trailing edge is not a necessary condition for the generation of the motion-induced vortex vibration in the torsional mode, regarding rectangular cross sections with side ratios of *B/D*=2.0, 4.0, 6.0.

5.4 The Effect of Secondary Vortex at Trailing Edge on Motion-induced Vortex Vibration at Peak Response for Rectangular Cylinders of *B/D*＝2, 4, 6 in a Torsional Mode

(1) *B/D*=2.0

It is known that the separated vortex from leading edge merges with the secondary vortex at trailing edge at the maximum and minimum displacement in a period of vibration[11]. In order to get a better understanding on the effect of the secondary vortex at trailing edge on the motion-induced vortex vibration, the main attention is concentrated on the flow patterns at the maximum and minimum displacement. **Figure 5.4.1-Figure 5.4.3** show the results of flow visualization tests with and without the

S.P. in the torsional mode for B/D=2.0 at the vicinity of the maximum and minimum displacement at V_r=2.8 where the maximum response amplitude of the motion-induced vortex vibration occurred. A red dotted rectangle was added at the rear corner in order to confirm the effect of secondary vortex at trailing edge on the flow field characteristics. It should be noted that the shape and brightness of the separated vortices from leading edge formed by the white smoke are affected strongly by the

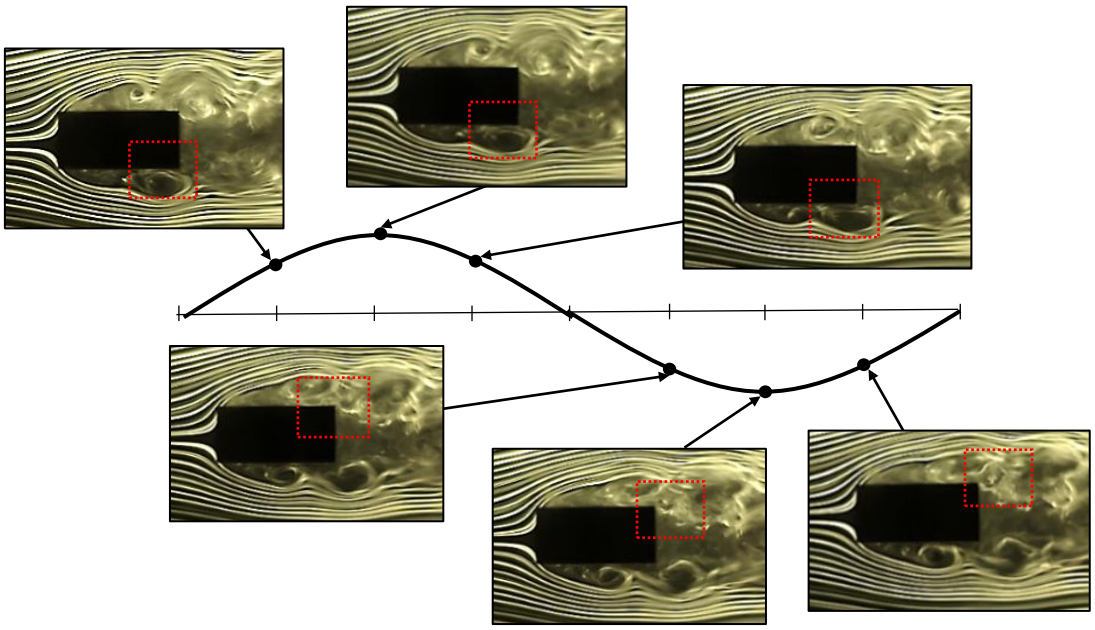

Figure 5.4.1 Results of Flow visualization tests for B/D=2.0 without S.P. in 2ϕ=1° at Vr=2.8

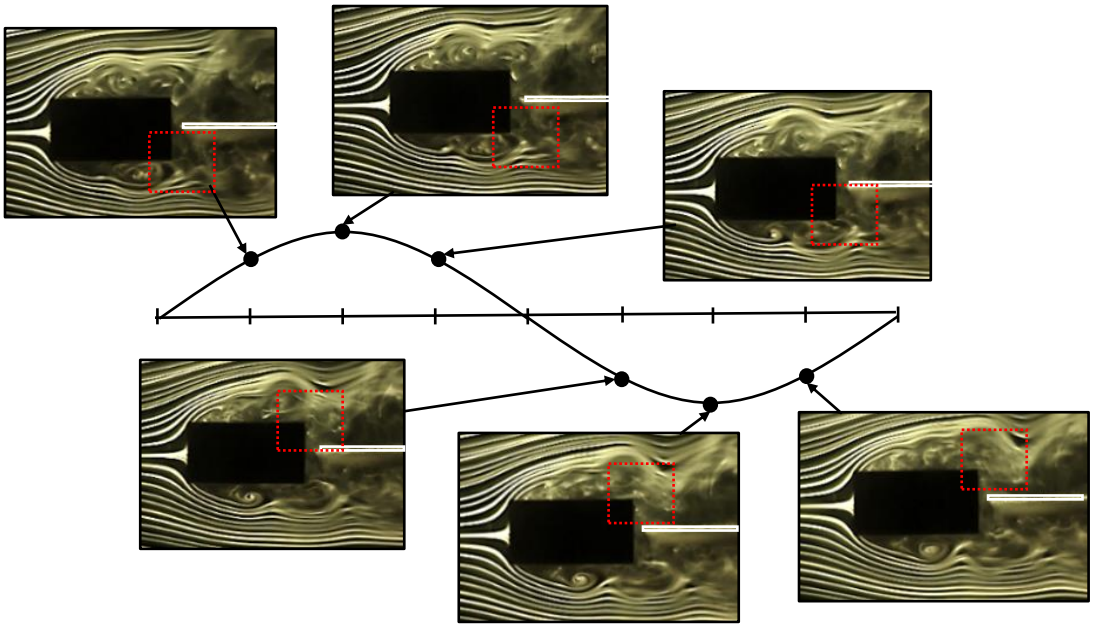

Figure 5.4.2 Results of Flow visualization tests for B/D=2.0 with S.P. (g=0.10B). in 2ϕ=1° at Vr=2.8

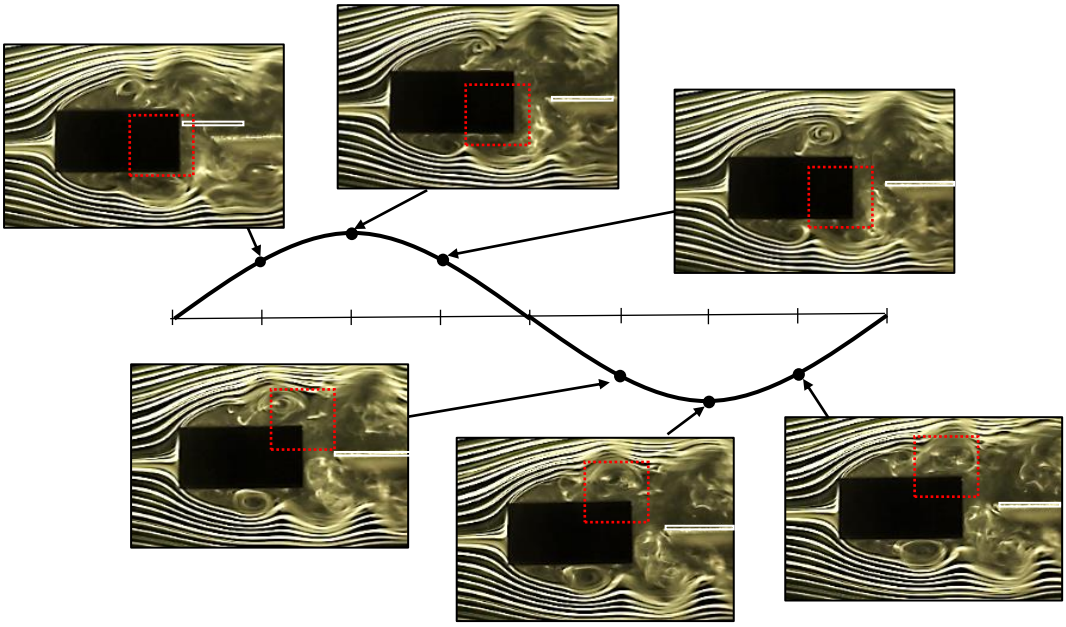

Figure 5.4.3 Results of Flow visualization tests for *B/D*=2.0 with S.P. (*g*=0.31*B*). in 2ϕ=1° at *Vr*=2.8

relative positional relation between the approaching white smoke and the model. Besides, the approaching white smoke is not axisymmetric with respect to the horizonal central line of the model. Hence, the shape and brightness of the separated vortices from leading edge on a surface of the model in a phase and those on the other surface in the opposite phase are not exactly the same. Despite these differences, the flow distributed on the upper and lower sides of the model can be considered to be axisymmetric with respect to the horizonal central line of the model, based on the fact that the locations of the centers of the separated vortices from leading edge in a phase and those in the opposite phase are point symmetric with respect to the center of the model.

The flow field around the model was similar in all three cases with and without S.P. The existence of the secondary vortex at trailing edge and its unification with the separated vortex from leading edge was not confirmed. Not only that, but also the results of the spring-supported tests of *B/D*=2.0 in the torsional mode shown in **Figure 5.2.2** has indicated that the installation of the S.P. has hardly any influence on the maximum response amplitude of the motion-induced vortex vibration. Combining the two results mentioned above, it is considered that the reason why the installation of S.P. has no influence on the response amplitude in the torsional mode can be explained in a way that the influence caused by the installation of the S.P. on the flow field was

small, because the secondary vortex at trailing edge was barely produced. For this reason, regarding the effect of the secondary vortex at trailing edge on the motion-induced vortex vibration for the rectangular cross section with the side ratio of B/D=2.0 in the torsional mode at peak response amplitude, further investigation is needed. This is a subject for future analysis.

(2) *B/D*=4.0

Figure 5.4.4-Figure 5.4.6 show the results of flow visualization tests with and without S.P. in the torsional mode for B/D=4.0 at the vicinity of the maximum and minimum displacement at V_r=5.2 where the maximum response amplitude of the motion-induced vortex vibration occurred. In the case when the S.P. was installed at g=0.10B, the entrainment of the integrated vortex composed of the separated vortex from leading edge and the secondary vortex at trailing edge was inhibited due to the installation of S.P. in comparison with the case without S.P., as shown in **Figure 5.4.4** and **Figure 5.4.5**. In addition, according to the result of unsteady aerodynamic moment distribution of B/D=4.0 in the wind velocity region of the motion-induced vortex vibration in the torsional mode, the unsteady aerodynamic moment acting on the windward side of the model provides damping moment to the model, whereas it provides exciting moment to the model on the leeward side[6]. Thus, it is suggested that the intensity of the integrated vortex has significant influence on the magnitude of the exciting moment acting on the model. Therefore, it can be considered that the reduction in the maximum response amplitude was due to the inhibition of the integrated vortex

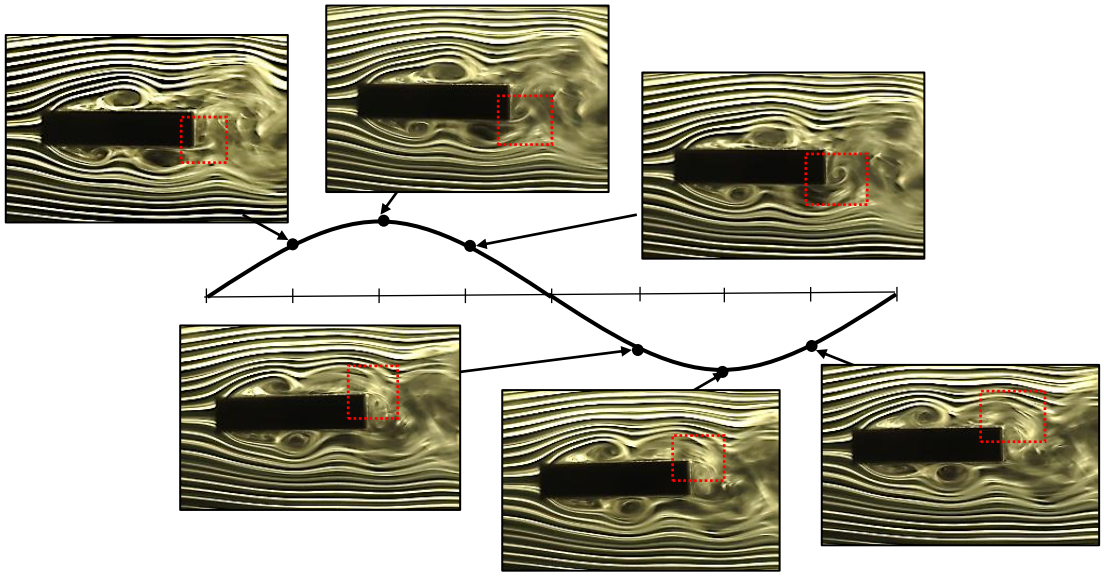

Figure 5.4.4 Results of flow visualization tests of *B/D*=4.0 without S.P. in 2ϕ=2° at *Vr*=5.2

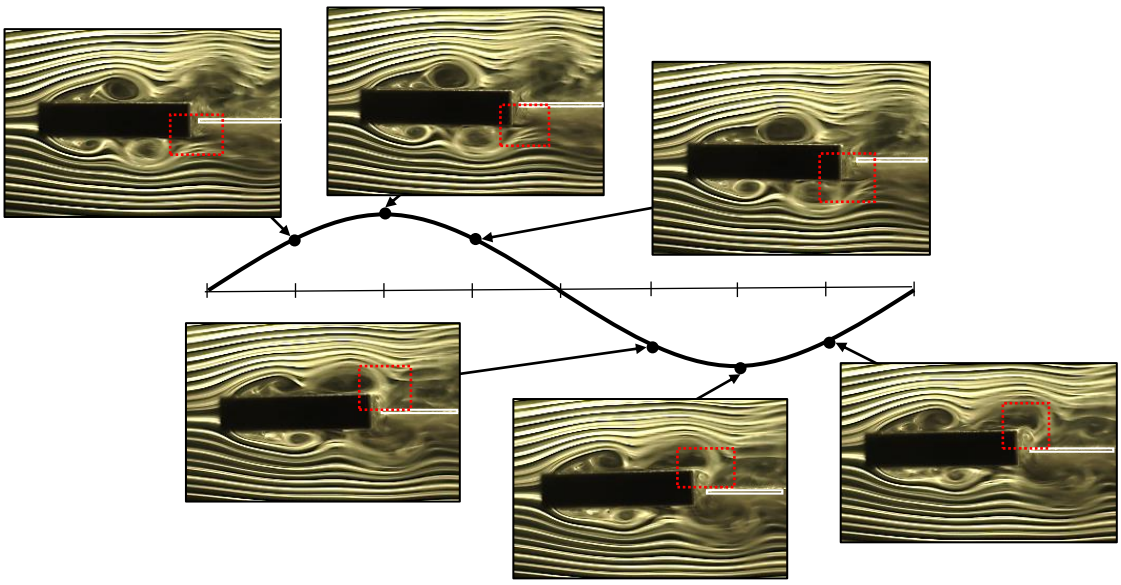

Figure 5.4.5 Results of flow visualization tests of *B/D*=4.0 with S.P. (*g*=0.10*B*) in 2ϕ=2° at V_r=5.2

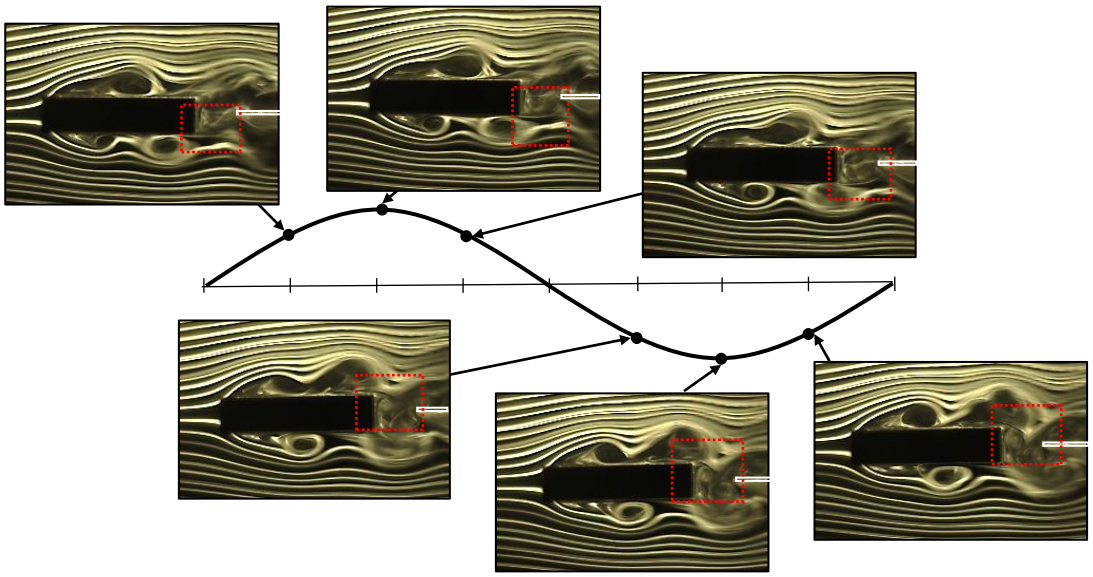

Figure 5.4.6 Results of flow visualization tests of *B/D*=4.0 with S.P. (*g*=0.31*B*) in 2ϕ=2° at V_r=5.2

consisting of the separated vortex from leading edge and the secondary vortex at trailing edge. In other words, the secondary vortex at trailing edge can be relevant to the magnitude of the exciting moment in terms of affecting the intensity of the integrated vortex at the peak response amplitude of the motion-induced vortex vibration for *B/D*=4.0 in the torsional mode.

In the case when the S.P. was installed at *g*=0.31*B*, regarding the entrainment of the integrated vortex composed of the separated vortex from leading edge and the

secondary vortex at trailing edge, there was no apparent difference between the case when the S.P. was installed at g=0.31B and the case when the S.P. was not installed, as shown in **Figure 5.4.4** and **Figure 5.4.6**. However, in chapter 4, the results of flow visualization tests of B/D=4.0 in the heaving mode have indicated that when the S.P. was installed at g=0.31B, the intensity of the integrated vortex of the separated vortex from the leading edge and the secondary vortex at trailing edge tended to become stronger due to the suppression of the Kármán vortex. Moreover, by contrasting the results of spring-supported tests of B/D=4.0 in the torsional mode with the results of spring-supported tests of B/D=4.0 in the heaving mode, when the S.P. was installed at g=0.31B, it was confirmed that the maximum response amplitude of the motion-induced vortex vibration slightly increased in the torsional mode while it increased remarkably in the heaving mode.

On one hand, the maximum response amplitude of the motion-induced vortex vibration in the torsional mode for the model of B/D=4.0 was confirmed at V_r=5.2, as shown in **Figure 5.2.3**. It separates away from the resonance reduced wind velocity of the Kármán vortex-induced vibration, which is 1/St=7.7 (St=0.13) referred from a previous wind tunnel test[9]. On the other hand, as demonstrated in chapter 4, the results of spring-supported tests of B/D=4.0 in the heaving mode have indicated that the maximum response amplitude of the motion-induced vortex vibration in the heaving mode occurred at V_r=8.3, which is close to the resonance reduced wind velocity of the Kármán vortex-induced vibration. Thus, it can be considered that the influence of the Kármán vortex on the motion-induced vortex vibration in the torsional mode is smaller than that in the heaving mode. Therefore, it can be suggested that when the S.P. was installed at g=0.31B, not only the Kármán vortex was weakened, but also the intensity of the integrated vortex composed of the separated vortex from leading edge and the secondary vortex at trailing edge was elicited. Therefore, the intensity of integrated vortex composed of the separated vortex from leading edge and the secondary vortex at trailing edge is considered to be stronger, although the degree of the enhancement of the integrated vortex in the torsional mode is not as distinct as that in the heaving mode. As a consequence, the exciting moment acting on the model is suggested to increase slightly in the torsional mode. Correspondingly, when the S.P. was installed at g=0.31B, the increment of the maximum response amplitude in the torsional mode is also much smaller than that in the heaving mode.

(3) *B/D*=6.0

Figure 5.4.7- Figure 5.4.9 show the results of the flow visualization tests in the torsional mode of *B/D*=6.0 with and without the S.P. at the vicinity of the maximum and minimum displacement at V_r=6.8 where the maximum amplitude of the motion-induced vortex vibration occurred. By comparing the case when the S.P. was not installed with the cases when the S.P. was installed at g=0.10B and g=0.31B, it can be observed that the generation patterns of the secondary vortex at trailing edge in all three cases have the same tendency as those in the case of *B/D*=4.0 in the torsional mode. When the S.P. was installed at g=0.10B, the integrated vortex composed of the separated vortex from leading edge and the secondary vortex at trailing edge was

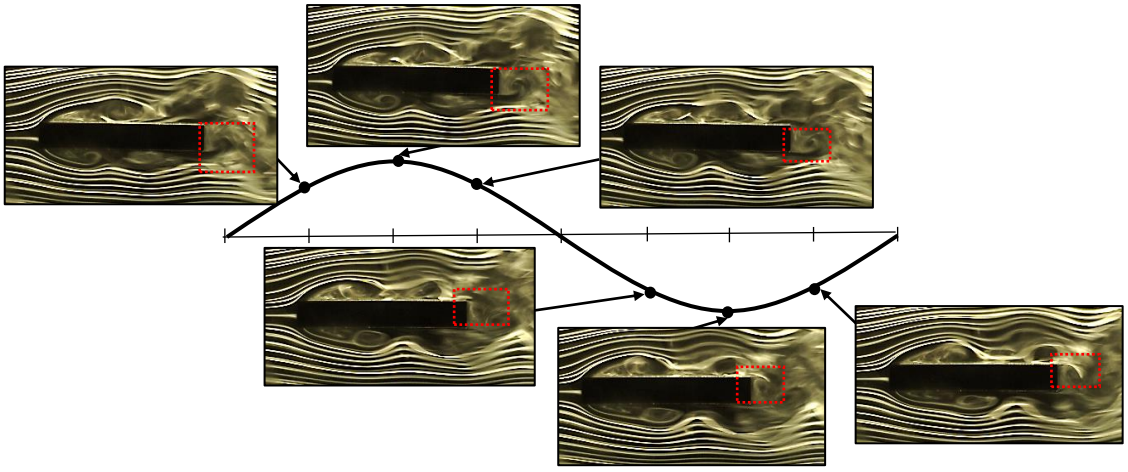

Figure 5.4.7 Results of flow visualization tests of *B/D*=6.0 without S.P. in 2ϕ=1° at V_r=6.8

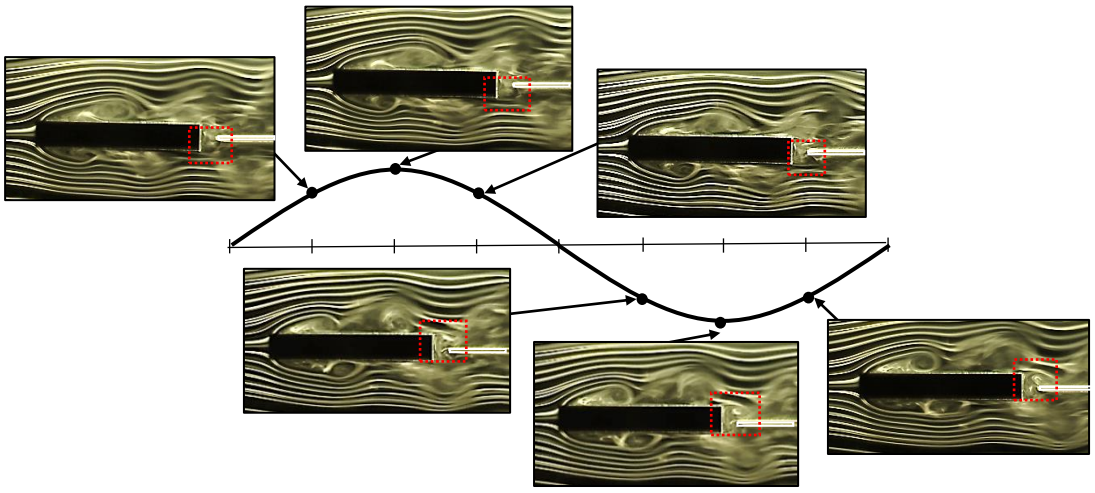

Figure 5.4.8 Results of flow visualization tests of *B/D*=6.0 with S.P. (g=0.10B) in 2ϕ=1° at V_r=6.8

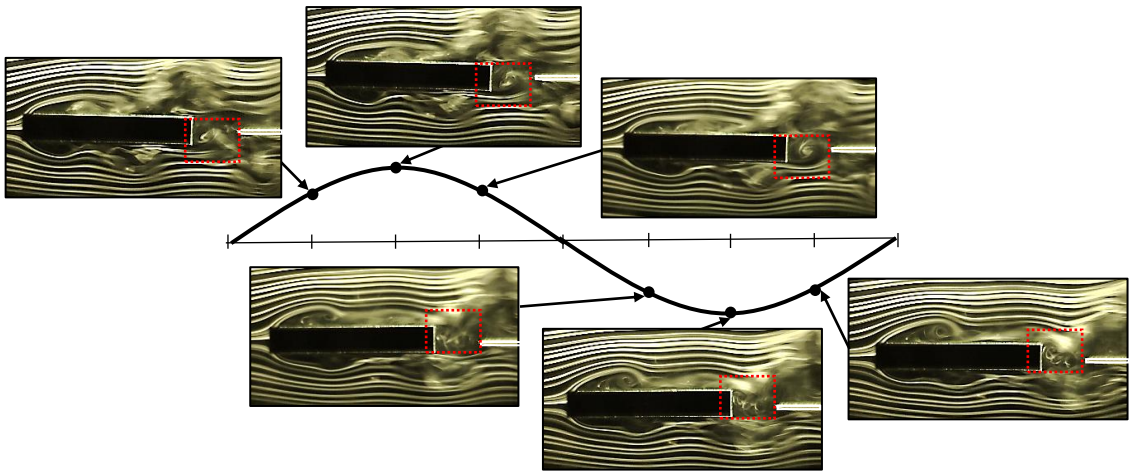

Figure 5.4.9 Results of flow visualization tests of *B/D*=6 with S.P. (*g*=0.31*B*) in 2ϕ=1° at V_r=6.8

inhibited due to the installation of the S.P. Thus, it is suggested that the decrease of the exciting moment of the motion-induced vortex vibration for *B/D*=6.0 was also attributed to the inhibition of the integrated vortex consisting of the separated vortex from leading edge and the secondary vortex at trailing edge. In other words, the secondary vortex at trailing edge can be relevant to the magnitude of the exciting moment of the motion-induced vortex vibration for *B/D*=6.0 in the torsional mode, just the same as in the case of *B/D*=4.0. When the S.P. was installed at *g*=0.31*B*, there seemed to be no apparent difference comparing with the case when the S.P. was not installed, in terms of the entrainment of the integrated vortex. This also can be explained in a way that the intensity of the integrated vortex is considered to become stronger due to the suppression of the Kármán vortex, although the degree of the enhancement of the integrated vortex in the torsional mode is not as distinct as it is in the heaving mode.

5.5 Summary

This chapter focuses on the effect of the secondary vortex at trailing edge on the motion-induced vortex in the torsional mode, with respect to the rectangular cross sections with side ratios of *B/D*=2.0-8.0 where the motion-induced vortex vibration is considered to occur. The results of spring-supported and flow visualization tests in the torsional mode for rectangular cross sections with side ratios of *B/D*=2.0, 4.0, 6.0 are introduced. The response characteristic of rectangular cross sections with side ratios *B/D*=2.0, 4.0, 6.0 in the torsional mode are confirmed. Subsequently, at the onset wind

velocity of the motion-induced vortex vibration, the necessity of the secondary vortex at trailing edge for the motion-induced vortex vibration in the torsional mode for rectangular cross sections with side ratios of B/D=2.0, 4.0, 6.0 are investigated. Furthermore, the effect of the secondary vortex at trailing edge on the response characteristics of the motion-induced vortex vibration at peak response amplitude is discussed. As a consequence, following conclusions have been drawn:

1. In the torsional mode, at the onset wind velocity of the motion-induced vortex vibration, the stable shedding of the secondary vortex at trailing edge is not a necessary condition for the generation of motion-induced vortex vibration for rectangular cross sections with side ratios of B/D=2.0, 4.0, 6.0, just as the same as the results obtained in the heaving mode.

2. On the other hand, at the peak response amplitude of the motion-induced vortex vibration, similar to the results obtained in the heaving mode, the secondary vortex at trailing edge can be relevant to the magnitude of the exciting moment acting on the model in terms of affecting the intensity of the integrated vortex consisting of the separated vortex from leading edge and the secondary vortex at trailing edge for rectangular cross sections with side ratios of B/D=2.0, 4.0, 6.0 in the torsional mode.

3. In the torsional mode, the installation of the S.P. has hardly any influence on the maximum response amplitude of the motion-induced vortex vibration for the rectangular cross section with a side ratio of B/D=2.0, although it influences the maximum response amplitude in the heaving mode. Regarding rectangular cross sections with side ratios of B/D=4.0, 6.0, at the peak response amplitude of the motion-induced vortex vibration, when the S.P. is installed at g=0.10B, the decline of the maximum response amplitude is confirmed, as the same as the results in the heaving mode. However, when the S.P. is installed at g=0.31B, the increment of the maximum response amplitude of the motion-induced vortex vibration in the torsional mode is not as large as that in the heaving mode, because the wind velocity region of the motion-induced vortex vibration in the torsional mode separates from the resonance wind velocity region of the Kármán vortex-induced vibration, compared with the one in the heaving mode. It is considered that the influence of the Kármán vortex on the separated vortex from leading edge and the secondary vortex at trailing edge in the torsional mode is smaller than that in the

heaving mode.

4. Regarding the rectangular cross section with the side ratio of B/D=2.0, the results obtained from the flow visualization tests in the torsional mode indicates that the secondary vortex at trailing edge and its unification with the separated vortex from leading edge is not confirmed. The flow field around the model is not influenced by installation of the S.P. Whereas in the heaving mode, the flow pattern of the integrated vortex composed of the separated vortex from leading edge and the secondary vortex at trailing is strongly influenced by the presence of the S.P. For the rectangular cross sections with the side ratios of B/D=4.0, 6.0, when the S.P. is installed at g=0.10B, the development of the integrated vortex composed of the separated vortex from leading edge and the secondary vortex at trailing edge is in the torsional mode, as the same as the results in the heaving mode. Nevertheless, when the S.P. is installed at g=0.31B, the degree of the enhancement of the integrated vortex composed of the separated vortex from leading edge and the secondary vortex at trailing edge in the torsional mode is not as distinct as that in the heaving mode. It can be explained the influence of the Kármán vortex on the separated vortex from leading edge and the secondary vortex at trailing edge in the torsional mode is smaller than that in the heaving mode.

References

1) Shiraishi, N. and Matsumoto, M., 1983. On classification of vortex-induced oscillation and its application for bridge structures, Journal of Wind Engineering and Industrial Aerodynamics, 14 (1-3), 419-430.
2) Shiraishi, N. and Matsumoto, M., 1982. On vortex-induced oscillations of bluff cross sections used for bridge structures, Proceedings of the Japan Society of Civil Engineers, 322, 37-50. (in Japanese)
3) Matsuda, K., Kato, K., Hisatomi, K. and Suda, K., 2013. Low speed instability of two-dimensional rectangular prisms, Proceeding of the ASME 2013 Pressure Vessels and Piping Conference (PVP2013), 97353, Paris, France.
4) Matsuda, K., Kato, K., Tamai, Y., and Suda, K., 2016. Experimental study on aerodynamic vibrations of rectangular cross sections having low side ratios, Proceedings of 8th International Colloquium on Bluff Body Aerodynamics and Applications, Boston, USA.
5) Matsumoto, M., Shiraishi, N., Shirato, H., Stoyanoff, S. and Yagi, T., 1993. Mechanism of, and turbulence effect on vortex- induced oscillations for bridge box girders, Journal of Wind Engineering and Industrial Aerodynamics, 49 (1-3), 467-476.
6) Shimada, K., 1999. Evaluation of aerodynamic characteristics and aerodynamic elasticity behavior forecast of rectangular cylinders using k-ε model, Doctor's thesis, Kyoto University. (in Japanese)
7) Matsumoto, M., Yagi, T., Tamaki, H. and Tsubota, T., 2008. Vortex-induced vibration and its effect on torsional flutter instability in the case of B/D=4 rectangular cylinder, Journal of Wind Engineering and Industrial Aerodynamics, 96 (6-7), 971-983.
8) Okajima, A., 1990. Numerical simulation of flow around rectangular cylinders, Journal of Wind Engineering and Industrial Aerodynamics, 33, 171-180.
9) Okajima, A, 1983. Flow around a rectangular cylinder with a section of various width/height ratios, Journal of Wind Engineering, Japan Association for Wind Engineering, 17, 1-19. (in Japanese)
10) Yagi, T., Shinjo, K., Narita, S., Nakase, T. and Shirato, H., 2013. Interferences of vortex sheddings in galloping instability of rectangular cylinders, Journal of Structural Engineering, Japan Society of Civil Engineers, 59A, 552-561. (in

Japanese)

11) Shiraishi, N. and Matsumoto, M., 1984. On physical mechanism of vortex-induced oscillation and its response evaluation, Journal of Wind Engineering, Japan Association for Wind Engineering, 20, 103-127. (in Japanese)

Chapter 6: The Role of Secondary Vortex at Trailing Edge in Motion-induced Vortex Vibration for Specific Cross Sections

The role of the secondary vortex at trailing edge in the motion-induced vortex vibration for the rectangular cross sections in the heaving and the torsional modes has been discussed in chapter 3, chapter 4 and chapter 5. Nevertheless, with regard to a rectangular cross section, the secondary vortex at trailing edge will inevitably be generated when the non-dimensional double amplitude becomes large. Therefore, it is difficult to discuss the influence of the secondary vortex at trailing edge on the motion-induced vortex vibration at higher wind velocity regions where larger response amplitudes of the motion-induced vortex vibration occur, with respect to the rectangular cross sections. In this chapter, two kinds of specific cross sections where the secondary vortex at trailing edge is considered less likely to occur are used as the target cross sections. Spring-supported and flow visualization tests in the heaving mode were conducted. By comparing the flow patterns of the secondary vortex at trailing edge with the response characteristics of the target cross sections, this chapter aims to clarify the influence of secondary vortex at trailing edge on the response characteristic of motion-induced vortex vibration at wind velocity regions where larger response amplitudes occur.

6.1 Wind Tunnel Tests for Specific Cross Sections in a Heaving Mode

6.1.1 Target Cross Sections

The target cross sections in this chapter were designed on the basis of a rectangular cross section with a side ratio of B/D=2.0. The geometrical shape of the trailing edge of the rectangular cross section was adjusted in order to suppress the generation of the secondary vortex at trailing edge. By referring previous studies, two kinds of cross sections were designed as the target cross sections.

Figure 6.1.1 shows the comparison of the results of the flow visualization tests for the rectangular cross sections of with a side ratio of B/D=1.18 with the angles of attack α=0° and α=10°[1)]. A red dotted circle was added at the rear corner on the upper

surface in order to recognize whether or not the secondary vortex at trailing edge is generated. It is suggested that the secondary vortex at trailing edge on the upper surface of the model is less likely to be generated for the rectangular cross section with an angle of attack α=10°, compared with the one whose angle of attack is α=0°. Therefore, the gradient θ was provided in a mainstream direction at the downstream side on both upper and lower surfaces of a rectangular cross section with a side ratio of B/D=2.0, in order to ensure that the secondary vortex at trailing edge is less likely to be generated on both upper and lower surfaces. The gradient θ was changed to θ=5°, 10° and 15°.The Schematic illustration of the sectional model is shown in **Figure 6.1.2**. Hereinafter, this kind of target cross section is referred to as TYPE-1.

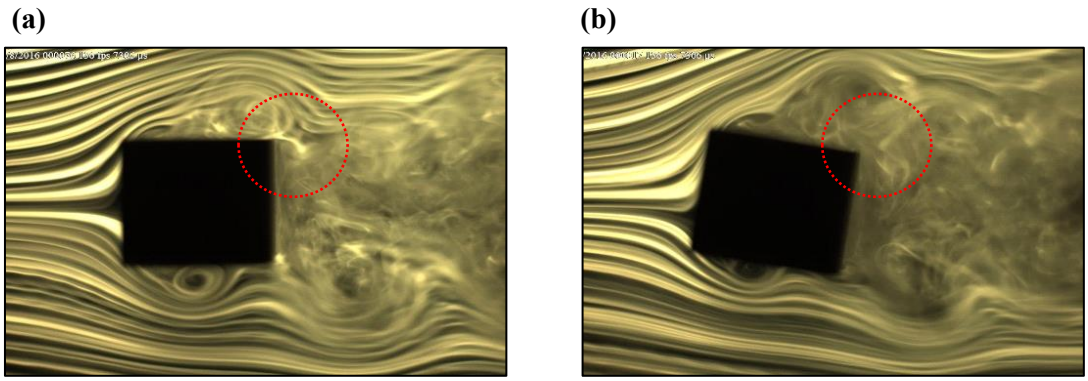

Figure 6.1.1 (a) Results of the flow visualization tests for B/D=1.18 with an angle of attack α=0° and (b) an angle of attack α=10° at the upper displacement (V_r=2.0, $2\eta/D$=0.10)[1)]

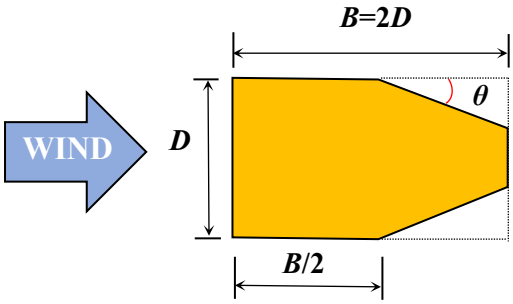

Figure 6.1.2 Schematic illustration of the sectional model of TYPE-1 (B/D=2.0)

Figure 6.1.3 shows the measurement of the fluctuating pressure coefficient distribution within the wind velocity region of the motion-induced vortex vibration for a rectangular cross section with a side ratio of B/D=3.0 with a vertical plate attached on the upper surface[2)]. It is found that on the upper side of the leeward face, the fluctuating pressure coefficient is much smaller than that in the opposite position due

to the installation of the vertical plate. Hence, it can be considered that the installation of the vertical plate has an effect which can eliminate the shedding of the secondary vortex at trailing edge. Thus, a rectangular cross section with a side ratio of B/D=2.0 attached with two vertical plates at the trailing edge on both the upper and lower surfaces of the model was selected as the target cross section where the secondary vortex at trailing edge is considered less likely to be generated. The lengths of the vertical plate L were set as L=0.25D, 0.50D and 0.75D. The schematic illustration of

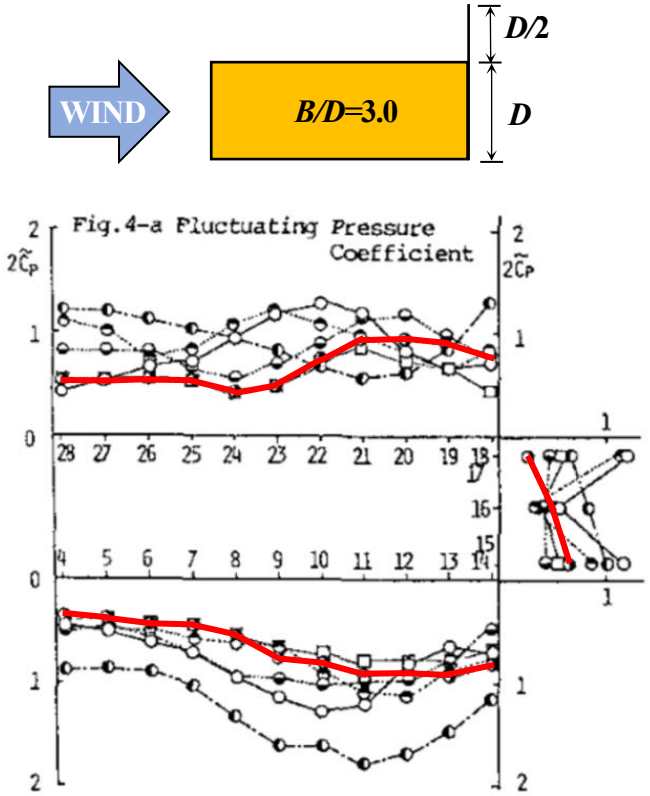

Figure 6.1.3 Measurement of the fluctuating pressure coefficient distribution for B/D=3.0 with a vertical plate attached on the upper surface (V_r=9.0, 2η/D=0.14)[2)]

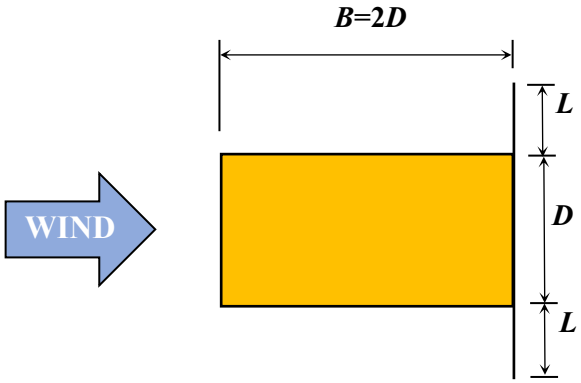

Figure 6.1.4 Schematic illustration of the sectional model of TYPE-2 (B/D=2.0)

the sectional model is shown in **Figure 6.1.4**. Hereinafter, this kind of target cross section is referred to as TYPE-2.

6.1.2 Spring-supported Tests

(1) Wind tunnel

The spring-supported tests in the heaving mode were conducted in a closed circuit wind tunnel at Kyushu Institute of Technology in order to obtain the response characteristics of the target cross sections. This closed circuit wind tunnel is the same as the one which has been demonstrated in chapter 3. The spring-supported tests were carried out in a smooth flow with a turbulence of less than 0.5%. The wind velocity V in the spring-supported tests was from 1.5m/s to 12m/s. The Reynolds number in the wind velocity region of the motion-induced vortex vibration was $Re=VD/\nu=7.2\times10^3$-2.8×10^4, where V: wind velocity (m/s), D: cross-wind length (m), ν: kinematic viscosity (m^2/s).

(2) Specifications of target models

The models of TYPE-1 cross sections were constructed of cypress wood. Two end plates were attached with at both ends of the models, in order to make the flow around the models appear as a two-dimensional flow. **Figure 6.1.5** shows the sectional model of TYPE-1 cross section with the gradient of θ=10° inside the wind tunnel.

Figure 6.1.5 Sectional model of TYPE-1 cross section (θ=10°) inside the wind tunnel

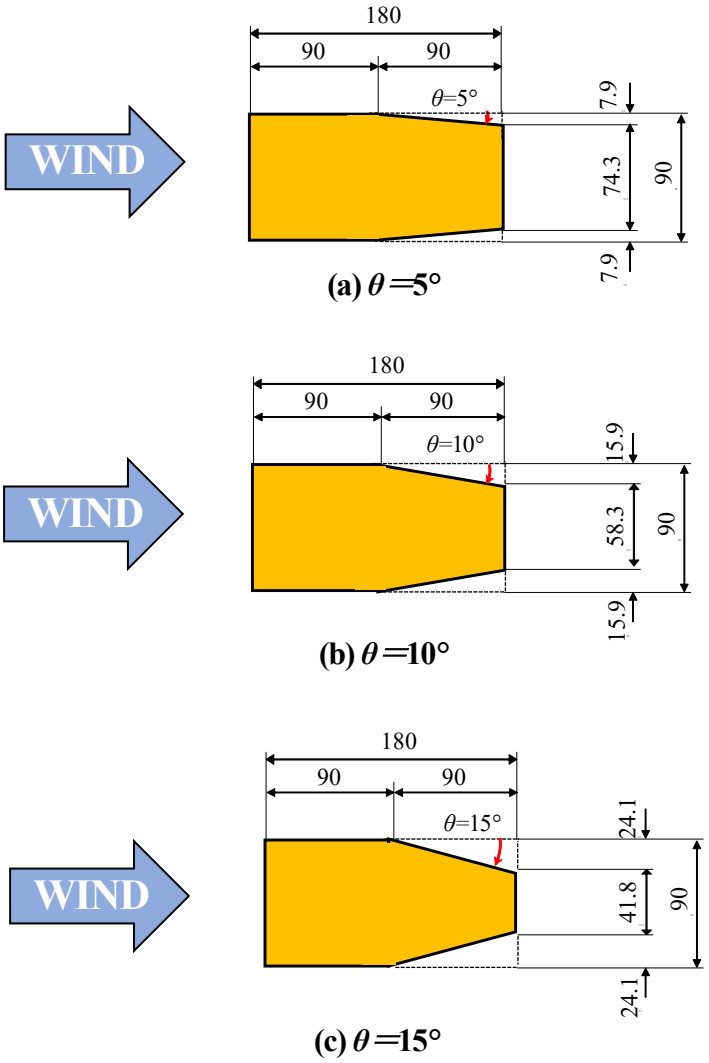

Figure 6.1.6 Size of models of TYPE-1 cross sections (unit: mm)

Figure 6.1.6 shows the size of models of TYPE-1 cross sections. The model length was 828mm for all cross sections.

The models of TYPE-2 cross sections were composed of a rectangular sectional model with a side ratio of *B/D*=2.0 and a cypress plate fixed on the leeward face of the sectional model. The thickness of the cypress plate was 2mm. Two end plates were also attached with at both ends of the models. **Figure 6.1.7** shows the size of models of TYPE-2 cross sections. It should be noted that in order to ensure that the wind in the wind tunnel is a smooth flow, the wind velocity in the wind tunnel must be set at no less than 1.5m/s. Thus, the blockage ratios of TYPE-2 cross sections were moderated to 6%, 8% and 10%, respectively, in order to ensure that the spring-supported tests for TYPE-2 cross sections can be carried out normally. With regard to

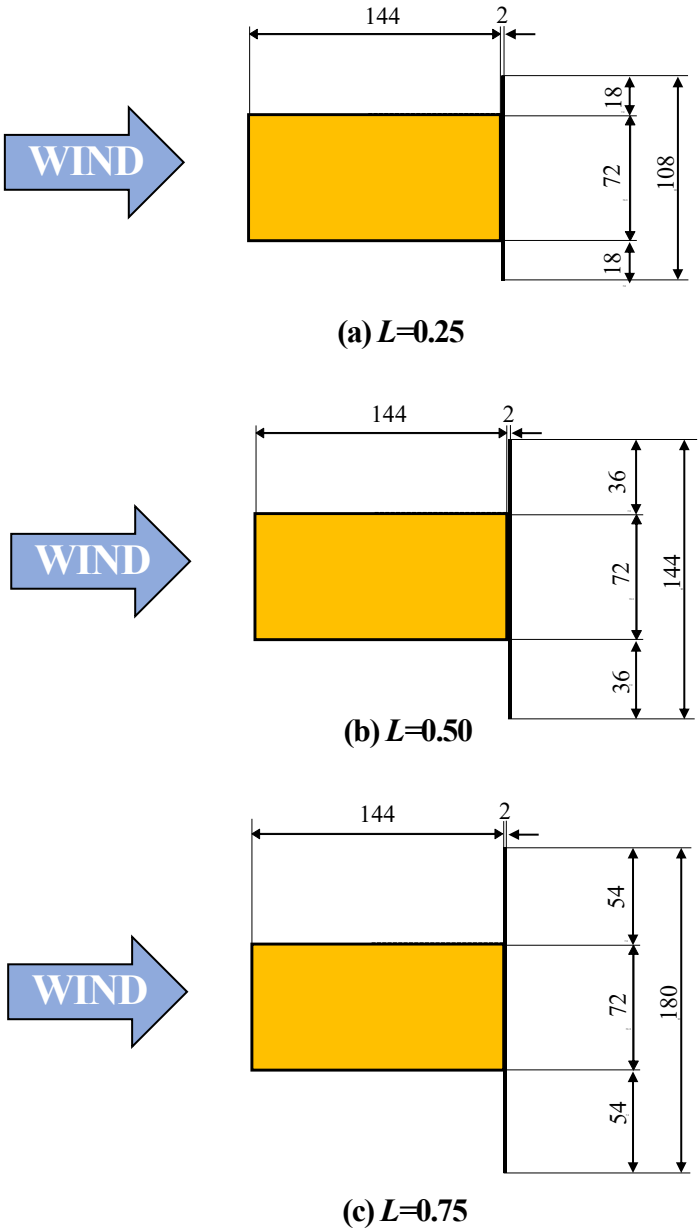

Figure 6.1.7 Size of models of TYPE-2 cross sections (unit: mm)

this moderation of the blockage ratio, according to the past results of spring-supported tests for B/D=1.18 with blockage ratio of 10% and 5%, it is confirmed that the difference in blockage ratio did not influence the response characteristics in the wind region of the motion-induced vortex vibration[3), 4)].

(3) Measurement system

The measurement and suspension systems are the same as the ones which have been demonstrated in chapter 3. The angle of attack was set as 0° for all the experiments. The models were supported in the wind tunnel elastically in the heaving mode by two coil springs at each side. The response amplitude of the models during

Figure 6.1.8 Suspension situation outside the wind tunnel

vibration was measured by a laser displacement detector. **Figure 6.1.8** shows the suspension situation outside the wind tunnel. The vibration system was so well designed that the structural damping of the vibration system could be reduced to as small as possible. The structural damping of the vibration system was adjusted with a pair of magnetic dampers.

(4) Experimental conditions of spring-supported tests

Table 6.1.1 shows the experimental conditions of the spring-supported tests. The Scruton number $Sc=2m\delta/\rho D^2$ for each cross section was adjusted as the same. In addition, a rectangular cross section with a side ratio of $B/D=2.0$ was also added for the spring-supported tests for purpose of comparison.

Table 6.1.1 Experimental conditions for spring-supported tests

Cross sectional type	B (mm)	D (mm)	Gradient θ	Vertical plate L	Natural frequency f (Hz)	Mass per unite length m (kg/m)	Logarithmic decrement of structural damping δ	Air density ρ (kg/m^3)	Sc
Rectangular	180	90	-	-	5.25	5.43	0.0043	1.21	4.7
TYPE-1	180	90	5°	-	7.23	2.87	0.0079	1.19	4.7
	180	90	10°	-	7.27	2.83	0.0081	1.20	4.7
	180	90	15°	-	7.29	2.82	0.0080	1.19	4.7
TYPE-2	144	72	-	0.25D	6.32	3.56	0.0041	1.20	4.7
	144	72	-	0.50D	6.76	3.11	0.0047	1.20	4.7
	144	72	-	0.75D	6.58	3.29	0.0045	1.22	4.7

Model length: 828mm

6.1.3 Flow Visualization Tests

(1) Wind tunnel

Flow visualization around a forced-oscillating model was conducted in a small-sized wind tunnel at Kyushu Institute of Technology. The small-sized wind tunnel is the same as the one demonstrated in chapter 3. The wind velocity V in the flow visualization tests was set as 0.6m/s or 0.8m/s which was good for visualization.

The Reynolds number in the flow visualization tests was $Re=VD/\nu=0.9\times10^3$-1.1×10^3, which is smaller than that in the spring-supported tests by approximately one order of magnitude. However, regarding a cross section with sharp corners, the separation point is fixed at the corner, and does not depend on the Reynolds number. For instance, according to the results of the measurements of the Strouhal numbers St in various Reynolds number range for a rectangular cross section with a side ratio of B/D=2.0, the Strouhal numbers in the Reynolds number range of $Re=0.9\times10^3$-1.1×10^3 and $Re=7.2\times10^3$-2.8×10^4 are St=0.08 and St=0.07, respectively[5]. Thus, it is deemed that the influence caused by different Reynolds numbers on the separated vortex from leading edge and the secondary vortex at trailing edge is small. Hence, it is reasonable to have qualitative discussion based on the results of spring-supported and flow visualization tests.

(2) Specifications of target models

The models of TYPE-1 and TYPE-2 cross sections used in flow visualization tests were made of transparent acrylic panels. All the models were painted in black while the central part of the models which were illuminated by a light source was transparent, for the sake of making the flow patterns around the model as bright as possible. An end plate was attached at the end of each model for the sake of ensuring that the flow around the model was two-dimensional. The model length was 150mm for all cross sections. **Figure 6.1.9** and **Figure 6.1.10** show the size of models of TYPE-1 and TYPE-2 cross sections, respectively. **Figure 6.1.11** shows the model of TYPE-1 with the gradient of θ=15° used in flow visualization tests inside the wind tunnel.

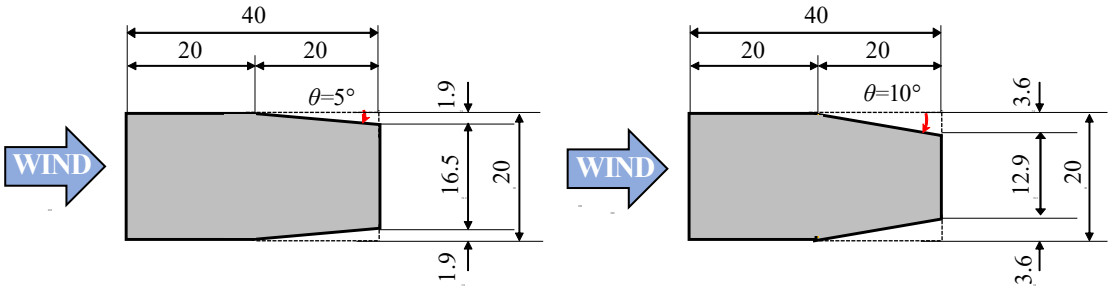

(a) θ=5° (b) θ=10°

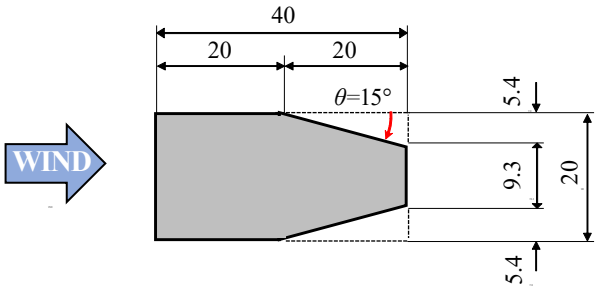

(c) θ=15°

Figure 6.1.9 Size of models of TYPE-1 cross sections (unit: mm)

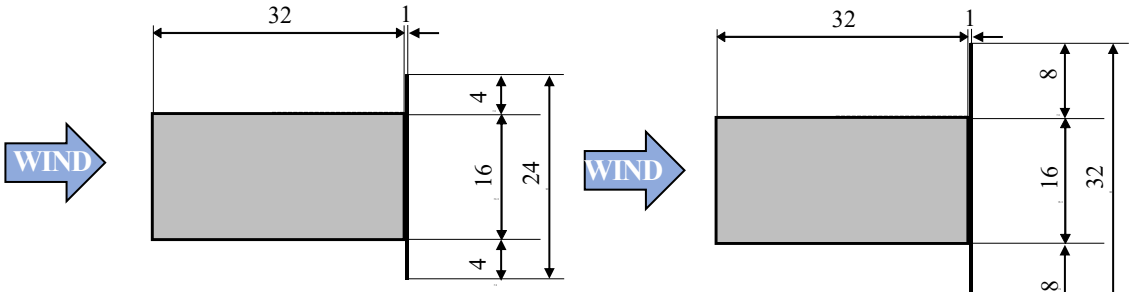

(a) L=0.25 (b) L=0.50

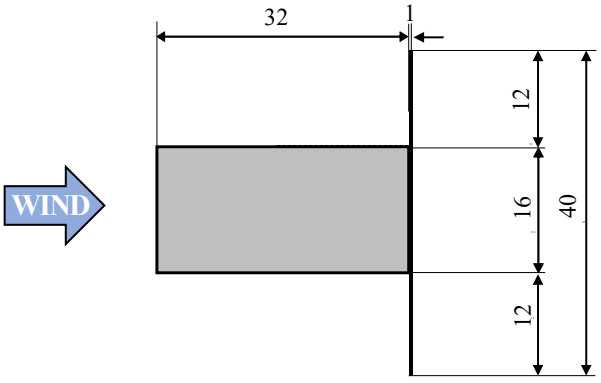

(c) L=0.75

Figure 6.1.10 Size of models of TYPE-2 cross sections (unit: mm)

Figure 6.1.11 Setting situation of the model of TYPE-1(θ=15°) inside the wind tunnel

(3) Measurement system

Flow visualization around a forced-oscillating model were conducted by the smoke wire method. The experimental setup and forced oscillation system are the same as the ones which have been introduced in chapter 3. The forced-oscillating frequency and amplitude were adjusted by a digital function signal generator and an amplifier, respectively. The flow patterns around the model were photographed with a high-speed camera. In each forced-oscillating amplitude, the models were photographed for ten periods of vibration. The photographed pictures were processed with the Motion Studio X64 software in a computer.

(4) Experimental conditions of flow visualization tests

Table 6.1.2 shows the experimental conditions of flow visualization tests. Based on the results obtained from the spring-supported tests, at the onset wind velocity and the velocity where a larger response amplitude of the motion-induced vortex vibration occurred, the non-dimensional forced-oscillating double amplitude was set as $2\eta/D$=0.02-0.30 (every 0.02 intervals), in order to verify the effect of the secondary vortex at trailing edge on the response characteristics of the motion-induced vortex vibration. It should be noted that in the results of the spring-supported tests, a limit cycle was confirmed for all of the cases at the vicinity of the wind velocity where the maximum response amplitude of the motion-induced vortex vibration occurred. The

flow visualization tests were therefore conducted at lower wind velocities than the wind velocity where the maximum response amplitude of the motion-induced vortex vibration occurred, in order to ensure that the measurement points were within the response amplitude range of the motion-induced vortex vibration. A rectangular cross section with a side ratio of B/D=2.0 was also added for the flow visualization tests for comparison.

Table 6.1.2 Experimental conditions for flow visualization tests

Cross sectional type	B (mm)	D (mm)	Gradient θ	Vertical plate L	Wind velocity (m/s)	Forced-oscillating frequency f (Hz)	Reduced wind velocity $Vr=V/fD$	Forced-oscillating amplitude $2\eta/D$
Rectangular	40	20	-	-	0.8	10.52	3.8	0.02-0.20
					0.8	7.69	5.2	0.02-0.20
TYPE-1	40	20	5°	-	0.6	7.69	3.9	0.02-0.30
					0.6	5.77	5.2	0.02-0.30
	40	20	10°	-	0.6	7.50	4.0	0.02-0.30
					0.6	5.77	5.2	0.02-0.30
	40	20	15°	-	0.6	6.52	4.6	0.02-0.30
					0.6	5.77	5.2	0.02-0.30
TYPE-2	32	16	-	0.25D	0.6	9.38	4.0	0.02-0.30
					0.6	7.98	4.7	0.02-0.30
	32	16	-	0.50D	0.6	9.38	4.0	0.02-0.30
					0.6	7.98	4.7	0.02-0.30
	32	16	-	0.75D	0.6	9.15	4.1	0.02-0.30
					0.6	7.98	4.7	0.02-0.30

Model length: 150mm

6.2 Response Characteristics of Target Cross Sections in a Heaving Mode

(1) TYPE-1 cross sections

The results of spring-supported tests for TYPE-1 cross sections and the rectangular cross section of B/D=2.0 are shown in **Figure 6.2.1**. Vortex-induced vibrations were confirmed as occurring at approximately V_r=3 for all cross sections. These vortex-induced vibrations are considered to be the motion-induced vortex vibrations. Because the onset reduced wind velocities of these vortex-induced vibrations approximately coincide with the empirical value of the onset reduced wind velocity of the motion-induced vortex vibration V_{cr}=1.67B/D=3.34. Along with the increase of the reduced wind velocity, the galloping was confirmed for all four cross sections. Furthermore, by comparing with the result of rectangular cross section, it was confirmed that the onset of the galloping occurs at lower reduced wind velocities for TYPE -1 cross sections.

The maximum response amplitudes of the motion-induced vortex vibration for three TYPE-1 cross sections are smaller, compared with the result of the rectangular cross section. **Figure 6.2.2-Figure 6.2.5** show the one period of vibration of the results

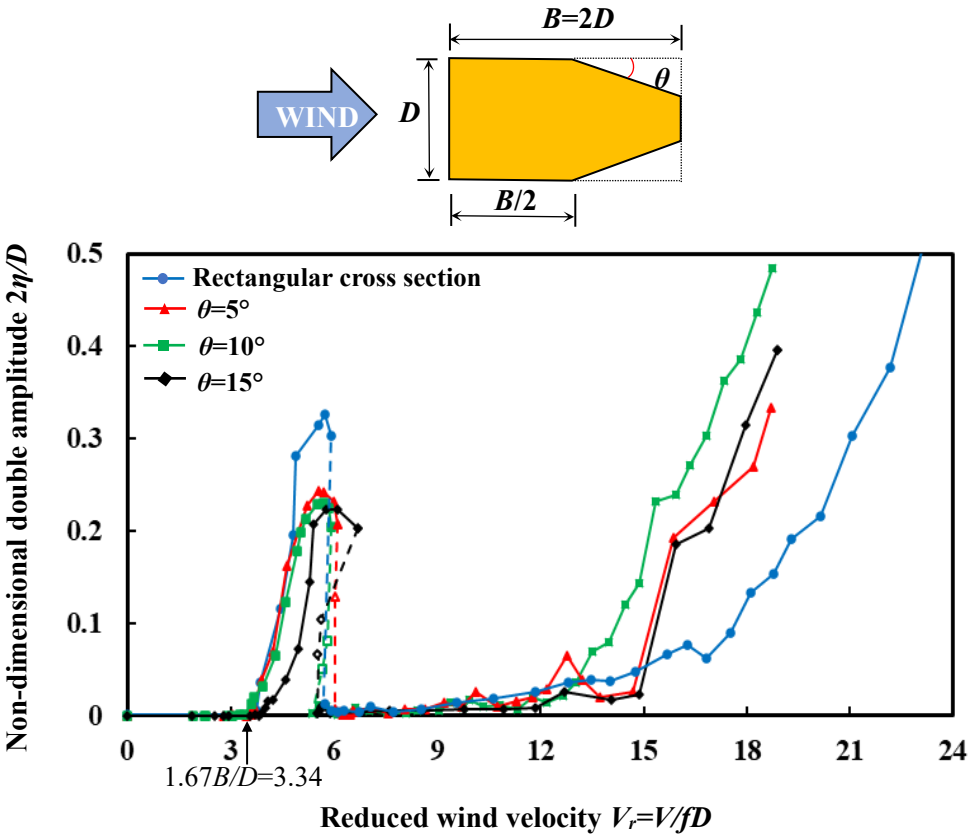

Figure 6.2.1 *V-A* diagrams of TYPE-1 and rectangular cross sections (B/D=2.0, Sc=4.7)

of the flow visualization tests for rectangular and TYPE-1 cross sections at V_r=5.2 which is close to the reduced wind velocity where the maximum response amplitude of the motion-induced vortex vibration occurred in a forced-oscillating amplitude of $2\eta/D$=0.20. By comparing the flow patterns of the separated vortex from leading edge in different cross sections, it was found that the separated vortices from leading edge

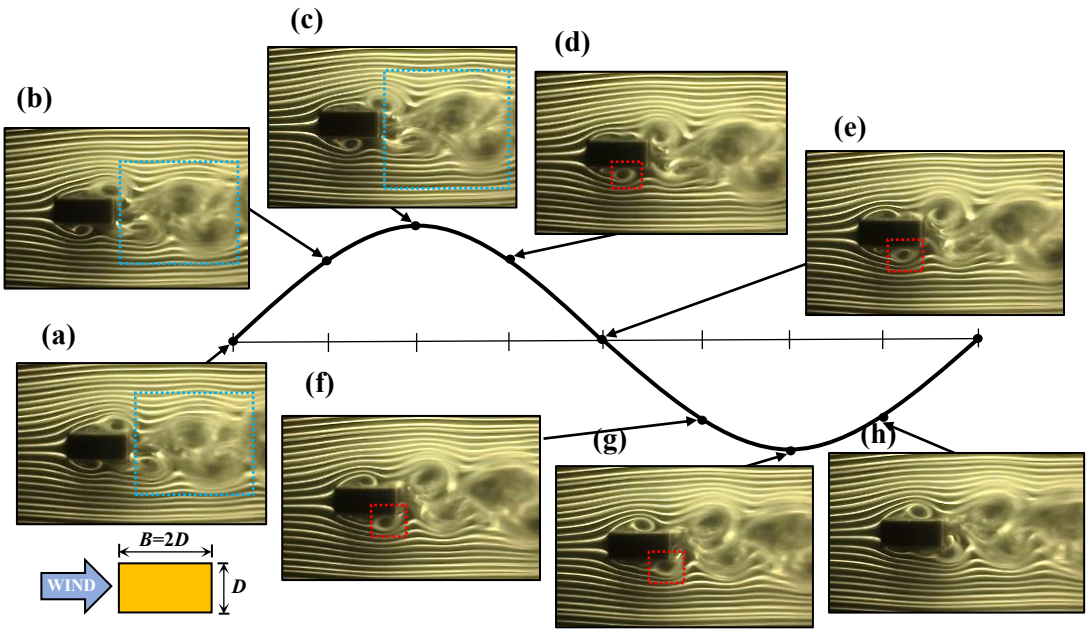

Figure 6.2.2 Results of flow visualization tests of rectangular cross section (B/D=2.0) at V_r=5.2 in $2\eta/D$=0.20

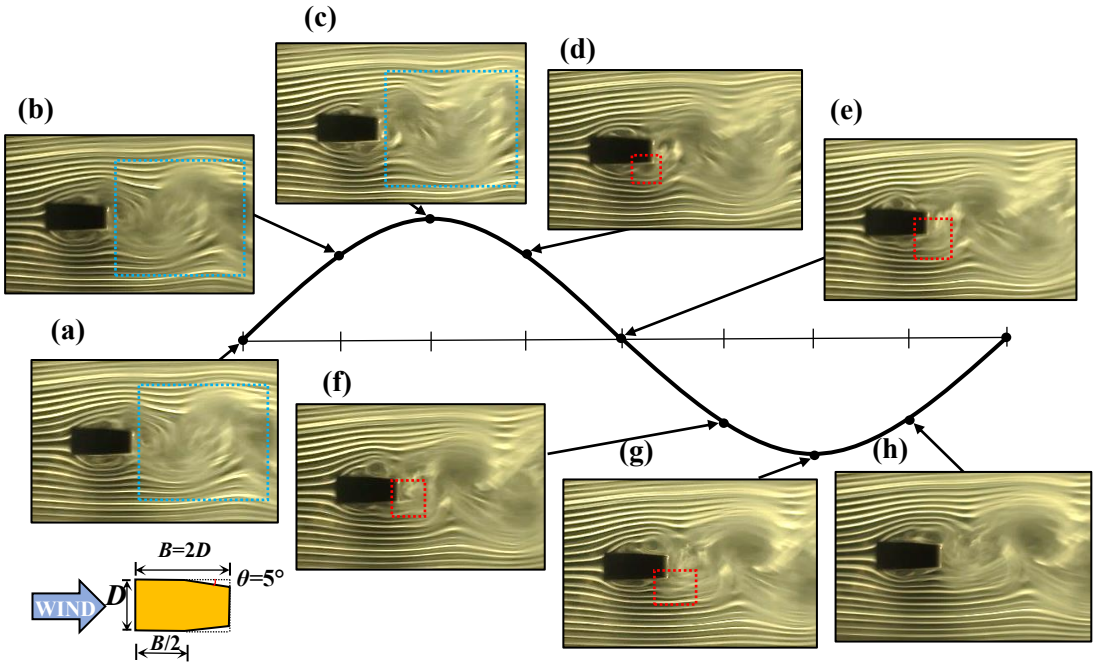

Figure 6.2.3 Results of flow visualization tests of TYPE-1 cross section (B/D=2.0, θ=5°) at V_r=5.2 in $2\eta/D$=0.20

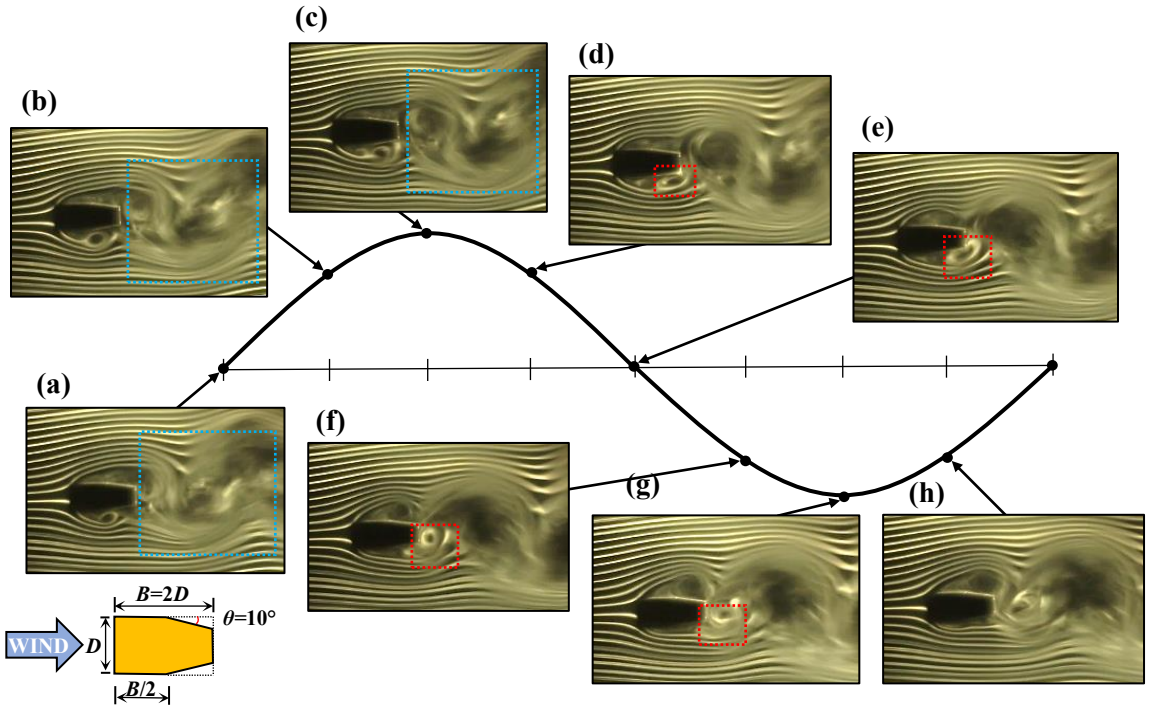

Figure 6.2.4 Results of flow visualization tests of TYPE-1 cross section (B/D=2.0, θ=10°) at V_r=5.2 in $2\eta/D$=0.20

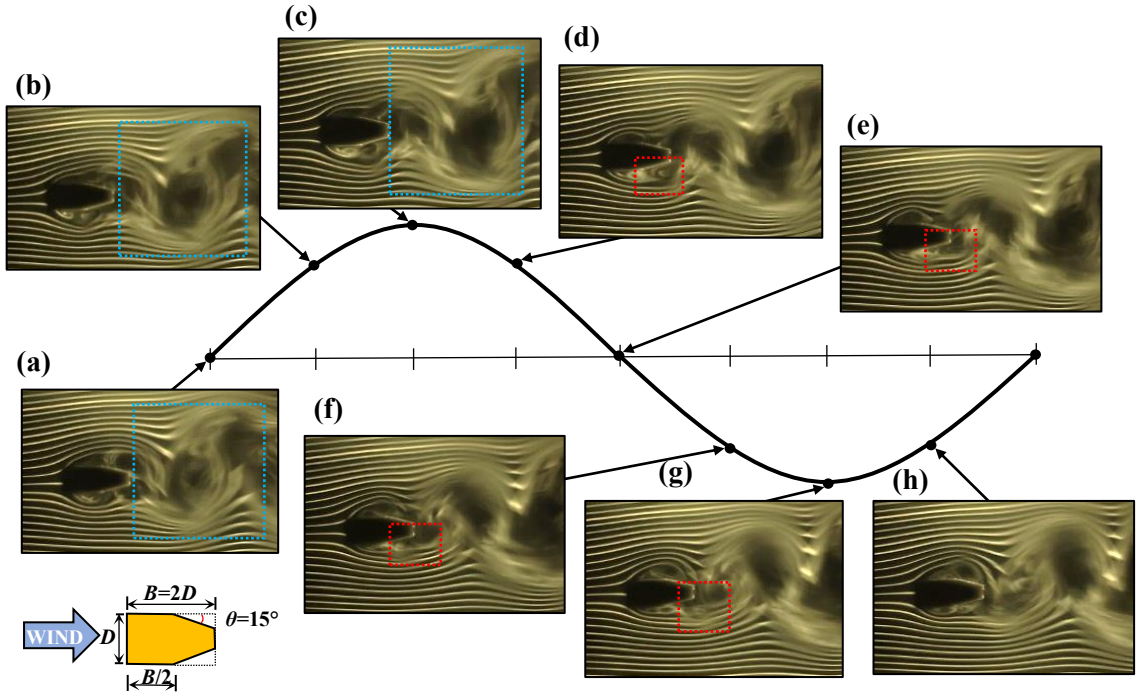

Figure 6.2.5 Results of flow visualization tests of TYPE-1 cross section (B/D=2.0, θ=15°) at V_r=5.2 in $2\eta/D$=0.20

in TYPE-1 cross sections are not as stable as those in the rectangular cross section. As shown in **Figure 6.2.2(d)-(g)-Figure 6.2.5 (d)-(g)**, the separated vortices from leading edge which are surrounded by red dotted lines on the lower surface tends to disperse while moving toward the leeward part of the surface for TYPE-1 cross sections. The

fluctuating wind pressure acting on TYPE-1 cross sections therefore is considered to be smaller than that on the rectangular cross section. As a consequence, the maximum response amplitudes of the motion-induced vortex vibration for three TYPE-1 cross sections are smaller than for the rectangular cross section.

TYPE-1 and the rectangular cross sections show different flow properties with respect to the flow patterns in the wake. For instance, in **Figure 6.2.2 (a)-(c)-Figure 6.2.5 (a)-(c)**, the separated shear layers in the wake of the four cross sections are surrounded by blue lines. It was confirmed that the curvatures of the separated shear layers in the wake of TYPE-1 cross sections are larger, by comparing with the flow patterns in the rectangular cross section. This result has a similar tendency to the previous research[6]. Furthermore, the larger the gradient θ is, the larger the curvatures of the separated shear layers tend to become.

In addition, it was confirmed that the maximum response amplitudes of the motion-induced vortex vibrations for the three TYPE-1 cross sections are approximately the same regardless of the value of gradient θ. However, with regard to the cross section having a gradient of θ=15°, the overall wind velocity range of motion-induced vortex vibration shifted to the side of high wind velocity, compared with other cross sections. This phenomenon can be related to the difference in the convection velocity of the separated vortex from leading edge. Further investigation is needed.

(2) TYPE-2 cross sections

The results of spring-supported tests for TYPE-2 cross sections and the rectangular cross section of B/D=2.0 are shown in **Figure 6.2.6**. In lower reduced wind velocity region, similar to the results of TYPE-1 cross sections, vortex-induced vibrations were confirmed as occurring at approximately V_r=3 for all cross sections. These vortex-induced vortex vibrations are suggested to be the motion-induced vortex vibration, as the onset reduced wind velocities approximately correspond to the empirical value of the onset reduced wind velocity of motion-induced vortex vibration V_{cr}=1.67B/D=3.34. In higher wind velocity regions, in contrast to the results of TYPE-1 cross sections, the galloping was not confirmed for the three cases of TYPE-2 cross sections.

Figure 6.2.7 shows the enlarged view of the wind velocity region of the motion-induced vortex vibration for TYPE-2 and rectangular cross sections. The onset and the

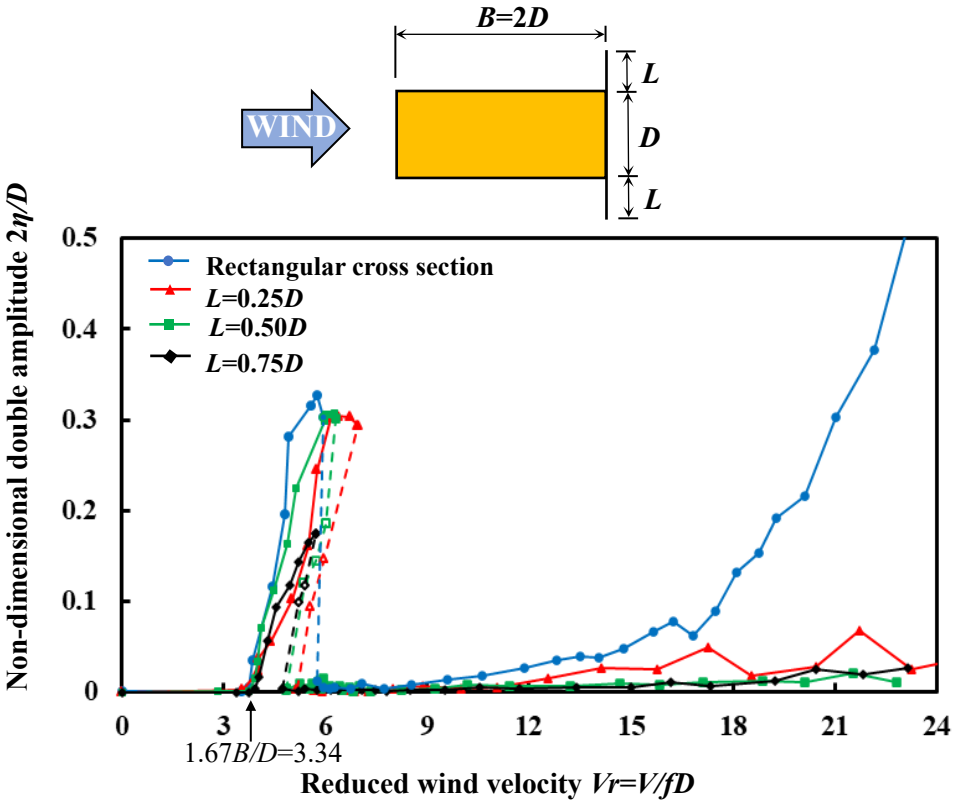

Figure 6.2.6 *V-A* diagrams of TYPE-2 and rectangular cross sections (*B/D*=2.0, *Sc*=4.7)

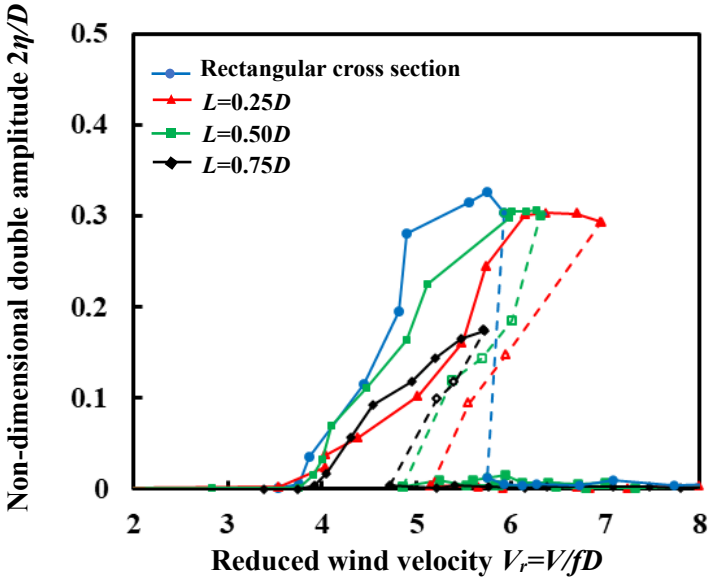

Figure 6.2.7 *V-A* diagrams for TYPE-2 and rectangular cross sections in the wind velocity region of motion-induced vortex vibration (*B/D*=2.0, *Sc*=4.7)

growth of the response amplitudes of the motion-induced vortex vibration for TYPE-2 cross sections were confirmed in higher wind velocity regions, compared with the result of the rectangular cross section. On one hand, according to the results of previous wind tunnel tests[2)], a vertical plate attached at the trailing edge of the model has an

effect which can reduce the convection velocity of the separated vortex from leading edge on the surface of the model. On the other hand, regarding a rectangular cross section, the empirical value of the onset reduced wind velocity of the motion-induced vortex vibration V_{cr}=1.67B/D is obtained based on the fact that the separated vortex from leading edge convection along the surface is approximately 60% of the approaching wind velocity[7]. As the side ratio B/D is constant for all of the cases, it can be considered that the convection velocity of the separated vortex from leading edge on the surface for TYPE-2 cross sections is lower than 60% of the approaching wind velocity. Therefore, the onset and the peak response amplitude of the motion-induced vortex vibration for TYPE-2 cross sections were confirmed as occurring at higher wind velocities than for the rectangular cross section.

As shown in **Figure 6.2.7**, it was confirmed that the maximum response amplitude of the motion-induced vortex vibration for rectangular cross section and TYPE-2 cross sections with vertical plates of L=0.25D, 0.50D nearly have the same value, whereas for TYPE-2 cross section with a vertical plate of L=0.75D, a significant decline was confirmed in terms of the maximum response amplitude. **Figure 6.2.8-Figure 6.2.10** show the one period of vibration of the results of the flow visualization tests for

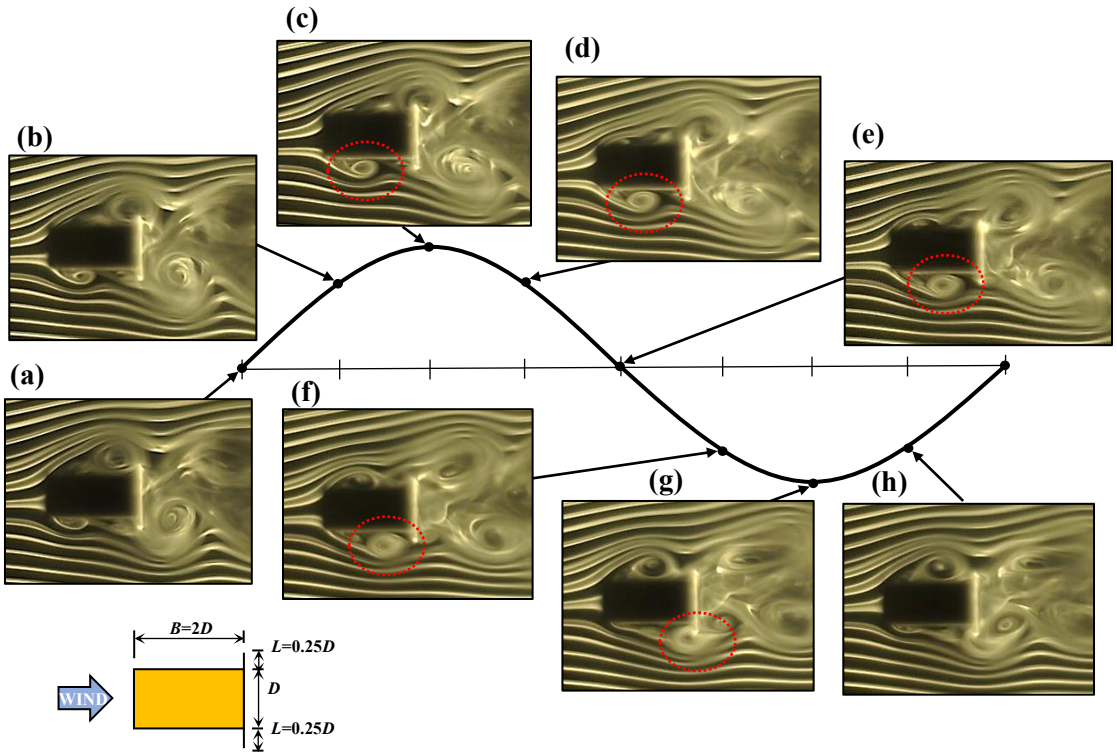

Figure 6.2.8 Results of flow visualization tests of TYPE-2 cross section (B/D=2.0, L=0.25D) at V_r=4.7 in 2η/D=0.20

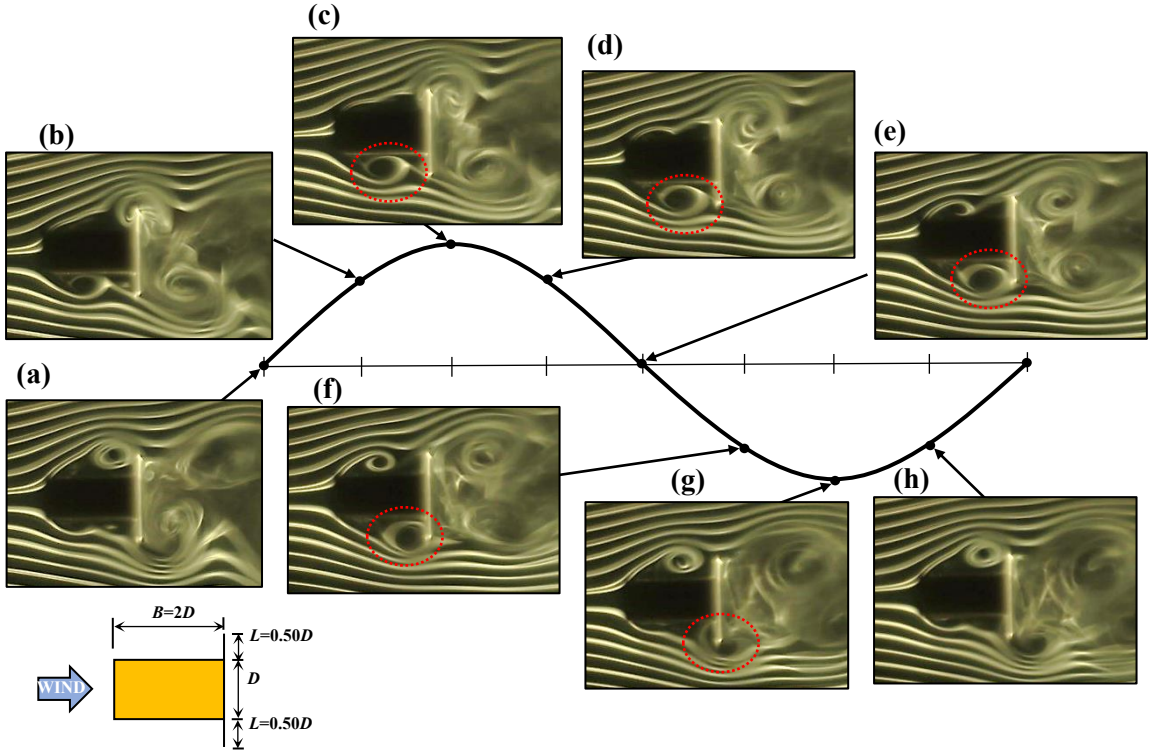

Figure 6.2.9 Results of flow visualization tests of TYPE-2 cross section (*B/D*=2.0, *L*=0.50*D*) at V_r=4.7 in 2η/*D*=0.20

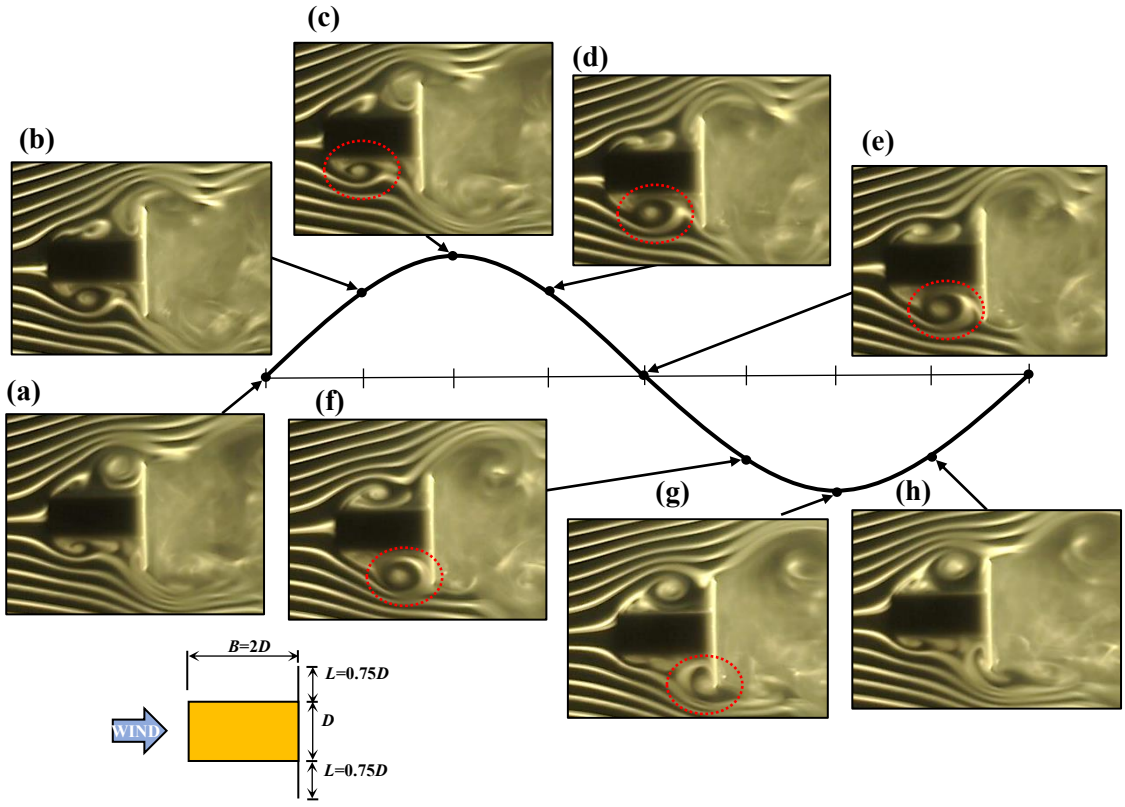

Figure 6.2.10 Results of flow visualization tests of TYPE-1 cross section (*B/D*=2.0, *L*=0.75*D*) at V_r=4.7 in 2η/*D*=0.20

rectangular and TYPE-2 cross sections at V_r=4.7 which is close to the reduced wind velocity where the maximum response amplitude of the motion-induced vortex vibration occurred in a forced-oscillating amplitude of $2\eta/D$=0.20. A red dotted line was added in the **Figure 6.2.8 (c)-(g)-Figure 6.2.10 (c)-(g)** in order to confirm the flow pattern of the separated vortex from leading edge on the lower surface. It was found that at the leeward part of the cross sections with a vertical plate of L=0.75D, the vertical plate inhibited the separated vortex from leading edge from moving along the lower surface of the model. As a result, the separated vortex from leading edge gradually separated from the lower surface of the model, as shown in **Figure 6.2.10 (e)-(g)**. Thus, the fluctuating lift provided by the separated vortex from leading edge did not seem to fully act on the model. Therefore, the fluctuating lift of the motion-induced vortex vibration for the cross sections with a vertical plate of L=0.75D was considered to decrease, compared with the other cross sections.

6.3 Necessity of Secondary Vortex at Trailing Edge for the Onset of Motion-induced Vortex Vibration for Target Cross Sections in a Heaving Mode

In the reduced wind velocity region of motion-induced vortex vibration, each model was photographed for ten periods of vibration when it was at forced-oscillating condition in the small-sized wind tunnel. In one period of vibration, there will be up to two secondary vortices at trailing edge generated. Thus, in ten periods of vibration, there will be up to twenty secondary vortices at trailing edge generated. Therefore, the generation probability of the secondary vortex at trailing edge is defined as (the number of secondary vortex at trailing edge/20)×100 (%). This was used as an index showing the extent of the stability of the secondary vortex at trailing edge. It should be noted that in a large amplitude range, the flow patterns of the secondary vortices at trailing edge are similar for each cross section. For the sake of convenience in showing the difference between the results obtained in higher and lower amplitudes, only the results of flow visualization tests conducted in a higher and a lower amplitude were demonstrated in this section.

(1) TYPE-1 cross sections

Figure 6.3.1 (a)-Figure 6.3.3 (a) show the relation between the generation probability of the secondary vortex at trailing edge and forced-oscillating amplitude at the onset reduced wind velocity of motion-induced vortex vibration for TYPE-1 cross

sections. **Figure 6.3.1 (b)-Figure 6.3.3 (b)** show the photographs of flow visualization tests taken in a higher and a lower amplitude. A red dotted rectangle was added at the rear corner in the bottom surface in order to recognize whether or not the secondary vortex at trailing edge is generated. **Figure 6.3.1 (c)-Figure 6.3.3 (c)** show the *V-A* diagrams in the wind velocity region of motion-induced vortex vibration. The results of rectangular cross section of *B/D*=2.0 are shown in **Figure 6.3.4** for the purpose of comparison. In all the cross sections, the separated vortex from leading edge was confirmed regardless of the forced-oscillating amplitude. On the other hand, in the TYPE-1 cross section of θ=5° as shown in **Figure 6.3.1**, the generation probability of

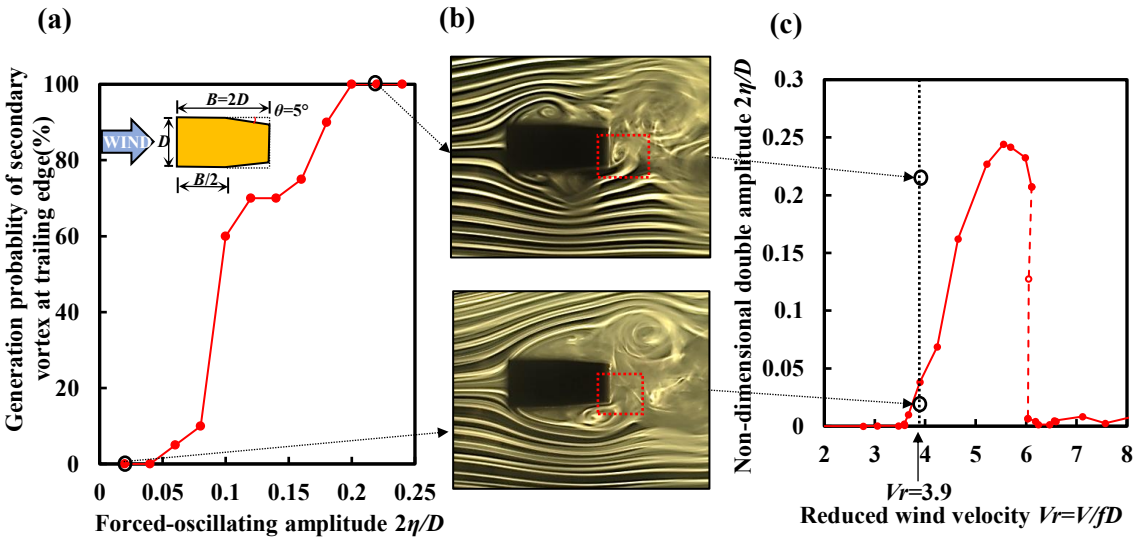

Figure 6.3.1 (a) Generation probability of secondary vortex at trailing edge, (b) flow visualization results at middle displacement with the maximum downward velocity at *Vr*=3.9 and (c) *V-A* diagram of TYPE-1 cross section (θ=5°, *Sc*=4.7)

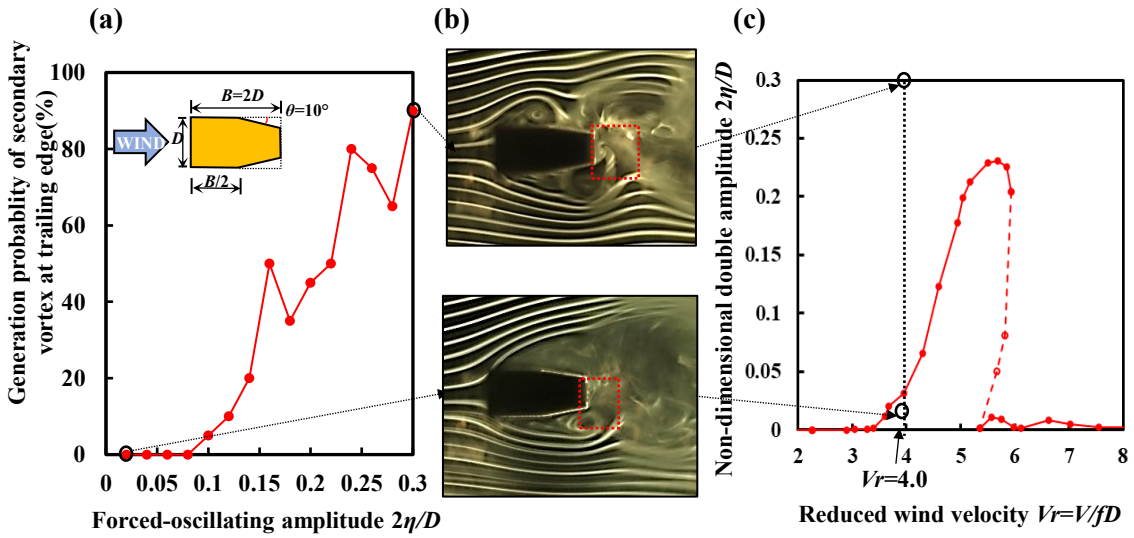

Figure 6.3.2 (a) Generation probability of secondary vortex at trailing edge, (b) flow visualization results at middle displacement with the maximum downward velocity at *Vr*=4.0 and (c) *V-A* diagram of TYPE-1 cross section (θ=10°, *Sc*=4.7)

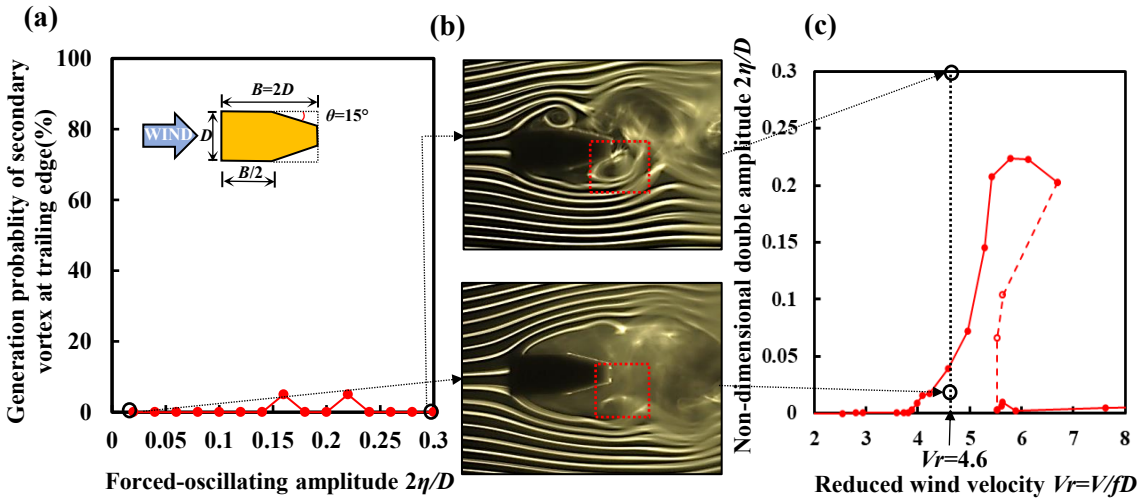

Figure 6.3.3 (a) Generation probability of secondary vortex at trailing edge, (b) flow visualization results at middle displacement with the maximum downward velocity at *Vr*=4.6 and (c) *V-A* diagram of TYPE-1 cross section (*θ*=15°, *Sc*=4.7)

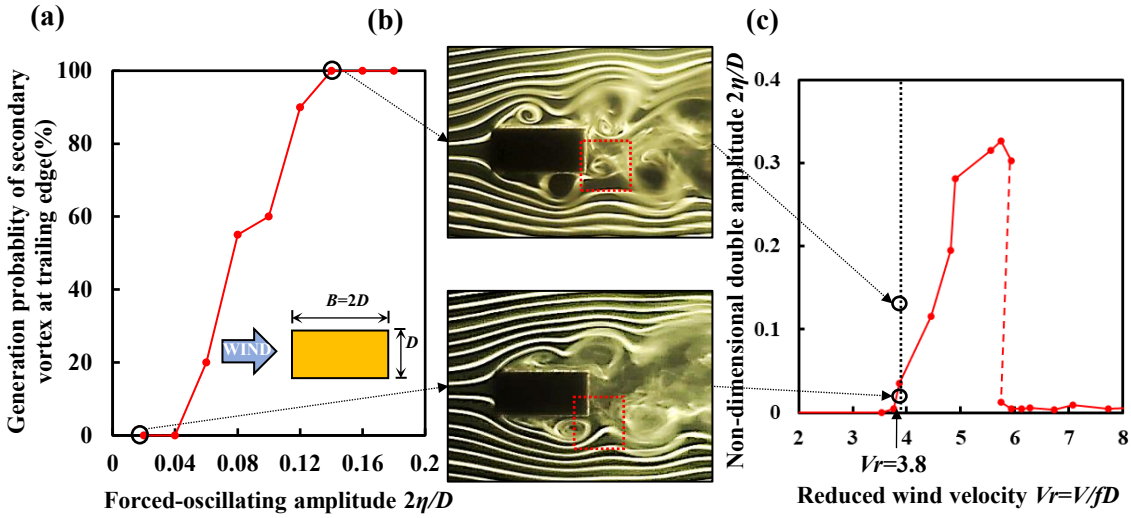

Figure 6.3.4 (a) Generation probability of secondary vortex at trailing edge, (b) flow visualization results at middle displacement with the maximum downward velocity at *Vr*=3.8 and (c) *V-A* diagram of rectangular cross section (*Sc*=4.7)

secondary vortex at trailing edge reached 100% in the forced-oscillating amplitude of $2\eta/D$=0.20, and the unification of secondary vortex at trailing edge and separated vortex from leading edge was observed. This result shows good agreement with the previous wind tunnel test[7]. However, in lower amplitudes, the secondary vortex at trailing edge was not confirmed. For instance, in the cross section of θ=5°, at the reduced wind velocity of V_r=3.9 where the motion-induced vortex vibration has generated, the secondary vortex at trailing edge was not confirmed in the amplitudes smaller than $2\eta/D$=0.06. In other words, the motion-induced vortex vibration can occur without the generation of the secondary vortex at trailing edge. A similar tendency was confirmed in the cross section of θ=10°, as shown in **Figure 6.3.2**. In addition, there was hardly any the secondary vortex at trailing edge generated even in higher

amplitudes in the cross section of θ=15°, as shown in **Figure 6.3.3**. Therefore, with regard to TYPE-1 cross sections, it is suggested that the secondary vortex at trailing edge is not essential for the generation of the motion-induced vortex vibration. Further, based on the results of the measurement of generation probability of the secondary vortex at trailing edge for TYPE-1 cross sections, it is also clear that the gradient θ provided in a mainstream direction at the downstream side of a rectangular cross section has an effect which can suppress the generation of the secondary vortex at trailing edge. In addition, by comparing the relation between the generation probability of the secondary vortex at trailing edge and forced-oscillating amplitude for three TYPE-1 cross sections, it is found that the larger the gradient θ is, the less likely the secondary vortex at trailing edge tends to be generated.

(2) TYPE-2 cross sections

Figure 6.3.5-Figure 6.3.7 show the results of the measurement of generation probability of the secondary vortex at trailing edge at the onset reduced wind velocity of the motion-induced vortex vibration combining with the photographs of flow visualization tests and the *V-A* diagrams in the wind velocity region of the motion-induced vortex vibration for TYPE-2 cross sections. The separated vortex from leading edge was confirmed regardless of the forced-oscillating amplitude in all three cross sections. In a period of vibration, when a separated vortex from leading edge reaches the trailing edge and collides with the vertical plate, then a deformed vortex is

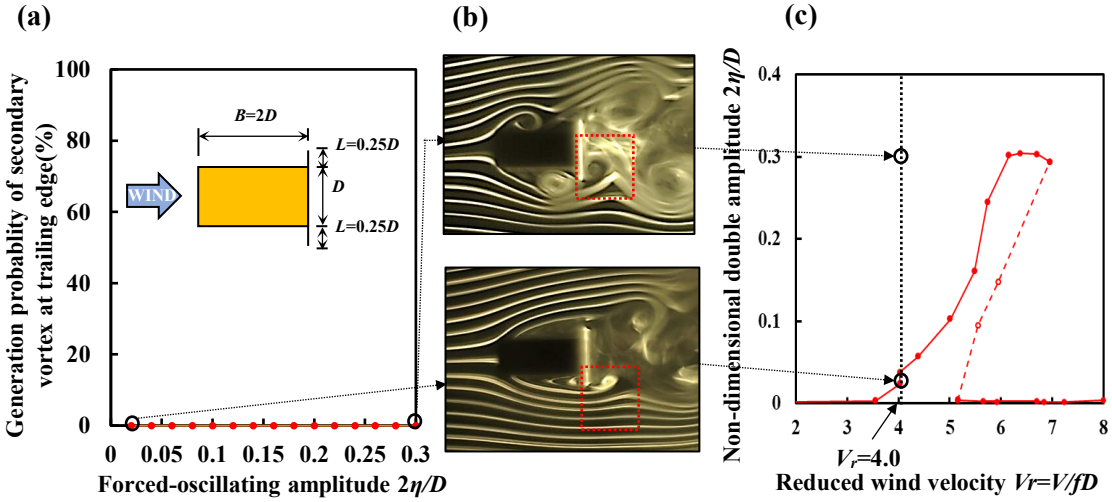

Figure 6.3.5 (a) Generation probability of secondary vortex at trailing edge, (b) flow visualization results at middle displacement with the maximum downward velocity at *Vr*=4.0 and (c) *V-A* diagram of TYPE-2 cross section (*L*=0.25*D*, *Sc*=4.7)

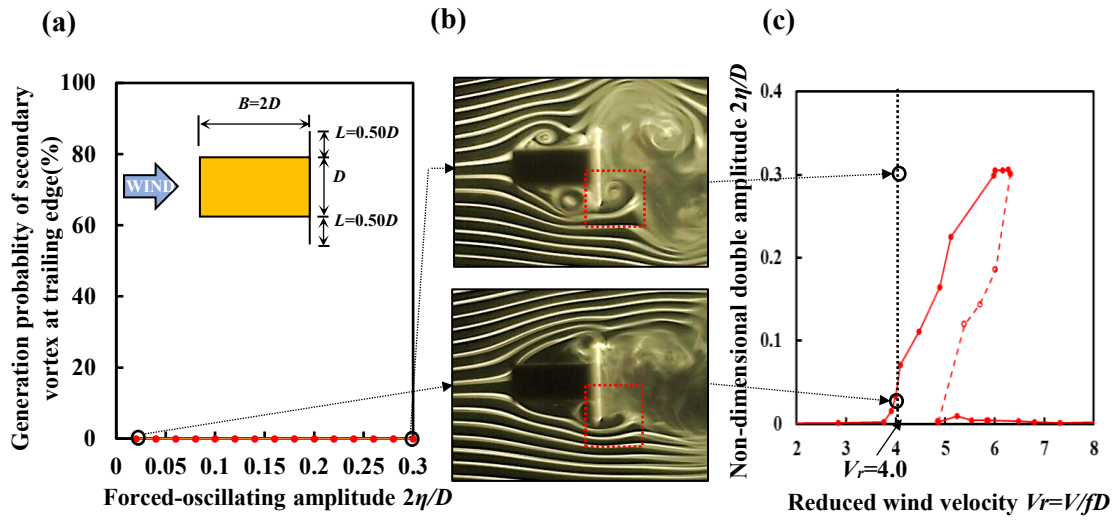

Figure 6.3.6 (a) Generation probability of secondary vortex at trailing edge, (b) flow visualization results at middle displacement with the maximum downward velocity at *Vr*=4.0 and (c) *V-A* diagram of TYPE-2 cross section (*L*=0.50*D*, *Sc*=4.7)

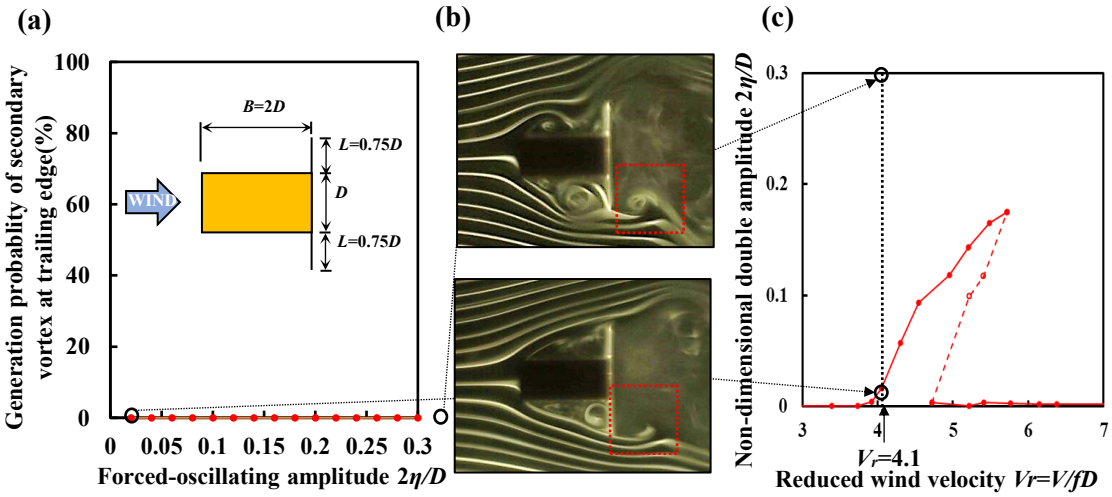

Figure 6.3.7 (a) Generation probability of secondary vortex at trailing edge, (b) flow visualization results at middle displacement with the maximum downward velocity at *Vr*=4.1 and (c) *V-A* diagram of TYPE-2 cross section (*L*=0.75*D*, *Sc*=4.7)

generated due to this collision. As shown in the bottom figures in **Figure 6.3.5 (b)-Figure 6.3.7 (b)**, a deformed vortex at the trailing edge is beginning to be generated after the separated vortex from leading edge collided with the vertical plate. Hence, the vortex generated at the trailing edge has the same shedding frequency as the separated vortex from leading edge. However, according to the conventional description of the secondary vortex at trailing edge, the generation of the secondary vortex at trailing edge is caused by the vertical motion of the model and the relative flow in the vertical direction[7]. Thus, these vortices generated at the trailing edge of TYPE-2 cross sections do not belong to the secondary vortex at trailing edge.

Therefore, there was no secondary vortex at trailing edge generated for all the TYPE-2 cross sections regardless of the forced-oscillating amplitude, as shown in **Figure 6.3.5-Figure 6.3.7**. Based on this fact, it can be considered that the secondary vortex at trailing edge is not essential for the generation of the motion-induced vortex vibration for all the TPYE-2 cross sections. Furthermore, it is also clear that the vertical plate attached at the trailing edge of a rectangular cross section has an effect which can eliminate the generation of the secondary vortex at trailing edge.

6.4 The Effect of Secondary Vortex at Trailing Edge on Motion-induced Vortex Vibration at Peak Response for Target Cross Sections in a Heaving Mode

(1) TYPE-1 cross sections

Figure 6.4.1 (a) shows the results of the measurements of the generation probability of the secondary vortex at trailing edge of the TYPE-1 and rectangular cross sections at the reduced wind velocity of V_r=5.2 which is close to the reduced wind velocity where the maximum response amplitudes occurred. **Figure 6.4.1 (b)-(d)** show the results of flow visualization tests taken at the reduced wind velocity of V_r=5.2 in the forced-oscillating amplitude of $2\eta/D$=0.26 for TYPE-1 cross sections. It was confirmed that the secondary vortex at trailing edge for TYPE-1 cross sections tends to be less likely to be generated as θ becomes larger, as shown in **Figure 6.4.1 (a)**. In the cross sections of θ=10°, 15°, the generation probabilities of the secondary vortex at trailing edge were 15% maximally within the range of the response amplitude of motion-induced vortex vibration $2\eta/D$=0-0.26. This result indicates that the secondary vortex at trailing edge was hardly generated when the non-dimensional double amplitude was smaller than $2\eta/D$=0.26. In other words, the generation of the secondary vortex at trailing edge is not essential even at the wind velocity where relatively larger response amplitude occurs for the cross sections of θ=10°, 15°.

Subsequently, the maximum response amplitudes of the cross sections of θ=5°, 10° and 15° are approximately the same, as shown in **Figure 6.2.1**. However, the generation probabilities of the secondary vortex at trailing edge for the cross sections of θ=5°, 10° and 15° at the reduced wind velocity of Vr=5.2 in the forced-oscillating amplitude of $2\eta/D$=0.26 are 60%, 15% and 0%, respectively, as shown in **Figure 6.4.1**. Based on this fact, it can be considered that the secondary vortex at trailing edge does not contribute to the exciting force of the motion-induced vortex vibration at the stage

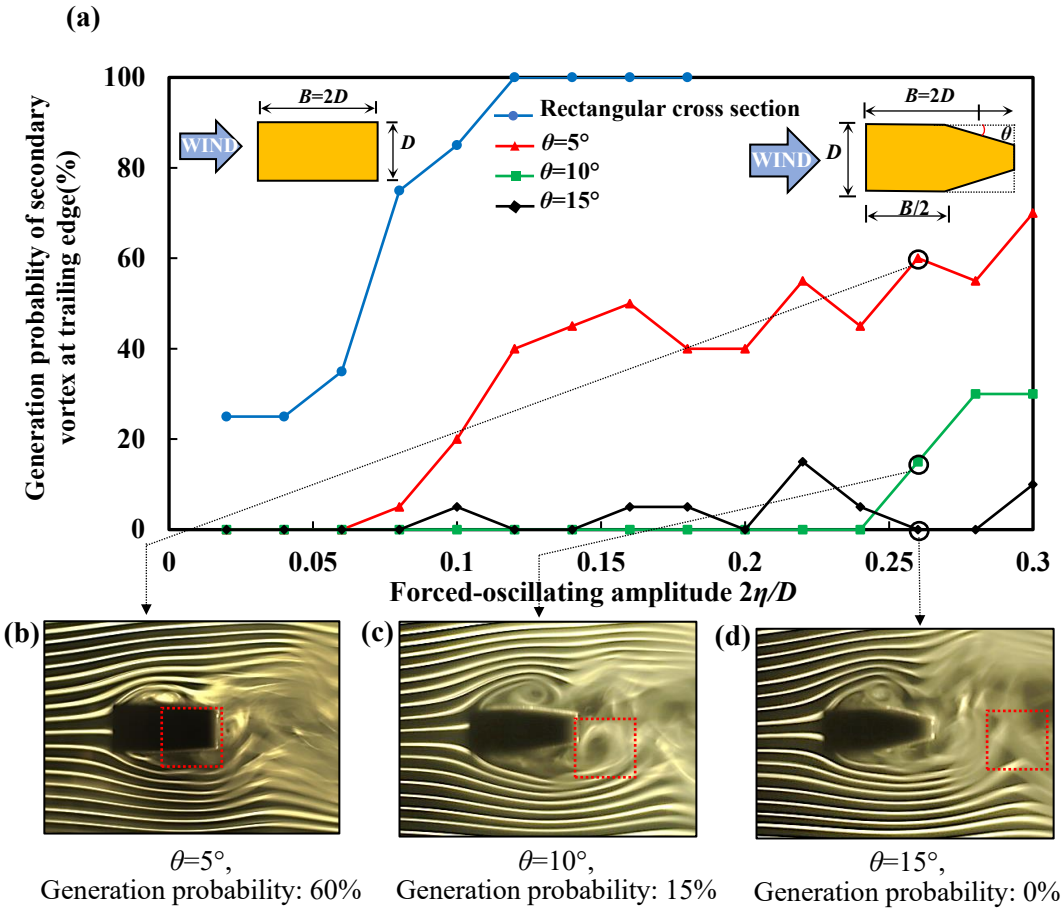

Figure 6.4.1 (a) Generation probability of secondary vortex at trailing edge for TYPE-1 and rectangular cross sections at V_r=5.2, (b) flow visualization results at V_r=5.2 in $2\eta/D$=0.26 at middle displacement with the maximum downward velocity for TYPE-1 cross section, θ=5°, (c) θ=10° and (d) θ=15°

where a larger response amplitude occurs.

(2) TYPE-2 cross sections

Figure 6.4.2 (a) shows the results of the measurements of the generation probability of the secondary vortex at trailing edge of the TYPE-2 cross sections at the reduced wind velocity of V_r=4.7 and the rectangular cross section at V_r=5.2, which are close to the reduced wind velocity where the maximum response amplitudes occurred. **Figure 6.4.2 (b)-(d)** show the photographs of flow visualization tests taken at the reduced wind velocity of V_r=4.7 in the forced-oscillating amplitude of $2\eta/D$=0.30 for TYPE-2 cross sections. At the trailing edge of each TYPE-2 cross section, it was observed that a deformed vortex was generated due to the collision of the separated vortex from leading edge and the vertical plate attached at the trailing edge. Hence, the generation probability of the secondary vortex at trailing edge was 0% for all TYPE-2 cross sections regardless of the forced-oscillating amplitude. Therefore, it is suggested

that the generation of the secondary vortex at trailing edge is not essential at the wind velocity where a relatively larger response amplitude occurs for TYPE-2 cross sections.

Furthermore, **Figure 6.2.7** has indicated that the maximum response amplitudes of the rectangular cross section and the cross sections of L=0.25D, 0.50D have nearly the same value. Nevertheless, the generation probability of the secondary vortex at trailing edge for the rectangular cross sections at the reduced wind velocity of V_r=5.2 in the forced-oscillating amplitude larger than $2\eta/D$=0.12 is 100%, whereas it is 0% for the cross sections of L=0.25D, 0.50D, as shown in **Figure 6.4.2**. From this fact, it can be concluded that the secondary vortex at trailing edge does not contribute to the exciting force of the motion-induced vortex vibration at the stage where a larger response amplitude occurs for TYPE-2 cross sections.

Based on the results obtained from TYPE-1 and TYPE-2 cross sections, it is suggested that the secondary vortex at trailing edge is not essential even at the wind

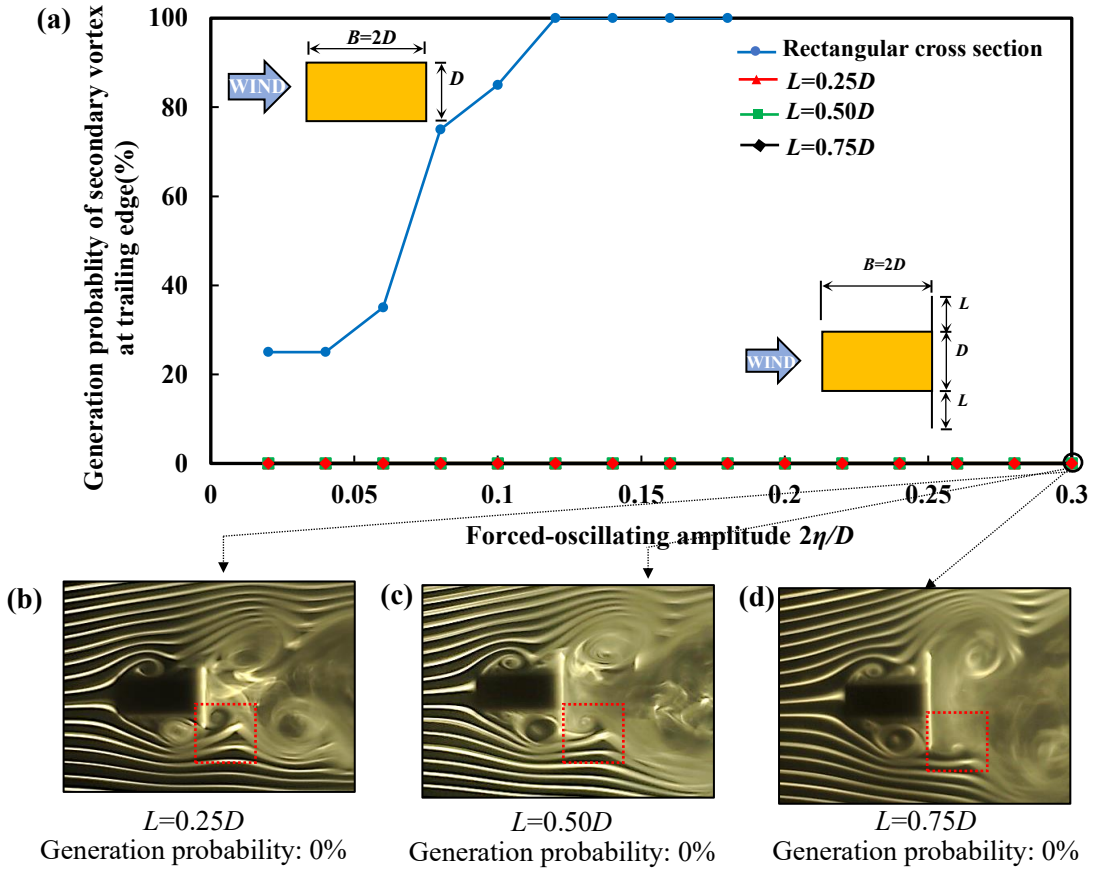

Figure 6.4.2 (a) Generation probability of secondary vortex at trailing edge for TYPE-2 sections at V_r=4.7 and for rectangular cross section at V_r=5.2, (b) flow visualization results at Vr=4.7 in $2\eta/D$=0.30 at middle displacement with the maximum downward velocity for TYPE-2 cross section, L=0.25D, (c) L=0.50D and (d) L=0.75D

velocity where a larger response amplitude of the motion-induced vortex vibration occurs. It can be considered that the secondary vortex at trailing edge does not affect the exciting force of the motion-induced vortex vibration.

6.5 Summary

In this chapter, two kinds of cross sections TYPE-1 and TYPE-2 where the secondary vortex at trailing edge is considered less likely to be generated are selected as the target cross sections. The results of the spring-supported and flow visualization tests in the heaving mode are discussed. Subsequently, the response characteristic of TYPE-1 and TYPE-2 cross sections are obtained. Moreover, the results of the flow visualization tests at the onset and the peak response of the motion-induced vortex vibration are demonstrated. Based on the results obtained from the spring-supported and flow visualization tests for the two kinds of cross sections, following conclusions have been drawn:

1. The motion-induced vortex vibration is confirmed as occurring on the TYPE-1 and TYPE-2 cross sections. The maximum response amplitudes of the motion-induced vortex vibration for TYPE-1 cross sections are smaller than for the rectangular cross section. It can be explained in a way that separated vortex from leading edge tends to become unstable while moving toward the leeward part of the model. Thus, the fluctuating wind pressure provided by separated vortex from leading edge seems to decrease in a consequence. For TYPE-2 cross sections with the vertical plates of L=0.25D, 0.50D, the maximum response amplitudes of the motion-induced vortex vibrations are approximately the same as the rectangular cross section. Whereas the maximum response amplitude of the motion-induced vortex vibration for the TYPE-2 cross sections with the vertical plate of L=0.75D is smaller than the rectangular cross section. Because the vertical plate of L=0.75D inhibits the separated vortex from leading edge from moving along the upper and lower surfaces of the model. As a result, the separated vortex from leading edge gradually separates from the upper and lower surfaces of the model. Thus, the fluctuating lift provided by the separated vortex from leading edge does not seem to fully act on the model with the vertical plate of L=0.75D.
2. With regard to the TYPE-1 cross sections, it is clear that the secondary vortex at trailing edge is less likely to be generated, compared with the rectangular cross

section. Furthermore, the larger the gradient θ is, the less likely the secondary vortex at trailing edge tends to be generated. With respect to the TYPE-2 cross sections, the secondary vortex at trailing edge is not generated regardless the forced-oscillating amplitude. Because the vertical plate attached at the trailing edge of a rectangular cross section has an effect which can eliminate the generation of the secondary vortex at trailing edge.

3. With regard to the TYPE-1 and TYPE-2 cross sections, at the onset wind velocity of the motion-induced vortex vibration, the secondary vortex at trailing edge is not essential for the generation of the motion-induced vortex vibration.

4. At the wind velocity where a larger response amplitude of the motion-induced vortex vibration occurs, the secondary vortex at trailing edge is not necessary, because it can be considered that the secondary vortex at trailing edge does not contribute to the exciting force of the motion-induced vortex vibration.

References

1) Matsuda, K., Kato, K., Cao, N., Shigetomi, K. and Ejiri, K., 2019. Motion-induced vortex vibration of a diagonal member in a steel truss bridge, 12th Pacific Structure Steel Conference (PSSC'2019), Tokyo, Japan.
2) Nagao, F., Shiraishi, N. and Matsumoto, M., 1982. Effects of a vertical edge plate on the vortex-induced oscillation of B/D=3 rectangular cross section, Proceeding of 37th Annual Conference of Japan Social Civil Engineering, I-236, 471-472. (in Japanese)
3) Matsuda, K., Kato, K., Hisatomi, K. and Suda, K., 2013. Low speed instability of two-dimensional rectangular prims, Proceeding of the ASME 2013, Pressure Vessels and Piping Conference (PVP2013), 97353, Paris, France.
4) Matsuda, K., Kato, K., Tamai, Y., and Suda, K., 2016. Experimental study on aerodynamic vibrations of rectangular cross sections having low side ratios, Proceedings of 8th International Colloquium on Bluff Body Aerodynamics and Applications, Boston, USA.
5) Okajima, A., 1990. Numerical simulation of flow around rectangular cylinders, Journal of Wind Engineering and Industrial Aerodynamics, 33, 171-180,
6) Matsumoto, M., Yagi, T., Lee, J., Hori, K., Kawashima, Y. and Hashimoto, M., 2006: The effects of the Karman vortex in aerodynamic forces around rectangular cylinders, Proceeding of 19th National symposium on Wind Engineering., 313-318. (in Japanese)
7) Shiraishi, N. and Matsumoto, M., 1983. On classification of vortex-induced oscillation and its application for bridge structures, Journal of Wind Engineering and Industrial Aerodynamics, 14 (1-3), 419-430.

Chapter 7: Conclusions and Future Issues

7.1 Conclusions

From the conventional conception on the motion-induced vortex vibration, it is deemed that the motion-induced vortex vibration is caused by the unification of the separated vortex from leading edge and the secondary vortex at trailing edge. Both the separated vortex from leading edge and the secondary vortex at trailing edge play important roles in the motion-induced vortex vibration. However, according to the aerodynamic characteristics of the rectangular cross sections with side ratio B/D=1.18, it is suggested that the motion-induced vortex vibration can occur without the formation of secondary vortex at trailing edge. This prospective indicates that the role of the secondary vortex at trailing edge in the motion-induced vortex vibration needs to be reevaluated. In this study, rectangular cross sections with side ratios of B/D=0.50-6.0 including side ratios smaller than B/D=2.0 were used as the target cross sections. In addition, specific cross sections where the secondary vortex at trailing edge is considered less likely to occur were also used in order to get a better grasp on the effect of the secondary vortex at trailing edge on the motion-induced vortex vibration. Spring-supported and flow visualization tests were conducted in order to clarify the role of the secondary vortex at trailing edge in the motion-induced vortex vibration. The main findings obtained from this study can be divided into four parts.

1. The role of the secondary vortex at trailing edge in the motion-induced vortex vibration for rectangular cross sections with small side ratios of B/D=0.62, 0.75, 1.0, 1.18 in the heaving mode:
    - It is clear that the motion-induced vortex vibration can be generated without the shedding of the secondary vortex at trailing edge. Therefore, it is suggested that the secondary vortex at trailing edge is not a necessary condition for the generation of the motion-induced vortex vibration regarding the rectangular cross sections with side ratios side ratios of B/D=0.62, 0.75, 1.0, 1.18.
2. The role of the secondary vortex at trailing edge in the motion-induced vortex vibration for rectangular cross sections with side ratios of B/D=2.0, 4.0, 6.0 in the

heaving mode:

- At the onset wind velocity of the motion-induced vortex vibration, the stable shedding of the secondary vortex at trailing edge is not a necessary condition for the generation of the motion-induced vortex vibration.
- At the peak response amplitude of the motion-induced vortex vibration, it is figured out that the secondary vortex at trailing edge can be relevant to the magnitude of the exciting force acting on the model in terms of affecting the intensity of the integrated vortex consisting of the separated vortex from leading edge and the secondary vortex at trailing edge for rectangular cross sections with side ratios of B/D=2.0, 4.0, 6.0 in the heaving mode.

3. The role of the secondary vortex at trailing edge in the motion-induced vortex vibration for rectangular cross sections with side ratios of B/D=2.0, 4.0, 6.0 in the torsional mode:
   - In the torsional mode, at the onset wind velocity of the motion-induced vortex vibration, the stable shedding of the secondary vortex at trailing edge is not a necessary condition for the generation of motion-induced vortex vibration.
   - On the other hand, at the peak response amplitude of the motion-induced vortex vibration, the secondary vortex at trailing edge can be relevant to the magnitude of the exciting moment acting on the model in terms of affecting the intensity of the integrated vortex consisting of the separated vortex from leading edge and the secondary vortex at trailing edge for rectangular cross sections with side ratios of B/D=2.0, 4.0, 6.0 in the torsional mode, just the same as the results obtained from the heaving mode.
4. The role of the secondary vortex at trailing edge in the motion-induced vortex vibration for specific cross sections:
   - With regard to the selected TYPE-1 and TYPE-2 cross sections, at the onset wind velocity of the motion-induced vortex vibration, the secondary vortex at trailing edge is not essential for the generation of the motion-induced vortex vibration.
   - At the wind velocity where a larger response amplitude of the motion-induced vortex vibration occurs, the secondary vortex at trailing edge is not

necessary, because it can be considered that the secondary vortex at trailing edge does not contribute to the exciting force of the motion-induced vortex vibration.

It is well known that the motion-induced vortex vibration is one of the most important design issues in the wind engineering, especially for bridge structures, since the service lives of bridge decks are prone to be influenced by the motion-induced vortex vibration. However, the conventional conception on the secondary vortex at trailing edge is not explicit. Hence, it can be difficult to improve the wind-resistant performance of bridge decks and additional members efficiently for wind-resistant designers with respect to the aerodynamic vibration control countermeasure against the motion-induced vortex vibration. Based on the results obtained from this study, it has been clear that at the onset wind velocity of the motion-induced vortex vibration, the secondary vortex at trailing edge is not a necessary condition for the generation of the motion-induced vortex vibration. On the other hand, at the peak response amplitude of the motion-induced vortex vibration, the secondary vortex at trailing edge can be relevant to the magnitude of the exciting force of the motion-induced vortex vibration for the rectangular cross sections with side ratios of B/D=2.0, 4.0, 6.0. In addition, regarding the specific cross sections mentioned in this study, the secondary vortex at trailing edge does not affect the onset and the exciting force of the motion-induced vortex vibration. In the bridge engineering area, these findings can be helpful to wind-resistant designers in terms of optimizing cross sections of bridge decks and maximizing the improvement of the additional members on the wind-resistant performance against the motion-induced vortex vibration.

7.2 Future Issues

In this study, the flow patterns of the secondary vortex at trailing edge and the separated vortex from leading edge were confirmed by flow visualization tests. The response characteristics of the target cross sections were obtained by spring-supported tests. By comparing the flow patterns of the secondary vortex at trailing edge and the separated vortex from leading edge with the response characteristics of the target cross sections, the effects of the flow patterns of the secondary vortex at trailing edge and the separated vortex from leading edge on the aerodynamic characteristics of the motion-induced vortex vibration are discussed qualitatively. However, regarding the

effect of the flow pattern of the separated vortex from leading edge on the aerodynamic characteristics of the motion-induced vortex vibration, a quantificational experiment still needs to be conducted in order to obtain a more accurate evaluation, such as the measurement of the unsteady pressure distribution on the model.

On the other hand, all the experiments in this study were carried out in a smooth flow. Nevertheless, in reality, the flow acting on structures usually is not a smooth flow, instead of a flow with a turbulence intensity to some extent. Thus, in order to evaluate the role of the secondary vortex at trailing edge in the motion-induced vortex vibration for actual structures, the experiments in a turbulence flow may need to be conducted to enhance the understanding.

Acknowledgements

First and foremost, I would like to avail myself of the opportunity to express my sincere appreciation and great gratitude for kind supervision and invaluable support from Prof. Kazutoshi Matsuda. His generous attention and patience support me throughout all my six years of study in Kyushu Institute of Technology. From Prof. Kazutoshi Matsuda, I not only learned about the permanently positive researching attitude, but also the active stance towards the future work and life.

My appreciation is also due to the committee members for their inputs on the research, Prof. Koju Hiraki, Prof. Eiki Yamaguchi and Prof. Chen Peishan. I would also like to acknowledge my indebtedness to Dr. Toshikazu Takai and Mr. Kusuo Kato for their kind supports, encouragement and useful suggestions on the research.

Besides, I would like to give my thanks to Mr. Yusuke Tamai, Mr. Kentaro Suda, Mr. Hajime Ishii, Mr. Roya Higashimura, Mr. Kazufumi Ejiri, Mr. Kenta Shigetomi, Mr. Mitsushi Imamura and Mr. Tomoya Yanase for their contribution in the experiment work. I am especially indebted to Mr. Koki Arise for all his generous help in getting me settled down in Japan. My deep appreciation also goes to all the members of Structural Lab of year 2015-2021 for their assistance in my study, support, and friendship throughout my stay in Japan.

Lastly, my thanks and appreciation to my beloved parents, Xiangxu Cao and Hui Sun for their whole support, constant patience, understanding and love. I never have made it here without both of them.